Microphysical Retrievals in Mixed-Phase Clouds with low LWP using Cloud Radar

MSc thesis in Geoscience & Remote Sensing

Peiyuan Wang

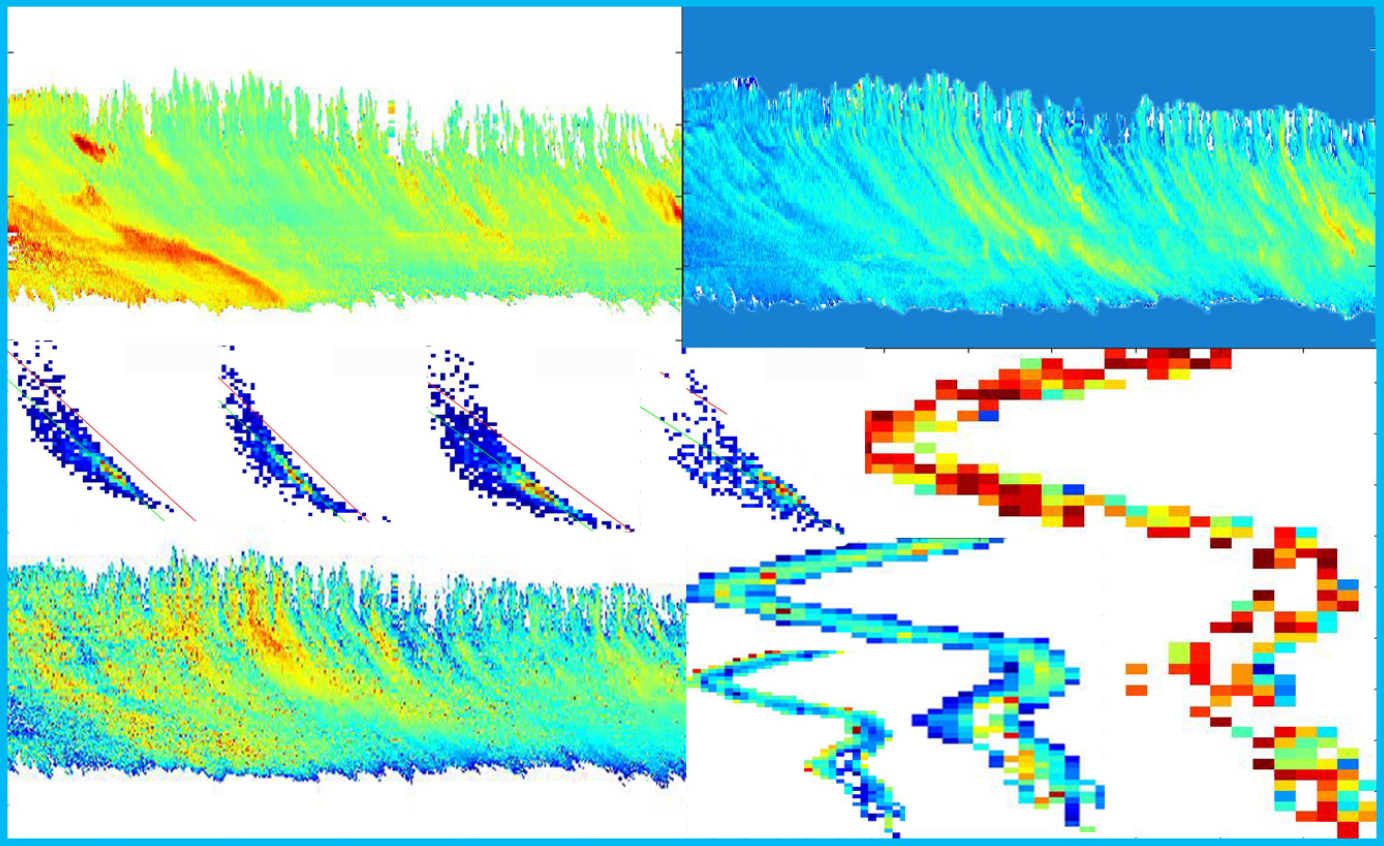

Delft University of Technology

TU Delft

Microphysical Retrievals in Mixed-Phase Clouds with low LWP using Cloud Radar

by

Peiyuan Wang

Student number:	5457653	
Project duration:	March, 2023 - January, 2024	
Thesis committee:	Ir. Christine Unal	TU Delft, Supervisor
	Dr. Marc Schleiss	TU Delft
	Dr. Franziska Glassmeier	TU Delft
	Dr. José Dias Neto	TU Delft

TU Delft

Abstract

Mixed-phase clouds, which have a significant impact on the global climate, are complex systems where liquid water and various types of ice particles coexist at temperatures below the freezing point. A key process in mixed-phase clouds is riming which alters microphysical and scattering properties of ice particles. Cloud radar is a powerful instrument for observing and understanding the processes that occur within mixed-phase clouds. Observations from multi-frequency radars and simulation results were combined in recent research to retrieve microphysical properties of ice particles in snowfall and ice clouds. This report presents an ambitious attempt to retrieve all common microphysical properties of ice particles, such as maximum dimension, density, aspect ratio and number concentration in slight-rime condition using Doppler spectra. Two mixed-phase cloud events with low liquid water path are studied for such purpose. Spectral dual-wavelength ratio is introduced to retrieve maximum dimension of particles. An iteration process is developed in order to retrieve aspect ratio and density of ice particles from observation of spectral differential reflectivity. The number concentration of particles is retrieved with additional spectral reflectivity. With all the retrieved microphysical properties, ice water content and particle size distribution can be further derived. Ice water content is compared with results from an empirical model. The retrieved properties obtained from using three distinct mass-size relations are compared. Also the bulk and spectral retrieved profiles are compared. The retrieval process can provide consistent microphysical properties of ice particles. It is found that the retrieved ice water content is generally smaller than that from empirical model. Besides, the mass-size relation has significant impact on all retrieved microphysical properties except maximum dimension. The resulting profiles from bulk retrieval are smoother, while spectral retrieval can provide values in regions where the former cannot. The possible error from different sources are discussed or estimated, including the effect on dual-wavelength ratio from the elevation angle of radar, the neglect of differential attenuation caused by liquid and the usage of soft spheroid model. Recommendations are discussed, which include the usage of the latest microphysical models for ice aggregates and Discrete Dipole Approximation for electromagnetic wave scattering simulation.

Nomenclature

List of Symbols

α	Euler angle ($^\circ$)
α_{att}	Specific attenuation (dB/km)
β	Euler angle ($^\circ$)
$\boldsymbol{r}$	The position of a volume element relative to the centre of mass, Equation 2.10
ϵ	Dielectric constant (-)
ϵ_{eff}	Effective dielectric constant of the medium (-)
ϵ_i	Dielectric constant of the inclusion (-)
ϵ_m	Dielectric constant of the matrix (-)
η	Radar reflectivity (m^{-1})
λ	Wavelength (m)
μ	Shape parameter of gamma distribution PSD (-)
ρ	Density (g/cm^3)
ρ_w	Density of water (g/cm^3)
ρ_{ice}	Density of ice (g/cm^3)
σ_b	Backscattering cross section (mm^2)
σ_r	Radar cross section (m^2)
a	Prefactor of the power-law mass-size relation (-)
b	Exponent of the power-law mass-size relation (-)
B / DWR	Dual-wavelength ratio (-/dB)
D	Melted-equivalent diameter (mm)
D_0	Median volume diameter (mm)
D_v	Melted-equivalent diameter (cm)
D_{max}	Maximum dimension (cm/mm)
D_{mean}	Mean of maximum chord lengths (Equation 2.13) (m)
Elv	Elevation angle of radar ($^\circ$)
f	The form factor (-)
f_{ice}	Volume fraction of ice (-)
h	Height (m)

IWC_{em}	Empirical ice water content (g/m^3)
K	Clausius-Mossotti factor (-)
k	Wave number (m^{-1})
k_a	Attenuation coefficient per unit mass (dBm^{2}kg^{-1})
m	Mass (g)
N	Particle size distribution (m^{-3})
N_w	The intercept parameter of gamma distribution PSD (mm^{-1}m^{-3})
P_s	Saturation vapor pressure (Pa)
r	Radar range (m)
r_d	Density factor (-)
R_w	Specific gas constant for water vapor (J/kg/K)
r_{av}	Average radius of gyration (mm)
r_g	Radius of gyration (mm)
RH	Relative Humidity (-)
sZ_{dr} / sZDR	Dual-wavelength ratio (dB)
sZ_{hh35}	Spectral reflectivity at 35GHz (dB)
sZ_{hh94}	Spectral reflectivity at 94GHz (dB)
sZ_{hh} / sZ_{vv}	Spectral reflectivity at horizontal / vertical polarization (dBZ)
sZ_m	Measured spectral reflectivity factor (dBZ)
T	Temperature ($^\circ$C)
V	The volume of spheroid (cm^3)
v	Doppler velocity (m/s)
Z_e / ZE	Equivalent reflectivity factor (mm^6 m^{-3} / dBZ)
Z_{dr} / ZDR	Differential reflectivity (dB)
Z_m	Measured reflectivity factor (dBZ)
AH	Absolute humidity (kg/m^3)
AR	Aspect ratio (-)
DPIA	Two-way path-integrated differential attenuation (dB)
ELWP	Effective liquid water path (kg/m^2)
IWC	Ice water content (g/m^3)
IWP	Ice water path (g/m^2)
LWP	Liquid water path (g/m^2)
NOP	Number concentration of particles (m^{-1})
sDWR	Spectral dual-wavelength ratio (dB)

Abbreviation

BR / SR	Bulk / Spectrally retrieved
DDA	Discrete Dipole Approximation
LUT	Look-up table
MPC	Mixed-phase cloud
NWP	Numerical weather prediction
PSD	Particle size distribution
RG	Rayleigh-Gans
SIP	Secondary ice production
SSTM	Soft spheroid and T-matrix
TM	T-matrix
WOS	The width of spectrum

Contents

1 Introduction

Cold clouds, including ice clouds and mixed-phase clouds, are clouds above the freezing level. They play a key role in global precipitation and climate. Most of Earth's precipitation is originated from precipitating ice [1]. According to a study of satellite observation, a large fraction of continental rain (except the Antarctica) is from ice clouds (≈60%) and mixed-phase cloud (≈10%) [2]. A mixed-phase cloud (MPC) is a kind of cloud where ice particles, supercooled liquid droplets and water vapor coexist below zero degree Celcius [3]. They're ubiquitous in the troposphere and exist from polar to tropical regions, though they tend to be more frequent at mid- and high-latitudes [4]. The mixed-phase condition can occur down to $-40°C$ and up to $0°C$. One or multiple supercooled liquid layers can exist in a cloud [5], where one of the four processes in Secondary Ice Production (SIP), the Hallett-Mossop mechanism [6], is believed to happen. Mixed-phase clouds are famously difficult to characterize in numerical weather prediction and climate models [3]. Since atmospheric ice formation and growth processes have a major impact on the Earth's radiative balance and on the hydrological cycle [7], the microphysical processes and quantities within cold clouds attract widespread interests. Previous research about MPC involving cloud radars was mostly focused on revealing complex phenomena [8, 9, 10] as well as distinguishing and quantifying liquid and ice [11, 12, 13]. The microphysical quantities of ice particles include particle size, density, shape, number concentration, etc.

Multiple in-situ measurements and remote sensing approaches for retrieving quantities of atmospheric ice were developed. Cloud radars have been widely used for their capability to detect tiny hydrometeors in clouds. In all the retrieval process, some are more empirical while others are more physical, but the MPCs are always more challenging to deal with. Hogan et. al. [14] found that the radar reflectivity at 35 GHz can be used to retrieved ice water content (IWC) within stratiform midlatitude ice clouds with empirical relation and assumed mass-size relation, but the accuracy is poorer in MPCs. Temperature profiles were later introduced to constrain number concentration when IWC was retrieved. In order to retrieve number concentration of ice particles in stratiform MPCs, Zhang et. al. [15] combined cloud-top temperature, liquid water path (LWP) and radar reflectivity in an ice growth model. Matrosov et. al. [16] effectively retrieved aspect ratio using differential reflectivity and copolar correlation coefficient of ice particles. These research typically focused on retrieving a certain property of ice particles with single-frequency radars.

More recently, multi-frequency Doppler cloud radars became popular because they are able to reveal more information about ice particles. Leinonen et. al. [7] developed an algorithm that retrieves size, density and number concentration of snow from radar reflectivity of three frequencies, based on databases of snow scattering properties. The attenuation caused by supercooled liquid was ignored, but snow and gas attenuation were corrected. To retrieve particle size distribution in ice clouds, Barrett et. al. [17] exploited spectral reflectivity of three frequencies from vertically-pointing radars with overall correction for attenuation. Median mass diameter, bulk aspect ratio (overall shape) and IWC were also retrieved from bulk radar measurements for snow [18], with the correction of snow and gas attenuation. However, there's still no attempts to make retrieval for all these quantities of ice particles using Doppler spectra in cold clouds, especially in mixed-phase clouds. The presence of an ample amount

of supercooled liquid in MPC can make the retrieval more challenging.

Hence, my research attempts to retrieve the aspect ratio and density of ice particles using Doppler spectra while also providing retrieval of other quantities (size, number concentration and ice water content), which can be applied to MPCs with low LWP and ice clouds. For this purpose, a semi-physical retrieval process is proposed in this report. With the knowledge on aggregation process and scattering properties, the retrieval process will no longer be purely empirical. Low-LWP condition allows the usage of some conclusions for ice clouds with limited bias introduced. Besides, the impact of different mass-size relations, a key assumption in the retrieval needs to be evaluated, because there's no conclusion about which one is most appropriate in low-LWP MPC. Moreover, the assumption in the retrieval is that all particles in a velocity bin are identical. It would be interesting to find out the impact of extending this assumption to the entire radar volumes. A comparison of the results from retrieval based on bulk variables and spectral data is useful for determine their consistency, which was not done before. Since the supercooled liquid is ignored, a simulation study is conducted to assess its impact from the perspective of differential attenuation. All of these are made possible by a cloud radar that can provide measurements of dual-wavelength ratio and differential reflectivity simultaneously, which was not available before.

1.1. Research Questions

This research focuses on retrieving microphysical properties of ice particles within mixed-phase clouds. Specifically, I focus on MPCs which contain little supercooled liquid water (i.e., low liquid water path) and mostly ice particles. This research will try to answer the following questions:

1. How can we design a semi-physical process to retrieve spectra of aggregate size, density, aspect ratio and number concentration in mixed-phase clouds using cloud radar measurements?
2. Are there cases for which we can retrieve the aggregate size distribution?
3. What's the difference between ice water content retrieved based on a purely empirical relation and the proposed semi-physical process?
4. How does the usage of different mass-size relations affect retrieval results?
5. What are the differences between retrievals based on bulk variables compared to spectral data?
6. How does the neglect of the differential attenuation caused by supercooled liquid affect the retrieved size and mass?

To answer these questions, methodology of retrieval and the physics behind are studied.

In Chapter 2, radar measurements involved in this research are firstly introduced. Methods and conclusions from previous studies about ice particles in the atmosphere using radar are reviewed along with some comments. In Chapter 3, the data used in this study is introduced. Chapter 4 presents the results of scattering simulation using T-matrix, which provides references to the development of methodology. Chapter 5 describes the details of retrieval process step by step. Chapter 6 presents the retrieval results from two typical events and provides insights to the results. In Chapter 7, the conclusions along with the recommendations are given for this study. In Appendix Section A, LV0 DWR and LV1 DWR are compared. Also, a direction of this study that has been discontinued is presented (Section B). The reason behind the failure is discussed and presented with some suggestions. Some retrieval results of a third MPC event are also presented (Section C).

2

Background

In this Chapter, the radar observables related to this research are firstly introduced. Then the manners to deal with differential scattering and attenuation contribution in DWR in ealier studies of clouds are illustrated. The radar observation of different phenomena in MPC is reviewed, which includes riming of aggregates and the existence of supercooled liquid droplets. Forward modelling including microphysical models of aggregates and scattering calculation methods are then reviewed, with an emphasis on Rayleigh-Gans theory and the DWR-size relation derived based on it. The current mass-size relations of unrimed and slightly-rimed aggregates are then introduced. Finally, the concepts of bulk and spectral retrieval are introduced.

2.1. Radar Observables

Active radars typically detect targets by emitting electromagnetic waves towards them and measuring the reflected signals.

2.1.1. Radar Reflectivity

The equivalent reflectivity factor $Z_{e,\lambda}$ at wavelength λ is defined by [19]:

$$Z_{e,\lambda} = \frac{\lambda^4}{\pi^5 |K_W|^2} \eta \tag{2.1}$$

where η (m^2m^{-3}) is the radar reflectivity and $|K_W|^2$ the refractive index of water. When particles are within Rayleigh regime, $Z_{e,\lambda}$ can also be calculated as below [20]:

$$Z_{e,\lambda} = \int_D D^6 N(D) dD \tag{2.2}$$

where D (mm) is the equi-volume diameter of particle and $N(D)$ ($mm^{-1}m^{-3}$) the particle size distribution (PSD). The radar reflectivity η is calculated as [20]:

$$\eta = \int_D \sigma_b(D) N(D) dD \tag{2.3}$$

where σ_b is the backscattering cross section of a particle. The reflectivity factor of radar is expressed in units of mm^6/m^3. Since the particle size can vary over many orders of magnitude, the logarithm $10log_{10}(Z_e)$ is commonly used and its unit is dBZ [20]. η is proportional to λ^{-4} when particles are significantly smaller than the wavelength (Rayleigh regime). Thus $Z_{e,\lambda}$ in Rayleigh regime doesn't depend on wavelength (Equation 2.1). When particles are larger, Mie scattering happens and η is no longer proportional to λ^{-4}, neither is $Z_{e,\lambda}$ independent of wavelength [19].

The reflectivity factor measured by radar in logarithm at range r is [19]:

$$Z_{m,\lambda}(r) = Z_{e,\lambda}(r) - 2 \int_0^r (\alpha_{att,\lambda}(s)) ds \tag{2.4}$$

where $\alpha_{att,\lambda}$ is the specific attenuation (dB/km) for wavelength λ, s the differential element of range r. Gases and hydrometeors are the main sources of attenuation for cloud radar.

2.1.2. Dual-Wavelength Ratio (DWR)

Dual-wavelength ratio (DWR) is defined as the difference of reflectivity factor measurements in logarithm at two frequency ($\lambda_1 > \lambda_2$) at the same location [19]:

$$\begin{aligned} DWR(r) &= Z_{m,\lambda_1}(r) - Z_{m,\lambda_2}(r) \\ &= Z_{e,\lambda_1}(r) - Z_{e,\lambda_2}(r) + 2\int_0^r (\alpha_{att,\lambda_2}(s) - \alpha_{att,\lambda_1}(s))ds \end{aligned} \tag{2.5}$$

The first two terms in the second row of Equation 2.5 represent the contribution from Mie effect and the final term is the two-way path-integrated differential attenuation (DPIA). The DPIA is positive because attenuation is stronger for shorter wavelength. DPIA grows as r increases. The DPIA caused by gases is always acquirable with temperature, air pressure and humdity profiles. The DPIA of liquid is challenging to obtain without the liquid water content profiles, especially in complex cases such as MPC. The DPIA caused by cloud ice particles can be ignored in most cases.

Without considering attenuation, the growth of DWR from zero starts when the scattering particle size starts to enter Mie regime for λ_2. At this moment the Z_{e,λ_2} (Z94, orange curve in Figure 2.1) becomes smaller than Z_{e,λ_1} (Z35, green curve in Figure 2.1), making a positive contribution to DWR (blue curve in Figure 2.1). As the particle becomes larger, the oscillation in Mie regime at shorter wavelength occurs and DWR also oscillates.

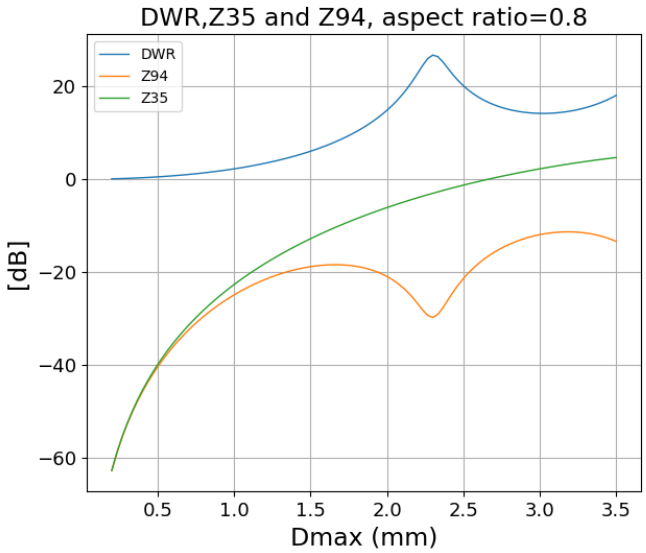

Figure 2.1: Simulation of reflectivity of a single soft spheroid particle at 94GHz and 35GHz and DWR$_{KaW}$

The particle in the simulation creating Figure 2.1 has a mass-size relation derived from [21] which is described in Equation 2.16. Note that the value of the curves in Figure 2.1, calculated using T-matrix, can have significant difference with reality, since many factors contributes to the value of reflectivity and DWR. They're going to be discussed in Section 2.5.1.

The Mie effect of ice particles in DWR was studied in earlier research. When there's Mie effect, the elevation angle of the radar can affect the sensitivity of DWR to the sphericity of ice particles [22]. When the radar is pointing closer to the zenith, the enhancement of DWR (compared to non-spherical particles) brought by particles that are more spherical is larger when other conditions remain the same.

Particles that are more spherical tend to have a more stable DWR when the elevation angle of radar is changing. On the other hand, a non-spherical particle exhibit lowest DWR when the radar is vertically-pointing. The DWR of non-spherical particles become larger when the elevation angle of radar is smaller. The more non-spherical the particle, the stronger is such variation of DWR. It's noteworthy that it's possible to measure negative DWR when a small positive DWR of tiny particles is contaminated by noise, but theoretically DWR of ice particles is only positive [22].

In conclusion, the DWR of aggregates in clouds is contributed by differential attenuation and Mie effect. The former includes contribution from gas, liquid water and ice, while the later includes size, density, aspect ratio of particles and the elevation angle of radar.

Similar to DWR, the spectral dual-wavelength ratio (sDWR) can be calculated using spectral reflectivity of two frequencies ($\lambda_1 > \lambda_2$) [17].

$$sDWR = sZ_{m,\lambda_1} - sZ_{m,\lambda_2} \tag{2.6}$$

which also has unit in dB. sDWR also includes the contribution from differential attenuation caused by hydrometeors and gases except the differential scattering.

Ideally, DWR should be calculated using the reflectivity of two frequencies for the same radar volume. Previously dual-frequency radars with well-matched radar volumes hadn't been available and studies always needed to carefully match different radar beams and assess the error brought by mismatching [23, 18, 17]. Fortunately, the radar used in this study allows calculating DWR with well-match radar volumes and reducing the error of DWR from mismatched beams as much as possible. On the other hand, the relative calibration between radar at two frequencies are essential to obtaining unbiased DWR. In this research the radar has been already carefully calibrated. A method of the relative calibration is described in [23], which utilizes the tiny ice particles at cloud top.

2.1.3. Differential Reflectivity (ZDR)

Radar observed differential reflectivity (dB) is defined as [20]:

$$Z_{dr} = 10log_{10}\left(\frac{\eta_{hh}}{\eta_{vv}}\right) \tag{2.7}$$

where η_{hh} and η_{vv} are copolar back scattering cross sections per unit volume (m^2m^{-3}) at horizontal and vertical polarizations. ZDR is widely used to characterize the shape of particles, but the radar cannot be vertically-pointing when ZDR is used for such purpose. The reason is that all particles tend to have their maximum dimension in horizontal plane and minimum dimension vertical, but the azimuth of their maximum dimension is random. ZDR will be zero in this case as long as the radar is well calibrated. For the same population of particles, ZDR is affected by the elevation angle of radar. The more horizontal the incident beam, the more sensitive ZDR is to the aspect ratio of particles. In a radar volume, ZDR is affected more by the aspect ratio of large particles because the radar reflectivity depends heavily on the reflectivity of large particles. The spectral differential reflectivity (dB) is calculated using spectral reflectivity factor:

$$sZ_{dr} = sZ_{hh} - sZ_{vv} \tag{2.8}$$

where sZ_{hh} and sZ_{vv} are spectral reflectivity factor of horizontal and vertical polarization.

2.1.4. Conclusion

In summary, the radar reflectivity is affected by PSD. In other words, it is controlled by both backscattering cross-section and number concentration of particles (Equation 2.3). Therefore, number concentration of particles is possible to be retrieved from radar reflectivity. Moreover, if the ice particles are in low-LWP condition and gas attenuation can be calculated, DWR contains mainly information about particle size (differential scattering) when the particle size is not too large. ZDR on the other hand usually can be used to retrieve the overall shape and density of ice particles. Thus, these radar measurements contain information about microphysical properties in the right condition.

2.2. Differential scattering and attenuation in DWR

As mentioned previously, DWR includes contribution from differential scattering and attenuation. Under certain conditions, the dual-wavelength ratio can be attributed completely to either differential scattering or attenuation [24]. For example, a method to retrieve liquid water content (LWC) for stratocumulus using DWR was developed without the need to consider Mie effect, because the droplets are tiny and within Rayleigh regime of the shorter wavelength in DWR [25]. In the reverse situation, where liquid water is absent and ice particles are small in ice clouds, it is typically permissible to neglect the differential attenuation from liquid and ice in DWR [24]. Since the DPIA caused by gases in atmosphere is always acquirable with temperature, air pressure and humdity profiles, it is convenient to study particle size with DWR in this case.

However, the separation of Mie and differential attenuation effects for DWR is needed in the cases that both effects are non-negligible, in order to study the size of particles or liquid water content accurately [19, 24]. A common method in previous studies to obtain differential attenuation for the whole cloud is utilizing the region near cloud top where only tiny pristine ice particles are considered present and DWR remains constant [24, 23]. This type of methods can provide information of liquid water path (LWP) [26], but the distribution of liquid content along the radar beam is still unsolvable. A more attractive way is separating Mie and differential attenuation in sDWR, which has been successfully applied in rain [19]. Despite the existence of noise, it allows the retrieval of liquid water content (LWC) in rain. Such practice might face great difficulty in the cases of MPC, which will be discussed in detail in Section B . The DPIA caused by ice crystals can be ignored at all frequencies below 200 GHz, while snowflakes can produce non-negligible attenuation at and above W band [24]. In MPC cases, it is reasonable to ignore DPIA caused by cloud ice particles, though an estimation of such quantity under certain circumstances is feasible.

2.3. Radar observations of Mixed-phase cloud

2.3.1. Supercooled liquid in MPC

Supercooled liquid droplets are possible to be observed in spectral reflectivity. Using vertically-pointing radar at 35GHz and 94GHz, the author of [11] observed liquid peaks in Doppler spectra with the confirmation from LiDAR measurement. More recently, in [27] the authors also observed liquid peaks with a W-band Doppler radar (Doppler velocity resolution $0.01m/s$). The liquid peak usually has a mean Doppler velocity close to $0m/s$ in Doppler spectra from a vertically-pointing radar, because liquid droplets are tiny and the terminal velocity can be considered as zero. However, the updraft and downdraft in a convective system can shift the mean Doppler velocity of liquid peak and therefore other information is needed to confirm that the peak is due to liquid droplets. The peak with sZDR value close to zero can be an evidence, since supercooled liquid droplets are tiny (typically $5\mu m$ to $20\mu m$, [27]) and therefore nearly spherical. Observing and analyzing liquid peaks are beyond the scope of this research due to the difficulty of detecting them in Doppler spectra under low LWP conditions.

2.3.2. Riming of aggregates in MPC

One of the most characterizing processes involving ice and liquid in MPC is riming. As one of the main ice growth mechanisms, it happens when ice particles collect supercooled liquid droplets and become complex-shapes heavy particles [4]. Most studies are primarily interested in examining the effects of riming on ice particles using vertically-pointing cloud radar that can readily detect changes in the properties of these ice particles.

In initial stage of riming, the density of particles increases but the shape usually remains unchanged [28]. Therefore, an important feature of riming in radar observation is the significantly increased terminal fall velocity of rimed particles. Vertically-pointing Doppler radars are used in many studies to measure Doppler velocity as terminal velocity. The mean Doppler velocity was used to determine the degree of riming in an earlier study [29]. It shows that heavy rimed particles have a fall velocity larger than $1.5m/s$, while for aggregates the terminal velocity rarely exceed $1.3m/s$ [30]. However, within convective systems, the presence of strong updrafts and downdrafts can render this approach too challenging. In recent studies, velocities measurements are combined with other radar observables (such as DWR [31]) to reveal more convincing information. For this research, terminal velocity is not available because

no reliable horizontal wind profiles can be used to extract terminal velocity from Doppler velocity, as a slant-viewing radar is used.

Another distinguishing feature of riming in radar observation is the triple frequency signature of rimed aggregates. It was observed in radar measurements for the first time that rimed particles gather along a near-horizontal line in triple frequency space, while the pattern of unrimed aggregates bend away from it significantly in [32]. In recent studies, it was discovered in both simulations and observations that density and internal structure of ice particles affect the shape of triple frequency curve [31, 33]. The increase of density and change of internal structure from heterogeneous to homogeneous are typical phenomena in riming process. However, since there is significant ambiguity between the radar signatures of small particles of all types, triple frequency signature are mainly studies for larger particles in snow [33]. Although the radar used in this research only has dual frequencies, the knowledge about triple frequency signatures can be helpful.

2.4. Forward Modelling

In order to retrieve information for ice particles from radar measurements, forward modelling is essential to provide a reference. Two kinds of essential models in forward modelling are microphysical models which decide the structure of ice particle and scattering models which describe how electromagnetic wave interacts with ice particles.

In the case of retrieval of particle size from DWR, the knowledge of the type of particles are needed, as many studies show that particle shape and density can affect the value of DWR [22, 34]. Size retrieval for aggregates was mainly studied because of their prevalence in ice cloud and snow precipitation. Based on different microphysical models of aggregation and different scattering model, one can have different relation connecting DWR and the size of aggregation.

2.4.1. Microphysical Models

The microphysical models for ice particles have been widely studied. They can generally be divided into two categories: Physical models and empirical models [35]. The physical models create aggregates by simulating the physical process of the growth of aggregates such as diffusional growth, aggregation and riming, while the empirical models build aggregates using knowledge from measurements of real particles and exclude unnecessary details [35]. The results from the former models are applicable to various condition though they're time-consuming to obtain, while the later usually save time but lack versatility.

A worth-mentioning model is soft spheroid. It is usually used to characterize the shape of particles when the scattering model T-matrix is used. The spheroid can be oblate or prolate. It is assumed that the spheroid is filled with a kind of medium, which means that the particles is perfectly homogeneous. The complex refractive index of the spheroid can be computed using Maxwell-Garnett effective medium approximation when there are actually different kinds of medium contained [36]:

$$\left(\frac{\epsilon_{eff}-\epsilon_m}{\epsilon_{eff}+2\epsilon_m}\right)=\delta_i\left(\frac{\epsilon_i-\epsilon_m}{\epsilon_i+2\epsilon_m}\right) \tag{2.9}$$

where ϵ_{eff} is the effective dielectric constant of the medium, ϵ_i of the inclusions, and ϵ_m of the matrix. δ_i is the volume fraction of the inclusions.

2.4.2. Scattering models

There are mainly three types of scattering models that involve in the study of ice particles, including T-matrix, Discrete Dipole Approximation and models based on Rayleigh-Gans theory.

T-matrix

T-matrix (TM) approach is one of the most widely used tools for calculating electromagnetic wave scattering by non-spherical particles based on directly solving Maxwell's equation [37]. It's often used with spheroid model because the rotational symmetry allows substantial simplification of the equations,

though in fact it can compute electromagnetic wave scattering for particles with arbitrary shape [37]. Although it is a good scattering model for raindrops and some types of ice particles like columns and plates, recently it is not considered sufficient for complex ice particles such as aggregates measured at high frequencies for the soft spheroid model it employs. This will be further elaborated in Section 2.5.1. However, T-matrix provides great convenience in setting the properties of simulated particles. Users only need to provide simple quantities such as the diameter and aspect ratio in order to make a simulation. Nevertheless, the DDA is the most popular method in recent studies and has a promising future as the study continues in ice particles with complex shape.

Discrete Dipole Approximation

The discrete dipole approximation (DDA) is a general method to calculate scattering and absorption of electromagnetic waves by particles of arbitrary geometry [38]. Although it has been employed as a highly reliable method in numerous studies, it is also time-consuming. In DDA, the particle is approximated by a regular lattice of electric dipoles separated by a fixed dipole spacing [35], and the interaction between dipoles are considered. In this study, a general function between DWR and particle size is needed, since the author hopes to focus in designing an information retrieval process for ice particles. Such a function based on DDA is currently not available in previous studies, and therefore DDA is not involved in this study. Further, DDA demands a lot of knowledge on the ice particles to provide the adequate scattering, while with our measurements, there's a lack of knowledge about which type of ice particles is measured. Because of this, DDA is often combined with in-situ measurements.

Models based on Rayleigh-Gans theory

Models based on Rayleigh-Gans (RG) theory are good approximations of Discrete Dipole Approximation (DDA) [39] in simulations of aggregates. With a physical microphysical model for simulating aggregation without priori assumptions about mass-size relation or size distribution, Westbrook et. al. found that some features of the aggregates are universal, which means they are not affected by the shape of size distribution of pristine ice crystals (monomers) that make up aggregates [39]. These features include a general relation between DWR and average radius of gyration, which is derived using Rayleigh-Gans theory. In RG theory, a particle is split up into small volume elements dV at position $\boldsymbol{r}$ relative to the overall centre of mass [39]. Each element is regard as a Rayleigh scatterer and the EM wave interactions between the elements are ignored. The microphysical properties of aggregates allow such simplification for typical radar frequencies and monomer sizes. The radar cross section of the whole particle is obtained by summing up the contributions from all elements with a phase factor [39]:

$$\sigma_r = \left(\frac{36\pi^3}{\rho_{ice}^2} \left| \frac{\epsilon - 1}{\epsilon + 2} \right|^2 \lambda^{-4} \right) m^2 f \tag{2.10}$$

where the form factor f is a function of $k = 2\pi/\lambda$ and r_g. r_g is the radius of gyration of the particle [39].

$$r_g = \left[\frac{\int_v |\boldsymbol{r}|^2 dv}{\int_v dv} \right]^2 \tag{2.11}$$

where $\boldsymbol{r}$ is the position of the volume element dv relative to the centre of mass of the aggregate. The form factor f represents the deviation from the Rayleigh regime when the size of the particle and the radar wavelength become comparable.

For a radar volume, the definition of the average radius of gyration is [39]:

$$r_{av} = (\Sigma m^2 r_g^2 / \Sigma m^2)^{1/2} \tag{2.12}$$

The authors of [39] fit a curve to the $f(kr_g)$ that they obtained from their computer simulations of ice aggregation. The curve combines the part of $f(kr_g)$ for relatively small particles and the part for larger particles. It leads to a formula with DWR, several constants and r_{av}, and therefore solving r_{av} using DWR is possible (Section 5.3). This relation between r_{av} and DWR is called Westbrook2006 later.

To apply RG theory, the particle cannot be too large or too strong a dielectric, otherwise the coupling between the elements can't be ignored. This indicates that it only works for particles with relatively low density (aggregates but not graupels) [39]. In [17], the authors retrieve particle size in ice cloud using the relation Westbrook2006 with sDWR. In [40], the bias of scattering properties when Rayleigh-Gans Approximation (RGA) is applied to aggregates of various degree of riming is evaluated by comparing with the scattering results from DDA. The authors conclude that: For Ka and W band, although for a single rimed aggregate the bias of backscattering cross section calculated by RGA can be quite large, the mean bias is relatively small (rarely exceeds 1dB, 26% difference) except the most heavily rimed snowflakes.

2.5. DWR-size relation

2.5.1. Comparison of DWR-size relation between RG and TM

As two possible options for retrieval of particle size, the model based on RG theory [39] is quite different from the model based on soft spheroid and T-matrix (SSTM) [41]. To compare, DWR-D_{max} relation are plotted (black curves, Figure 2.2) when the density of spheroid of SSTM is varied between 0.1 g/cm^3 to 0.25 g/cm^3 and aspect ratio (AR) is varied between 0.6 to 0.8, which are common values for aggregates. The DWR-D_{max} relation for Ka and W band from [39] is also plotted in the same figure (blue dash line, Figure 2.2).

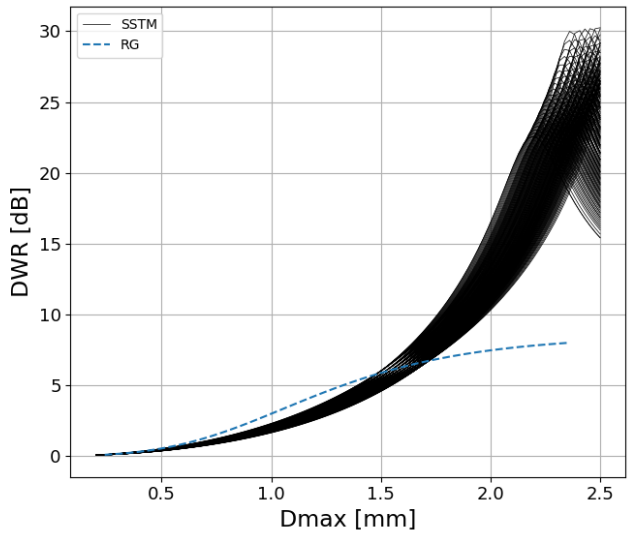

Figure 2.2: Comparison between DWR-Dmax relations of ice particles derived from RG theory and SSTM.

The discrepancy between two models after D_{max} reaching 1.6mm needs explanation. It was indicated in different studies that soft spheroid is not sufficient to characterize the backscattering properties of individual rimed and unrimed aggregates [42, 43]. According to [44], soft spheroid model systematically underestimates the backscatter for large aggregates. Additionally, a study has shown that when dealing with sizes that are large compared to the wavelength, the use of homogeneous spherical or spheroidal shape models leads to a misestimation of the backscattering cross section of snowflakes [45]. Besides, simulations show that DWR$_{KaW}$ for aggregates (ELWP$= 0.0kg/m^2$) and slightly rimed (ELWP$= 0.1kg/m^2$) aggregates reaches peak at a bit more than 8dB (Figure 2.3, green curve) as ice particles become larger ([42],fig. 5), which is similar to the dash curve of RG and different from the curves of SSTM in Figure 2.2. The curves of different colors in Figure 2.3 represent various degree of riming on aggregates, which is characterized by different effective liquid water path (ELWP) (kg/m^2) in the legend. Similar maximum DWR$_{KaW}$ values in triple frequency signature for unrimed aggregates are discovered in different forward modelling, including [31].

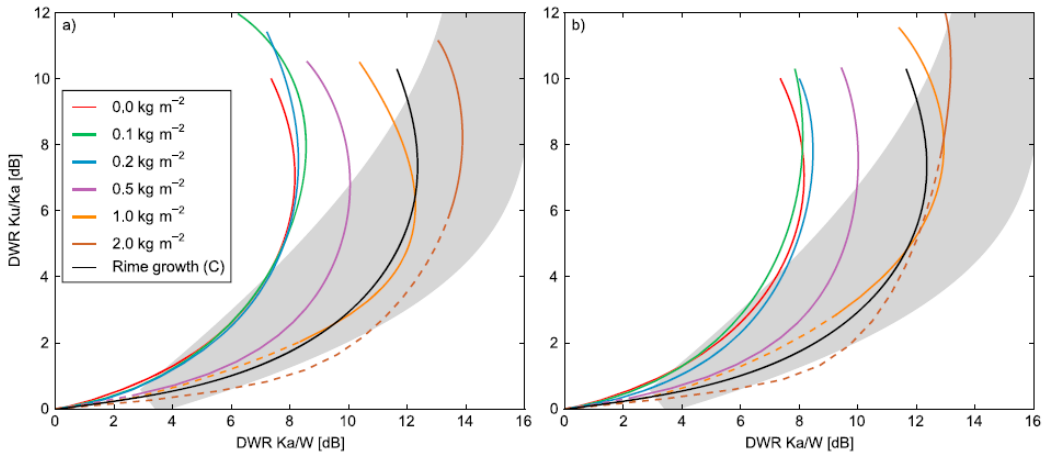

Figure 2.3: Triple frequency patterns from simulations (Leinonen, 2015 [42]). Left: Simultaneous aggregation and riming. Right: Aggregation followed by riming. Black curve in both sides: Only riming on pristine ice particles.

In Figure 2.3, the left figure displays triple frequency signatures from the scenario where the ELWP is evenly applied to the aggregate during aggregation. In the right figure, the aggregation process occurs without riming, and subsequently, all the ELWP is applied to the resulting aggregate [42]. The black curves in both left and right figures represent the condition when ice crystals or very small aggregates are rimed, with ELWP goes up to 6.0 kg/m^2. Figure 2.3 shows that as the degree of riming increases, the maximum value of DWR$_{KaW}$ also increases. [33] reaches similar conclusion and mentions that one of the reasons is that particles become more homogeneous in riming process, which is, to some extent, consistent with the SSTM curves in Figure 2.2 which exhibit large values for large particles compared to the RG curve. It's worth mentioning that slightly rimed aggregates (ELWP$= 0.1kgm^{-2}$) exhibit a triple frequency curve very close to unrimed aggregates in both situations (Figure 2.3 left and right).

In [33] the authors found different maxima in DWR$_{KaW}$ for aggregates of bullet rosettes and needles in their simulation. The former has a maxima of 8 to 12dB and the later of 7 to 8dB. However in radar observations it is not practical to distinguishing the components of aggregates, and therefore such difference is not going to be taken into account.

2.5.2. Feasibility of Using DWR-size relation in RG to slightly rimed aggregates

There's not direct conclusion about how slight rime affects the relation between DWR$_{KaW}$ and particle size in literature, though it's not expect to be significant. In figure 3 of [33] (Figure 2.4), simulated triple frequency signatures of aggregates of needles (b) and aggregates of bullet rosettes (e) from Self-Similar Rayleigh-Gans Approximation are shown, with varying density factor r_d (r in the figure) from 0 to 1. The thin black lines that cross the triple frequency curves represent the median volume diameter in the simulation from 1mm to 10mm. When r_d is equal to 0, it means that the mass-size relation in simulation is for aggregates [46] while r_d equal to 1 means that the mass-size relation is for solid ice. In figure 1 of [31], $r_d = 0.2$ is approximately corresponding to the aggregates with a m(D) relation (Leber17) derived from in-situ measurements while LWP=0-100g/m^2 [47]. Therefore, the curves with r_d equal to 0 and 0.2 in Figure 2.4 with indications of size reveal that the change of DWR$_{KaW}$-size relation is relatively small when low LWP presents. From the figure one can conclude that if a DWR-size relation for unrimed aggregates is applied to slight-rimed aggregates, an overestimation of size is possible.

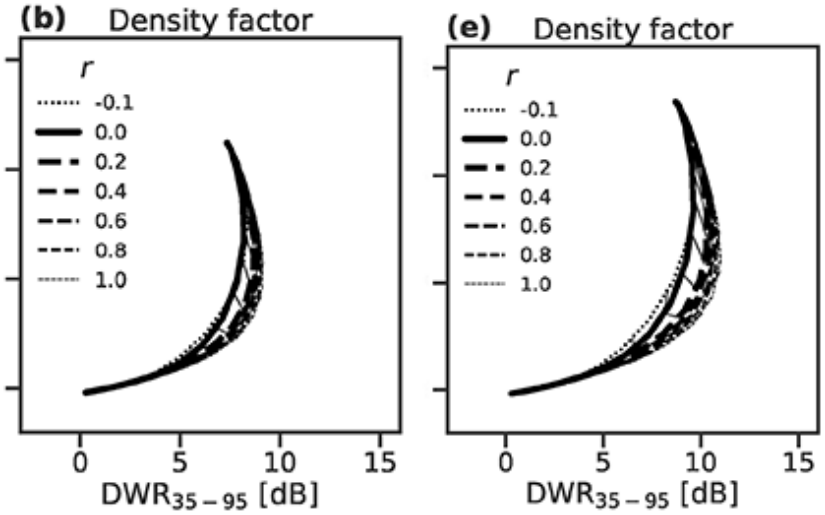

Figure 2.4: Triple frequency signatures of aggregates of needles (b) and aggregates of bullet rosettes (e) with varying density factor, (S.Mason, 2018 [33])

Another issue to settle is that former studies about DWR and aggregates are mostly based on vertically pointing radar, including the DWR-size relation from [39], the conclusions about rimed and unrimed aggregates from [42, 40] and many simulations related to the triple frequency signature. However, as mentioned in Section 2.1.2, the elevation angle of radar affects DWR [22] when large particles are non-spherical, which is what this study is facing with a slant-pointing radar. The authors of [22] shows cases that the effect of elevation angle can be ignored when ZDR is less than about 0.5dB. Therefore although cases with large ZDR are not actively avoided, it is preferred to have cases with small ZDR to limit the potentially large error. In practice, only the velocity bins with large sZDR are affected when spectra are exploited in retrieval. Considering mainly the aggregation process, usually small ice particles tend to have more non-spherical shape and large ZDR, but they're more likely to be within Rayleigh regime and therefore not affected by such issue.

2.6. Mass-size relation

The mass-size relation, or m(D) function, is a key theoretical property of ice particles. It is useful for describing the density of certain type of particle as a function of size and commonly used in microphysical retrieval of ice particles. The mass-size relation is critical in forward modelling because density is a key property affecting scattering properties.

In T-matrix, the mass-size relation of ice particles is chosen by the user as an input and assumption, but for more realistic microphysical models, m(D) is usually an output because it is determined by the microphysical process. Mathematical descriptions of internal structure can also determine the mass-size relation in another way, as what has been done in Self-Similar Rayleigh-Gans Approximation [44].

2.6.1. m(D) of unrimed aggregates

Initially, the m(D) function for aggregates was chosen to be power law based on in-situ measurements [48]. One popular version of such function is from [46] (BF95), which was derived from in-situ measurements in cirrus:

$$m(D_{mean}) = aD_{mean}^{b} \tag{2.13}$$

where D_{mean} (m) is the mean of the maximum chord lengths measured parallel and perpendicular to the probe photodiode array, a the prefactor and b the exponent (the fractal dimension). Notice that cirrus can contain ice particles with a wide range of size. Such form of m(D) function indicates that aggregates are fractal. More recently, idealized theoretical models of ice aggregation process were developed [49, 50], whose results also suggest that aggregates are fractal in geometry [51]. Therefore it is reasonable to consider general ice aggregates are fractal [39]. In [52] the authors proposed a correction form for BF95, considering that the original relation was not derived for common definition

of the maximum dimension of ice particle. The modified BF95 is shown below:

$$m = 480 D_{max}^3 \quad D_{max} < 6.6 \times 10^{-5} \tag{2.14}$$

$$m = 0.0121 D_{max}^{1.9} \quad D_{max} \geq 6.6 \times 10^{-5} \tag{2.15}$$

where m is mass in kilogram and D_{max} the maximum dimension in meter. As mentioned before, BF95 is derived for ice particles in cirrus, which is a kind of ice cloud at high altitude. For ice particles with D_{max} smaller than 6.6×10^{-5}m, modified BF95 assumes that particles are solid.

Other forms of mass-size relation for aggregates were also developed, such as the one based on [21] (Yang2000), which is hardly a power-law function (Equation 2.16 to Equation 2.18). In Yang2000, the melted volume V_{melt} (cm^3) of particles is calculated using the relation between melted-equivalent diameter D_v (cm) and maximum diameter D_{max} (cm) from [21]:

$$D_v = exp\left[\sum_{n=0}^{4} b_n (lnD_{max})^n\right] \tag{2.16}$$

$$V_{melt} = \frac{\pi}{6} D_v^3 \tag{2.17}$$

where b_n are 4 coefficients for aggregates in Table 2.1 [21].

b_0	b_1	b_2	b_3	b_4
-0.70160	0.99215	0.29322E-2	-0.40492E-3	0.18841E-4

Table 2.1: Parameters of D_v vs. D_{max} relation [21]

The particle mass m (g) is calculated based on its volume and density of water.

$$m = \rho_w V_{melt} \tag{2.18}$$

where $\rho_w = 1\ g/cm^3$ is the water density. The Yang2000 relation is based on simulated cirrus aggregates (arbitrary attachments of two to eight randomly selected hexagonal elements) and accurate single-scattering calculation [21].

In [18], the authors compare modified BF95 and Yang2000 in their retrieval process for snow. They found out that Yang2000 works far better with T-matrix than modified BF95 in retrieval of aspect ratio using T-matrix. Even so, they also suggest that the near-constant density provided by Yang2000 is suspicious while modified BF95 and other similar m(D) were confirmed in different in-situ measurements. However, the usage of power-law m(D) derived from in-situ measurements will result to unrealistically small retrieved aspect ratio. In conclusion, a satisfying m(D) function for all retrieval purpose is still debatable. Mass-size relation should be chosen according to the involved microphysical model in forward modeling, in order to produce a realistic scattering result. When T-matrix is used, to obtain reasonable aspect ratio from retrieval using ZDR, one should use Yang2000 instead of other power-law m(D).

2.6.2. m(D) of rimed aggregates

Heavily rimed ice particles are usually considered as solid ice in terms of density. For slightly rimed aggregates, one of the simulation results in [42] shows that the fractal dimension of slightly rimed aggregates is closed to unrimed aggregates (Figure 2.5). In term of density, the density of slightly rimed aggregates with $ELWP = 0.1 kgm^{-2}$ can be 3-5 times higher than unrimed aggregates (Figure 2.5 left and right, red and green line).

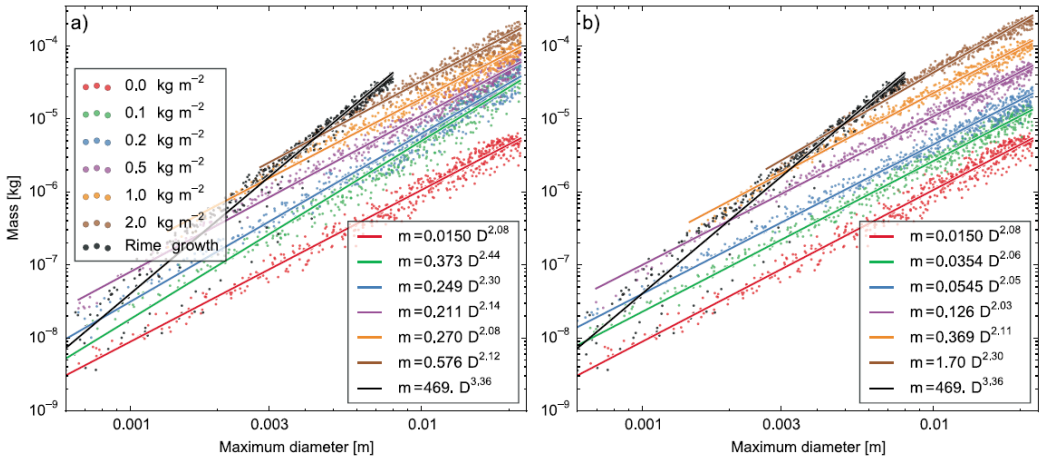

Figure 2.5: Mass-size relation for the same settings as Figure 2.3, Leinonen, 2015 [42]. Left: Simultaneous aggregation and riming. Right: Aggregation followed by riming. Black curve in both sides: Only riming on pristine ice particles.

It was mentioned in [53] that in the early riming stage the fractal dimension can be considered unchanged (close to 2) while the prefactor increases. The authors of [53] also provide a summary of different m(D) functions (Figure 2.6). The m(D) relations for aggregates fall in a relatively small range (dark grey region), while for rimed snow (light grey region) the uncertainty is larger. These two regions are right next to each other.

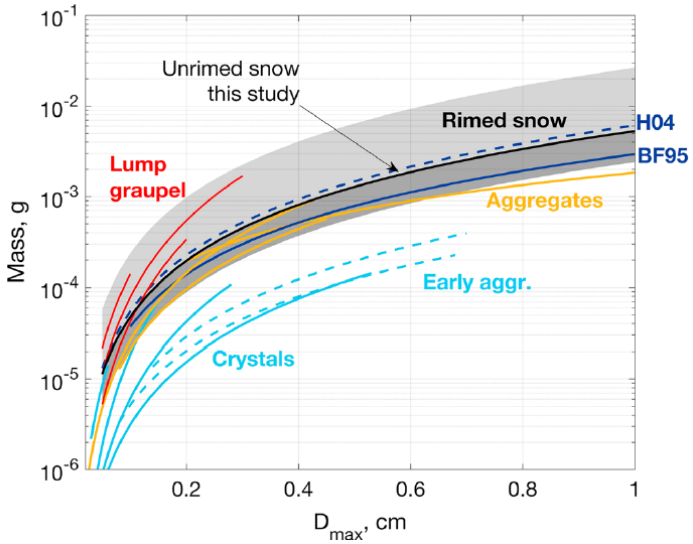

Figure 2.6: Summary of m(D) function from D.Moisseev, 2017 [53]. The dark grey region represents the range of m(D) for aggregates, while the light grey region represents m(D) for rimed snow.

An m(D) relation (Lerber17) was derived from unrimed to slightly rimed snow cases (LWP$= 0 \sim 100 g/m^2$) using measurements in snow events from the Biogenic Aerosols–Effects on Clouds and Climate (BAECC). It is shown in Equation 2.19:

$$m = 0.0046 D_{max}^{2.1} \tag{2.19}$$

where m is mass in gram and D_{max} the maximum dimension in centimeter. The minimum observable particle size in BAECC data is 0.28mm, which is much larger than the minimum ice crystal size in Yang2000 (3-5μm) and BF95 (0.1mm).

To summarize, the three m(D) introduced above are shown in Table 2.2.

m(D)	Scenario	Origin	min Size
(modified) BF95	cirrus	in-situ measurement	0.1mm
Lerber17	slightly-rimed snow	in-situ measurement	0.28mm
Yang2000	cirrus	simulation	3-5μm

Table 2.2: Characteristics of different m(D)

Although it's obvious that different m(D) is needed for different degree of riming, different type of ice particles or different ice growth processes, there's no conclusion about what kind of m(D) is most suitable for microphysical retrieval in low-LWP MPC.

2.7. Bulk and Spectral Retrieval

There are two types of DWR applications to retrieve size information for ice particles using radar measurements, bulk and spectral retrieval (BR and SR). They can be applied to the retrieval of other quantities with other radar measurements as well. Bulk retrieval involves making retrievals using height-time profiles of radar measurements, such as retrieving the median size diameter or median mass diameter for a radar volume with DWR in earlier research. It's previously used for radar that can't provide spectral reflectivity [54, 55] but can also applied to radar with spectra measurements [18]. T-matrix is usually used to determine the DWR-size relation in these studies since it is considered adequate for characterizing bulk scattering properties of ice particles [18]. Another way to make retrieval is to assume that each velocity bin of Doppler spectra contains one type of ice particles with the same properties [17]. In this case, sDWR is used to derive the particle size for each velocity bin.

In this study, the second approach is mainly applied for the following reasons: Using Doppler spectra can make the most use of the information obtained by our radar. It allows detailed description of ice particles within a radar volume and reserves the possibility of distinguishing different types of ice particles. Therefore, it allows the retrieval of particle size distribution. This is particularly meaningful when MPC, where a wide range of ice particles exist, is being studied. However, it also requires high sensitivity of radar at both frequencies to obtain high-quality Doppler spectra. The bulk retrieval is considered as a substitution of spectral retrieval if the quality of spectra is not satisfying. Besides, bulk retrieval can directly provide the retrieved height-time profiles.

2.8. Conclusion

This chapter firstly introduces three types of radar measurements which will be used in this research. Then the manners to deal with differential scattering and attenuation contribution in DWR in ealier studies are illustrated. Later it reviews previous radar observations of MPC. Three scattering models are introduced with an emphasis on Rayleigh-Gans theory and the DWR-size relation based on it. For ice aggregates, the Westbrook2006 (based on RGA) is found to be better than DWR-size relation derived from T-matrix. The slightly-rime effect on DWR-size relation should be limited, while the effect on m(D) is evident. However, being close to reality is not the only important criterion for choosing a m(D) for microphysical retrieval because the accuracy of retrieval results can be more important. Although microphysical retrieval is challenging due to the various properties of unrimed and rimed particles affecting the process from start to finish, it can still be accomplished with acceptable error in slight-rime conditions.

3

Data

3.1. Radar measurements

The radar measurements are obtained from a dual-frequency polarimetric scanning cloud radar (CLARA) located at atmospheric station in the national Ruisdael Observatory, Cabauw. The radar operates simultaneously with two frequencies (35GHz and 94GHz), providing Doppler spectra of polarimetric measurements for the same radar volumes along the radar beam. The radar was working in hybrid mode, which means it was emitting radiation of fixed linear polarization oriented at 45° with simultaneous reception of horizontal and vertical polarized back scattered signal components [20]. Detailed description of the part of radar working at 94GHz can be found in [56]. The temporal resolution of the radar measurements is 3 or 4 seconds with the average time being about 3.6 seconds.

The radar was working with an elevation angle of 45.01° and a fixed azimuth direction. Different settings were used in different chirps, which are shown in Table 3.1. The setting for two frequencies are different in term of maximum Doppler velocity and velocity resolution.

	Chirp 1	Chirp 2	Chirp 3
FFT size	256	256	128
Height intervals [m]	84-843	864-3458	3503-10587
Range resolution [m]	29.81	29.81	55.04
94GHz			
Maximum Doppler velocity [m/s]	7.35	5.99	3.97
Doppler velocity resolution [m/s]	0.0576	0.0470	0.0625
35GHz			
Maximum Doppler velocity [m/s]	19.73	16.08	10.66
Doppler velocity resolution [m/s]	0.1548	0.1261	0.1678

Table 3.1: Chirp Settings of the radar

There are two levels of product of radar measurements: LV0 products contain Doppler spectra at horizontal and vertical polarization as well as covariance spectra, while LV1 products contain mean Doppler velocity, correlation coefficient, differential phase shift and differential reflectivity profiles [57]. A pair of LV0 and LV1 files are produced by the radar each hour.

Besides, the radar also provides LWP measurements by two receiving antennas (which are not the same as radar receivers). One of the antennas receives radiation at 89GHz and the other at 31.4 GHz. Initial usage of the two LWP indicates that the LWP at 31.4 GHz was not reliable (drift) due to uncertain reasons, and therefore only the LWP at 89GHz is utilized. The noise level of this LWP measurement is $10g/m^2$.

3.2. Microwave radiometer

The microwave radiometer located near the radar is RPG-HATPRO. It works on two bands (22-31GHz and 51-58GHz) and provides information about humidity and temperature, among which vertical temperature profiles are mainly used in this study. The radiometer was pointing towards the zenith. The temperature profiles have 93 height bins with the height ranges from 0 to 10000 meters. The height resolution decreases from 10m to 200m as altitude increases. The vertical LWP measured by radiometer is also used as a reference to LWP measured by radar receiver (slant-view).

3.3. NWP model results

The model results from ECMWF were used in this study for calculation of gas differential attenuation, which includes relative humidity profiles, air pressure profiles and temperature profiles at Cabauw with horizontal resolution of 9km and temporal resolution of one hour. The altitude of the profiles starts from about 9m to 76000m and the vertical resolution decreases from about 20m to about 300m within the lowest 10000m. The data can be obtained from CloudNet data portal (https://cloudnet.fmi.fi/) [58].

4

Scattering simulation results

Simulation results from T-matrix are shown in this chapter, since they help illustrate the logic behind the methodology. It is crucial to know how microphysical properties, such as size, density and aspect ratio of ice particles affect radar measurements of ZDR and ZE.

The simulations are carried out with PyTmatrix package in Python [41]. The microphysical model is soft spheroid and the scattering model is T-matrix. The simulations below (except DWR) are made for Ka band (35GHz), since only radar reflectivity and ZDR at Ka band will involve in methodology development and therefore need to be studied. In these single particles simulations, the particle is oblate when aspect ratio (AR) is less than 1 and prolate when AR is larger than 1. The zenith angle of incident beam and scattered beam are set as $45°$ and $135°$, which represents the observing geometry of our radar. The orientation of ice particles are described by Euler angle α and β in PyTmatrix (Figure 4.1). For oblate particles, the Euler angles are kept zero. Therefore in all the simulations, the maximum dimension of the particle is perfectly aligned with the horizontal plane and the variation of canting angle is not considered.

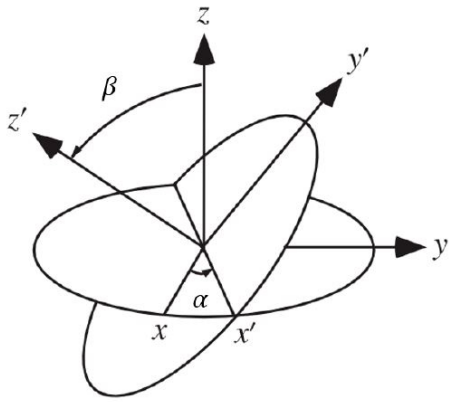

Figure 4.1: The Euler angle α and β

The Maxwell-Garnett effective medium approximation is exploited in PyTmatrix to calculate the refractive index of a particle containing ice-air mixture using the refractive index of pure ice and pure air. It takes in the volume fraction of ice f_{ice} as input, but in this study it is the density of ice particle that is being studied. To convert density into volume fraction of ice,

$$f_{ice} = \frac{\rho - 1}{\rho_{ice} + \rho - 1} \tag{4.1}$$

where ρ is the density of ice particle and $\rho_{ice} = 0.9167\ g/cm^3$ the density of pure ice.

4.1. DWR

Although soft spheroid model lacks internal structure of ice particle, T-matrix is still able to show how density affects DWR-size relation for homogeneous particles. Figure 4.2 shows different DWR-size relations for constant density and density computed by different m(D) relations when aspect ratio$= 0.6$, a representative value for aggregates [31]. Model A ELWP$= 0.1kg/m^2$ (MA1, simultaneously aggregation and riming, dash dot line) and model B ELWP$= 0.1kg/m^2$ (MA2, first aggregation and then riming, dash line) are the same scenarios as Figure 2.3, whose m(D) relations are shown in Figure 2.5 left and right. The curve for unrimed aggregates (solid black line) is the same scenario as the one with zero ELWP in Figure 2.5. Yang2000 relation (dots) is described in Equation 2.16 to Equation 2.18. One can conclude that the curves of particles with larger density is closer to zero when D_{max} is small, but the DWR increases faster as D_{max} increases and enters Mie regime with a smaller D_{max}. Thus in Figure 4.2, MA1 has a larger density at all size, while the curves of MB1 and unrimed aggregates are very close to each other. The curve of Yang2000 is quite similar to the curve with density equal to $0.2\ g/cm^3$. Overall, the density of ice particle can greatly affect the DWR-size relation.

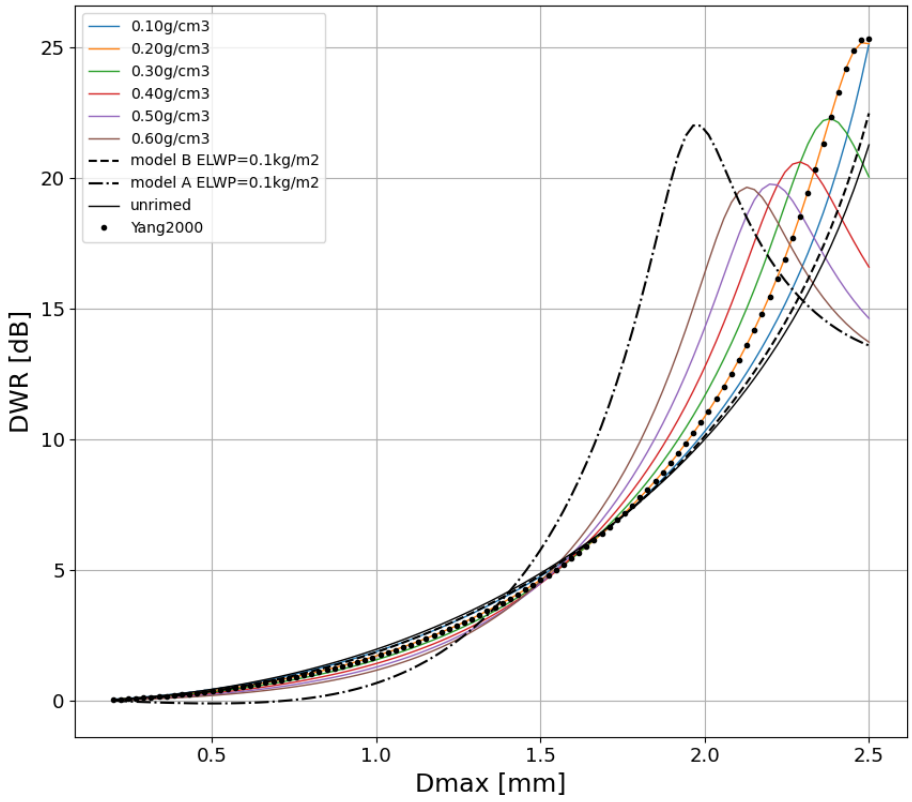

Figure 4.2: DWR-D_{max} relations simulated by T-matrix for various m(D)

The relations shown in Figure 4.2 are not used in retrieval of particle size, since Westbrook2006 is considered more realistic (Section 2.5.1). However, the advantage of T-matrix is that the microphysical properties such as density and AR can be conveniently changed without knowing the realistic details of ice particles. Thus it provides an simple approach to study the sensitivity of radar measurements to microphysical properties.

4.2. ZDR

Simulation results of ZDR versus D_{max} with different constant density and aspect ratio are shown in Figure 4.3. In Figure 4.3 left, the ZDR of $\rho = 0.1g/cm^3$ is nearly a constant as the size increases, while for large density as $\rho = 0.6g/cm^3$ ZDR increases about 0.2dB as the D_{max} increases. Figure 4.3 right shows similar curves but with larger ZDR because of the smaller AR. Overall, Figure 4.3 shows that density can greatly affect the value of ZDR, which means it has to be taken account for. In contrast, the size of particle has little impacts on ZDR with low density. The size effect on ZDR should come from Mie scattering. The higher the density, the more the particle size affects ZDR.

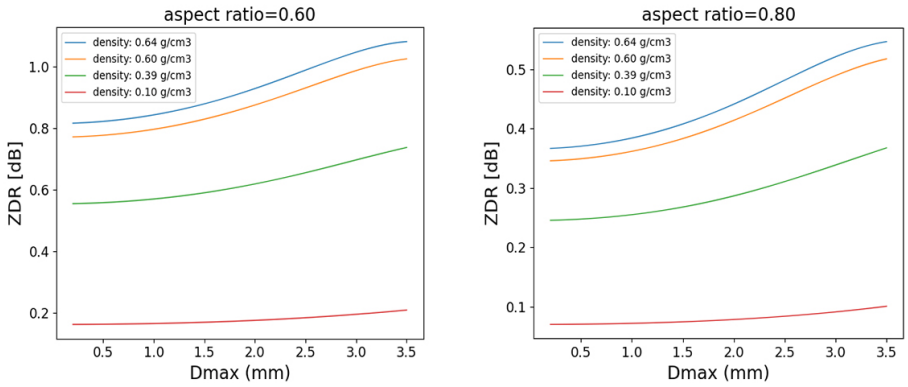

Figure 4.3: D_{max} vs. ZDR with different density. Left: AR=0.6. Right: AR=0.8

The relation between ZDR, density and AR is shown in Figure 4.4. It is shown that AR and density both contribute to ZDR. As the aspect ratio increases from 0.5 to 0.8, ZDR decreases from more than 1.1dB to 0.4dB when the density is $0.6g/cm^3$, while ZDR decreases from 0.25dB to less than 0.1dB when the density is $0.1g/cm^3$. For particle with the same density, smaller AR causes larger ZDR. For particle with the same AR, larger density causes larger ZDR.

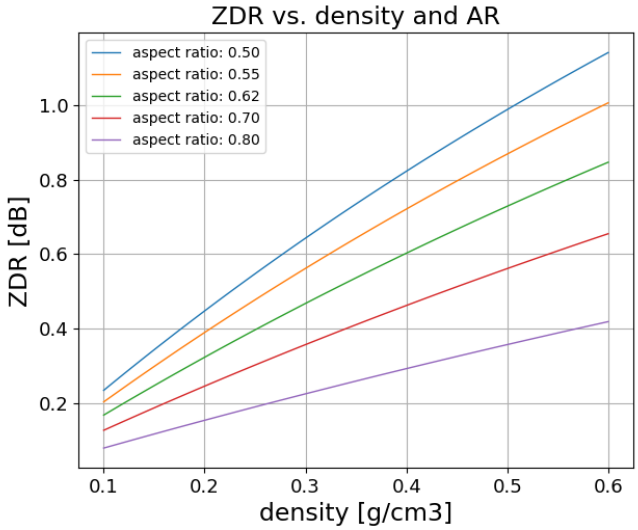

Figure 4.4: ZDR vs. density and AR for oblate particles

In Figure 4.5, ZDR versus density with aspect ratio varied from 0.7 to 1.2 is shown. Figure 4.5 indicates that a prolate particle with the maximum dimension in horizontal plane is not distinguishable from oblate particles by ZDR, since their ZDR are within the same range. In Figure 4.5 , the purple and red curves, representing prolate particles, include the range of ZDR for oblate particles (Blue, orange and green curves).

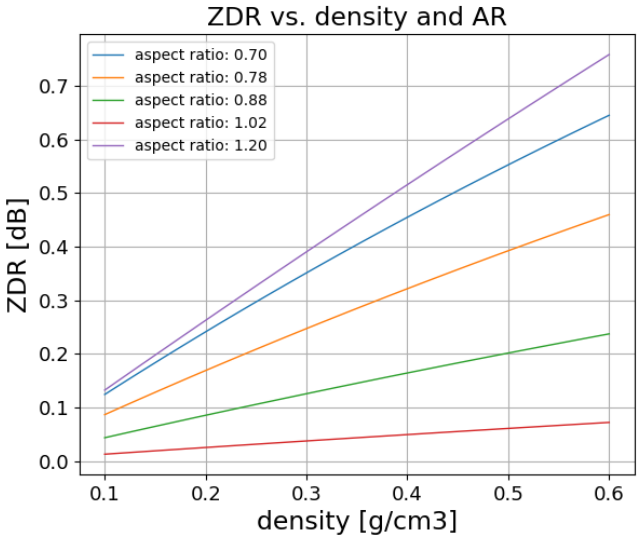

Figure 4.5: ZDR vs. density and AR for oblate and prolate particles

4.3. ZE

In the simulation of reflectivity, the m(D) function involved is Yang2000 (Equation 2.16 to Equation 2.18). For the right figure, the Euler angle α and β of the spheroid are 0 degree when AR is smaller than 1. When AR is larger than 1, α and β are both 90 degree. In Figure 4.6 left, ZE versus D_{max} with constant AR is shown. The radar reflectivity increases from about -60dB to more than 5dB as maximum dimension increases from 0.2mm to 3.5mm. In Figure 4.6 right, ZE versus AR with different D_{max} is shown. The radar reflectivity almost remains constant as AR increases, regardless of the value of D_{max}. For large particles ($D_{max} = 3.5mm$), the reflectivity decreases as AR increases when AR is less 1 while it's the other way around when AR is larger than 1. Overall, Figure 4.6 indicates that reflectivity is much less sensitive to AR than size and mass.

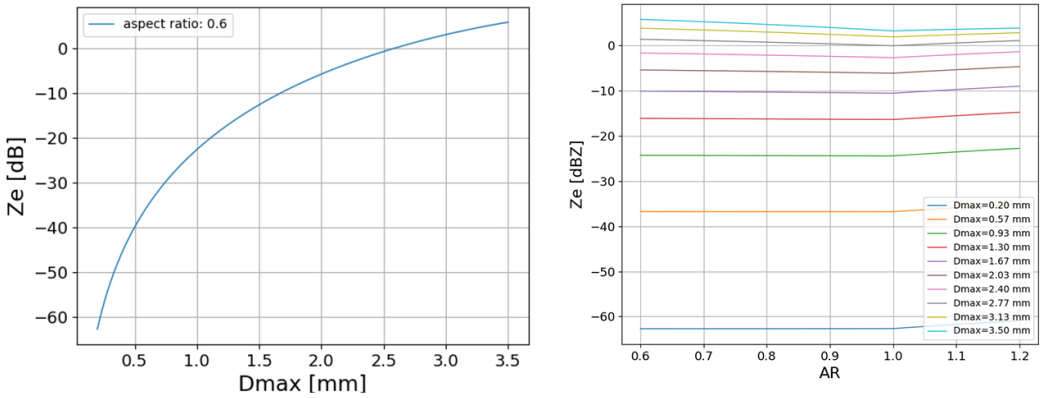

Figure 4.6: Left: Reflectivity vs. Dmax with constant AR=0.6. Right: Reflectivity vs. AR for different Dmax (0.2mm to 3.5mm)

For a fixed AR equal to 0.6, the radar reflectivity is simulated for different density and particle size (Figure 4.7 left). Similar figure is made for AR equal to 0.98 (Figure 4.7 right). One can conclude that the dependency of radar reflectivity on density is strong for a given size.

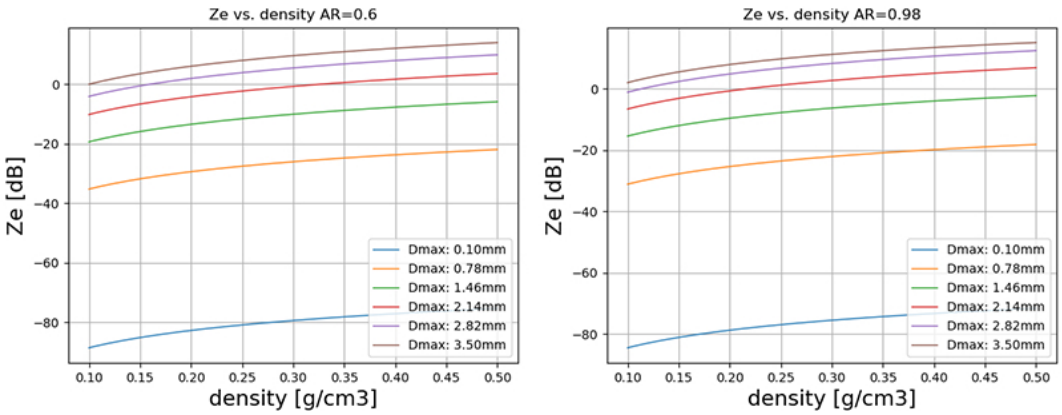

Figure 4.7: Radar reflectivity vs. density with D_{max} ranging from 0.1mm to 3.5mm. Left: AR=0.6 Right: AR=0.98

4.4. Conclusion

From the simulation results in this chapter, one can conclude that density is an important factor affecting DWR-size relation. Density and aspect ratio both affects ZDR, but one cannot distinguish prolate particles from oblate particles using ZDR. Therefore, density and AR should be considered simultaneously when making use of ZDR in retrieval of microphysical properties. The radar reflectivity is primarily influenced by density and size, with a minor impact from aspect ratio.

5

Methodology

As discussed in Chapter 4, radar measurements are affected differently by microphysical properties of ice particles. These differences observed using scattering simulation will be exploited to build the proposed retrieval process in this chapter. To retrieve 4 microphysical properties (size, density, aspect ratio and number concentration) of ice particles one will need four different inputs, but there are only DWR, ZDR and ZE from radar measurements. Thus, the introduction of m(D) is required, which can provide controllable extra information, given the extensive studies of mass-size relations for aggregates.

The main structure of retrieval procedure is shown in Figure 5.1, with the inputs and outputs of each step. The entire retrieval process takes in Doppler spectra and is based on an assumption that each velocity bin in spectra contains a number of identical particles. The retrieval procedure can also be applied to integrated radar measurements (bulk variables) without any modification. In that case the assumption will be that all particles within a radar volume are identical.

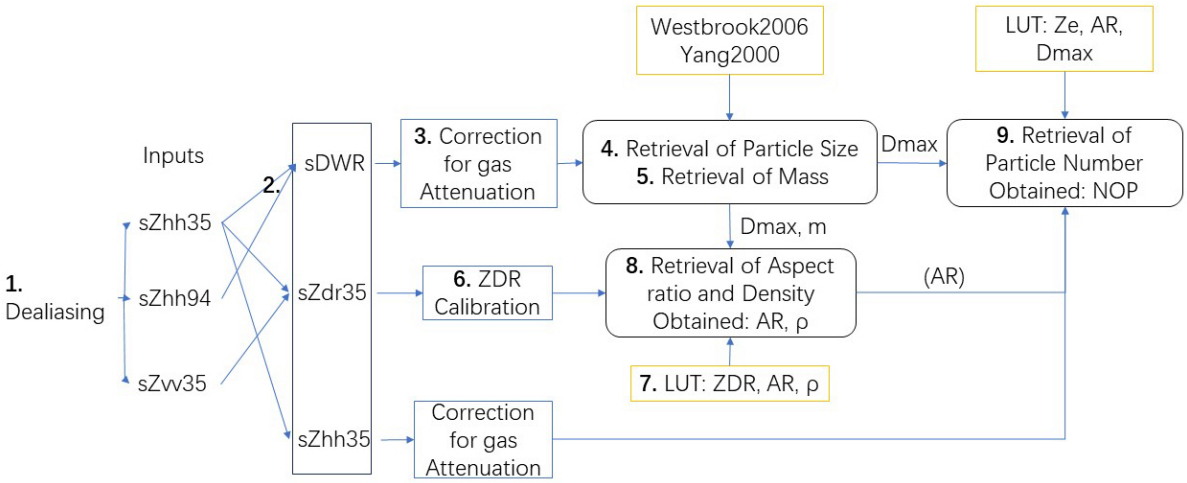

Figure 5.1: The retrieval procedure of microphysical properties of ice particles at spectral level for a MPC characterized with low LWP.

At the beginning of the retrieval, MPC events with small LWP are identified. The key steps afterwards are listed below with the numbers corresponding to those in Figure 5.1:

1. The Doppler spectra $sZ_{hh,35}$, $sZ_{hh,94}$ and $sZ_{vv,35}$ are dealiased [57].
2. sDWR is calculated using $sZ_{hh,35}$ and $sZ_{hh,94}$. (Section 5.2.1)
3. Gas attenuation is corrected for sDWR. (Section 5.2.2)

4. (Section 5.3) Choosing to exploit the DWR-size relation of Westbrook2006 for particle size retrieval is a good option to set aside other contributions (e.g. density, internal structure) without introducing too much bias, as explained in Chapter 2 and Section 5.3.
5. After this, it is natural to utilize a preferred m(D) relation to derive particle mass. Up to this point some constraint (minimum density) of particle density is obtained.
6. sZDR is calibrated. (Section 5.4.1)
7. The look-up table of ZDR is built. (Section 5.4.2)
8. Then calibrated sZDR is introduced to retrieve density and aspect ratio at the same time. (Section 5.4.3)
9. The gas attenuation corrected sZ_{hh} at 35GHz is further introduced to retrieve number concentration of particles. This step doesn't necessarily need aspect ratio (AR) as input because of the lack of sensitivity of reflectivity to AR shown in Section 4.3. (Section 5.5)

Although some steps are not listed above, they are also described in following sections. The height-time profiles can be calculated after the whole program is finished. The m(D) relation is employed twice in the entire procedure: initially when calculating mass using D_{max}, and subsequently when constructing a look-up table for radar reflectivity in number concentration retrieval. After the retrieval, IWC (Section 5.6) and PSD (Section 5.7) are further derived. The error caused by ignoring supercooled liquid is estimated from a simulation (Section 5.8).

5.1. Determination of MPC cases

The MPC is considered to be a cold cloud with positive LWP when there's no liquid cloud or precipitation near the ground. The temperature profiles obtained from microwave radiometer are used to distinguish between liquid clouds and ice clouds. If a cloud exists at temperature below zero degree Celsius, it definitely contains ice particles, while a cloud present at positive temperature should be a liquid cloud. An ice cloud present with positive LWP without any reflection at positive temperature region is considered to be a MPC. In this study in order to limit the error caused by liquid differential attenuation in DWR, only MPC cases with LWP less than $100g/m^2$ are selected. This value is based on the simulation made in [42, 40]. In the simulation [42] for slightly rimed aggregates, the effective liquid water path (ELWP) is set as $100g/m^2$. The ELWP for riming is always smaller than or equal to LWP for riming, and therefore their findings that matter for this study hold when LWP is less than $100g/m^2$. One should note that the LWP from radar receiver is slant LWP with an elevation angle of 45.01°. It is used to select MPC events, and therefore the actual vertical LWP might be even smaller than $100g/m^2$. Besides, to reduce the error of applying the DWR-size relation derived for vertically-pointing radar on our radar with an elevation angle of $45°$, events with small ZDR are preferred, based on the findings from [22]. This selection of MPC cases at low LWP is carried out prior to the retrieval procedure of Figure 5.1.

5.2. Calculation and Correction of sDWR

The core of this methodology is the usage of sDWR. It can provide crucial information about particle size, but it requires at least the exclusion of differential attenuation of gases. The Doppler spectra of the selected events are dealiased using the algorithm from [57], including horizontally and vertically polarized radar reflectivity at 35GHz and sZ_{hh94}.

5.2.1. Calculation of sDWR

As described in Chapter 3, the Doppler spectra at 35GHz and 94GHz have different Doppler velocity resolution dv and Nyquist velocity. 94GHz spectra have higher Doppler velocity resolution and smaller Nyquist velocity. Therefore interpolation for spectra of one frequency is needed before sDWR can be calculated, as mentioned in [17]. It is expected that the interpolation can be applied to the spectral reflectivity of any one of the two frequencies without much difference, because the information contained in sDWR is limited by the spectra with less information.

The parts of spectra with power smaller than the noise level are removed. Then the spectral reflectivity at 94GHz sZ_{hh94} (red curve in Figure 5.2) is linearly interpolated at the velocity bins of the spectra at 35GHz (black curve in Figure 5.2). The dash lines in Figure 5.2 represent the interpolated values.

The marks on both curves represent the division of velocity bins. Usually, the sZ_{hh94} is expected to be narrower than sZ_{hh35} due to less sensitivity at 94GHz. Since only the common parts of two spectra are kept and used for sDWR calculation, the extra parts of sZ_{hh35} are removed.

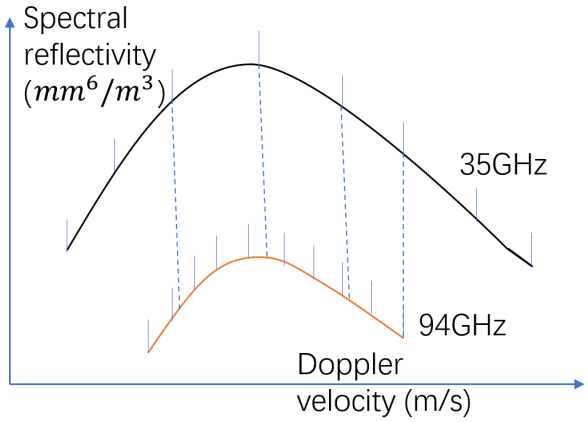

Figure 5.2: Schematic diagram of interpolation of the 94GHz spectra

To account for the difference in Doppler velocity resolution, the interpolated spectral reflectivity $sZ_{hh94,int}$ is multiplied by dv_{35}/dv_{94} and the unit of $sZ_{hh94,int} \times dv_{35}/dv_{94}$ is still mm^6/m^3. In short, the sDWR is calculated by:

$$sDWR = 10log_{10}\frac{sZ_{hh35,clipped}}{sZ_{hh94,int} \times dv_{35}/dv_{94}} \tag{5.1}$$

where $sZ_{hh35,clipped}$ is the common part of sZ_{hh35}. The DWR is calculated as:

$$DWR = 10log_{10}\frac{\sum^{entire\ spectrum} sZ_{hh35,clipped}}{\sum^{entire\ spectrum} sZ_{hh94,int}} \tag{5.2}$$

5.2.2. Correction for gas attenuation

As mentioned in Section 2.1.2, DPIA and Mie scattering contribute to DWR. The DPIA of air at all radar range can be estimated, knowing air pressure, temperature and absolute humidity. The output profiles from a ECMWF model at Cabauw are used (Section 3.3). The saturation vapor pressure P_s (Pa) is calculated using temperature T (K) profiles:

$$P_s = 610.78\ exp(17.2694(T - 273.16)/(T - 35.86)) \tag{5.3}$$

Absolute humidity (AH) (kg/m^3) is calculated using relative humidity RH, saturation vapor pressure P_s and temperature T:

$$AH = \frac{RH \times P_s}{R_w \times T \times 1000} \tag{5.4}$$

where $R_w = 461.5$ (J/kg/K) is the specific gas constant for water vapor. Matlab provides a function that can calculate specific attenuation $\alpha_{att,\lambda}$ (dB/m) using inputs mentioned above according to [59]. The DPIA (dB) caused by gases at height h is then:

$$DPIA_{gases}(h) = 2\int_0^h (\alpha_{att,94GHz,gas}(s) - \alpha_{att,35GHz,gas}(s))ds \tag{5.5}$$

The fact that our radar was pointing at $45°$ elevation angle means that $DPIA_{gases}$ needs to be divided by $sin(45°)$ to account for longer travelling distance of radar signal (Equation 5.6). The $DPIA_{gases}$ at all radar ranges are then subtracted from corresponding sDWR and the negative sDWR after subtraction are removed:

$$sDWR(r) = sDWR_{att}(r) - DPIA_{gases}(h)/sin(Elv) \tag{5.6}$$

where Elv is the elevation angle of radar. This means that DPIA from ice particles and potential liquid still exists in sDWR. Further, one should notice that the profiles from ECMWF are of low resolution in time and space, and therefore also bring some error.

5.3. Retrieval of Particle Size and Mass

After the correction of sDWR, the average radius of gyration r_{av} (m) is retrieved from sDWR using the relation proposed in [39] (Westbrook2006):

$$a'(4r_{av}^2)^3 + b'(4r_{av}^2)^2 + c'(4r_{av}^2) + d' = 0 \tag{5.7}$$

where:

$$a' = c_1 c_2 k_1^2 k_2^2 (B\ k_1^2 - k_2^2) \tag{5.8}$$
$$b' = c_2 (B\ k_1^4 - k_2^4) \tag{5.9}$$
$$c' = c_1 (B\ k_2^2 - k_1^2) + (c_1 + 1/3)(B\ k_1^2 - k_2^2) \tag{5.10}$$
$$d' = B - 1 \tag{5.11}$$

where $c_1 = 12.7$, $c_2 = 4.5$ [60] and B is the linear value of DWR with DPIA corrected. k_1 and k_2 (m^{-1}) are the wave numbers of two radar wavelengths:

$$k_i = \frac{2\pi}{\lambda_i} \quad (i = 1, 2) \tag{5.12}$$

Equation 5.7 is a polynomial equation in one variable. The minimum real and positive solutions of Equation 5.7 are taken as r_{av}. The solution of Equation 5.7 versus DWR$_{KaW}$ is shown below:

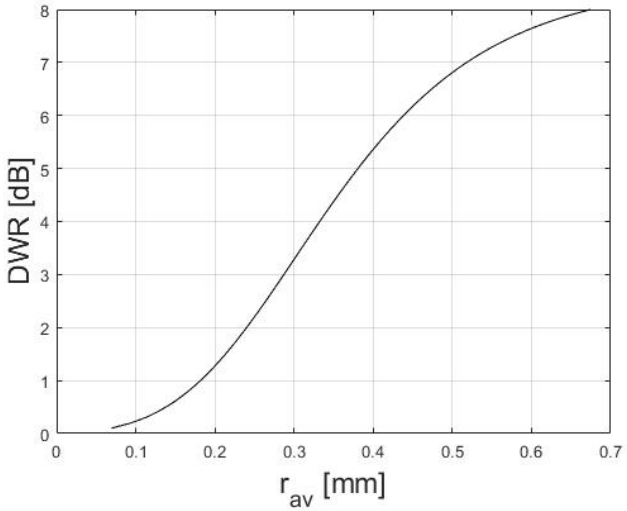

Figure 5.3: r_{av} vs. DWR$_{KaW}$ solution in Westbrook, 2006 [39]

The retrieved r_{av} is also a spectrum similar to sDWR. The r_{av} is then converted into the maximum dimension D_{max} by [42]:

$$r_{av} = 0.287 D_{max} \tag{5.13}$$

Although in [42] the concluded relation (Equation 5.13) is for r_g and D_{max}, here it is used for r_{av}. In [39], $r_g \approx 0.3 D_{max}$. The Equation 5.13 is preferred because it looks more accurate, while the difference between r_{av} and r_g is expected to be small within the same velocity bin. Saturation can be seen in the curve when DWR approaches maxima (Figure 5.3). The maximum allowed DWR for Ka and W band in Westbrook2006 is between 8.5dB to 8.6dB. The cutoff value is set as 8.5dB currently to retrieve as much size as possible. Any sDWR beyond this value will be considered invalid and removed. A small cutoff value can reduce the uncertainty of retrieved size when DWR is large, but it leads to the loss of number of bins with retrieved size. A cutoff value of 8dB allows the maximum retrieved D_{max} to be about 2.35mm, while 8.5dB allows maximum D_{max} to be about 3.38mm. Besides, there's no limit to the minimum retrieved size. Mixed-phase clouds are usually mid-level clouds such as altostratus

or altocumulus, though cirrocumulus, a kind of high-level cloud, can also be MPC. Based on previous in-situ observations, the ice particles within altocumulus rarely have D_{max} larger than 2mm, while for altostratus the D_{max} can sometimes go up to 3mm but rarely to 4mm [61, 62]. Therefore DWR$_{KaW}$ should be able to characterize the size of ice particles in most cases, though the accuracy for large particles will be lower.

The minimum input of sDWR is 0dB. In the simulation used to derive Westbrook2006, the rescaled size of aggregates are used [63], but one can conclude that the minimum size of those aggregates used to derive Westbrook2006 is no less than 100μm based on figure 2 in [63] and information given in [64]. What really matters to the lower limit of Westbrook2006 is that the aggregates involved are fractal, while it is mentioned in [64] that aggregates of 'a handful of monomers' are enough to exhibit the fractal property (self-similarity). However, the fact that the sensitivity of radar at 94GHz is lower than that at 35GHz means that the smallest particles probably don't have sDWR above noise level. Thus, the chance that Westbrook2006 is applied to ice crystals that are too small (aggregates comprise fewer than 3 crystals) in Doppler spectra is low.

In mass retrieval, the preferred m(D) is Yang2000 because it works better than a power-law m(D) with T-matrix for the retrieval of AR [18], as mentioned in Section 2.6.1. In this case, the priority is to obtain reasonable AR instead of reliable mass and density. This trade-off is worthwhile because the options to obtain correct AR for aggregates are limited. The retrieved D_{max} is used as an input and the mass of particles is obtained.

5.4. Retrieval of Aspect ratio and Density

Spectral differential reflectivity sZDR at 35GHz is introduced in order to retrieve aspect ratio (AR) and density of ice particles using Doppler spectra.

5.4.1. ZDR Calibration

sZDR is calibrated using the calibration result from [65]. The calibration value (dB) is a vector containing corrections for each radar range which need to be subtracted from original sZDR (Figure 5.4 left). The value of such calibration ranges from about -0.16dB to -0.22dB while the distance from radar ranges from 111m to 8322m. When the radar is pointing at the elevation angle of 45°, the calibration can only be applied to the data with height less than about 5886m.

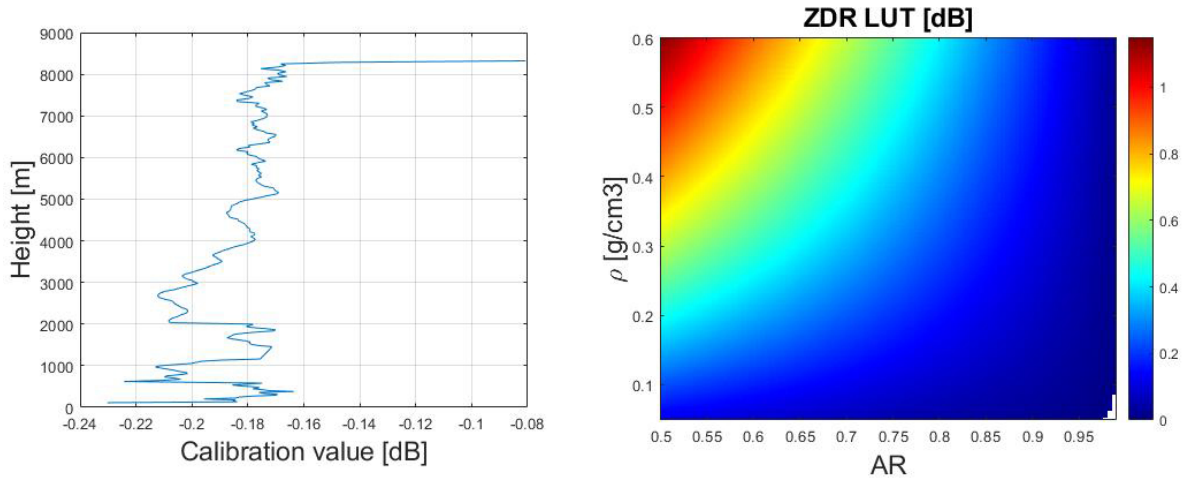

Figure 5.4: Left: Calibration value of ZDR when radar is pointing towards the zenith [65]. Right: example of LUT of ZDR.

The calibration is important because the error in ZDR measurements results to many negative values in sZDR. Those velocity bins originally have positive sZDR close to zero, which is quite common for large ice particles like aggregates. After subtracting the calibration value from original sZDR, the

negative sZDR is removed because the retrieval process doesn't handle this rare case. The calibration is not expected to be perfect because it was obtained from the observations made several months after the MPC events used in this study.

The retrieval of AR and density of ice particles is based on simulation results. Soft spheroid is used to represent ice particles and the scattering model is T-matrix. AR and density are solved in the same iteration process.

5.4.2. Look-up table

A look-up table (LUT) of ZDR is built using the simulation results from PyTmatrix library in Python environment similar to Chapter 4. The ranges and steps of AR and density were determined before simulation of ZDR of an spheroid ice particle. The AR ranges from 0.2 to 0.99 with 400 steps while the density ranges from $0.05g/cm^3$ to $0.6g/cm^3$ with 200 steps. The maximum dimension of ice particle is set as 1mm, as previous simulation shows that particle size doesn't have significant impact on ZDR (Figure 4.3), especially for particles with low density like aggregates. The density of aggregates in this research is expected to be smaller than 0.22 g/cm^3 (Figure 6.15). The LUT is designed for only oblate particles, since prolate particles are rare and can't be distinguished from this retrieval process. Previous research also found that oblate spheroids can represent the shape of ice aggregates better than prolate spheroids [18]. Each ZDR corresponding to a density and an AR is saved in the same matrix which is later used in retrieval. The two vectors containing all density and AR respectively are also saved. In Figure 5.4 right, a example of ZDR LUT is shown.

5.4.3. Iteration

For the first iteration, the AR spectra are initialized as 0.6 for all velocity bins, though other values within the range of LUT can also be used. Then volume V and density ρ are calculated based on D_{max}, AR and mass, assuming particles are homogeneous oblate spheroids:

$$V = (AR \times D_{max}/2)(D_{max}/2)^2 \times \frac{4\pi}{3} \tag{5.14}$$

$$\rho = m/V \tag{5.15}$$

By searching the indexes of ρ and corresponding observed sZDR in the LUT, the corresponding AR can be determined and updated. The input density is firstly checked to make sure it's within the density range of LUT. Then a corresponding ZDR value is looked up in LUT. The index of such ZDR value is used to find a corresponding AR as output. If the input ZDR is smaller than the smallest ZDR corresponding to input density in the LUT, AR equal to one is returned. If the input ZDR is larger than the largest ZDR corresponding to input density in the LUT, AR equal to zero is returned as a mark of such situation. Now the new AR is inputted and new ρ is calculated using the same procedure above. Since the AR returned can be zero, the calculated density can be infinity. In this case the returned AR in next iteration will set zero. The zero AR is used in retrieving number concentration of particles.

Usually it takes about four iterations for AR and density to fully converge. After that the results oscillate between neighboring values in LUT. The difference between two iterations of the sum of AR during the iteration process in one case is shown in Figure 5.5:

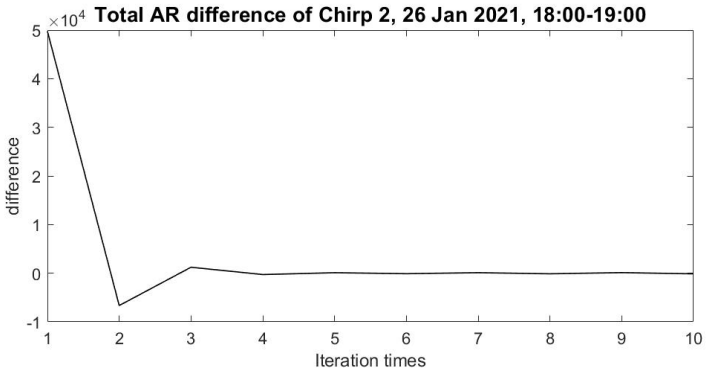

Figure 5.5: The total difference of AR during iterations for Chirp 2, 18:00-19:00 26 January 2021

In iterations, any intermediate density results which are out of the boundary of LUT are removed and won't participate in subsequent procedure.

5.5. Retrieval of Particle Number

This process is similar to the step 4 and 5 in [17]. To retrieve number concentration of particles (NOP) in velocity bins, spectral reflectivity sZ_{hh} at 35GHz is introduced. The parts of spectra with value smaller than noise level are removed. Gas attenuation correction for spectral reflectivity is similar to Section 5.2.2, but with one frequency the attenuated value should be added to the observed spectral reflectivity (Equation 5.16).

$$sZ_{hh35}(r) = sZ_{hh35,att}(r) + 2/sin(Elv)\int_0^h \alpha_{att,35,gases}(s)ds \tag{5.16}$$

A LUT is built for reflectivity similar to the LUT for ZDR. In the LUT, the controlling parameters are D_{max} and AR while the resulting matrix is radar reflectivity at 35GHz. The range of AR is the same as the LUT of ZDR, while the range of D_{max} is from 0.02mm to 3.4mm. The m(D) relation of Yang2000 is used during the simulation to build the LUT, unlike the LUT for ZDR. Since D_{max} and AR are already solved previously, the estimated $Z_{hh,est}$ (mm^6/m^3) of a single particle in a velocity bin can be looked up directly. To minimize the loss of valid velocity bins in this process, if the input D_{max} is smaller than the minimum D_{max} in LUT, the minimum D_{max} in the LUT will be used for searching corresponding reflectivity instead, since as D_{max} becomes smaller, the reflectivity decreases very slowly. If the input D_{max} doesn't have corresponding AR information, it is assumed that the AR equal to 0.6. The 0.6 is an average value of AR of aggregates [52]. If the AR is too small for the LUT (marked by AR equal to zero), the reflectivity of the particle with the same D_{max} and smallest AR in LUT is returned because reflectivity is only slightly affected by AR (Figure 4.6). With the estimated reflectivity of a single particle in velocity bins, one can estimate the number concentration of particles by:

$$NOP = Z_{hh,obs}/Z_{hh,est} \tag{5.17}$$

where $Z_{hh,obs}$ is the observed spectral reflectivity of a velocity bin and $Z_{hh,est}$ the estimated reflectivity of a particle in that velocity bin (mm^6/m^3). In this process, almost all the bins with valid sDWR and sZ_{hh35} can obtain NOP.

5.6. Calculation of Ice water content and Ice water path

Ice water content (IWC) profiles (g/m^3) can be retrieved using retrieved mass and NOP spectra:

$$IWC(r,t) = \sum NOP(r,t,v) \times m(r,t,v) \tag{5.18}$$

where r and t are range and time, v the Doppler velocity. Previously, empirical relations between temperature, radar reflectivity and IWC (Z-T-IWC relation) were summarized from several large airborne in-situ microphysical databases [66]. These databases include only cases of ice cloud. The relation

for radar reflectivity at 35GHz at mid-latitude was found to be [66]:

$$log_{10}(IWC) = 0.000372ZdB_{35}T + 0.0782ZdB_{35} - 0.0153T - 1.54 \tag{5.19}$$

where IWC is in the unit of g/m^3 and temperature in Celsius. This empirical relation serves as a comparable target for the retrieved IWC in this research.

Furthermore, ice water path (IWP,g/m^2) can be calculated based on IWC profiles:

$$IWP(t) = \sum IWC(r,t) \tag{5.20}$$

The IWP calculated in this study only includes IWC within radar range, and therefore it is not a typical IWP which takes the entire atmospheric column into account. Also, the IWP is not vertically integrated but in the direction of the radar beam.

5.7. Retrieval of Particle Size Distribution

In order to illustrate how to extract PSD in some cases, groups of particles can be extracted from LV1 reflectivity profiles at 35GHz using region growing algorithm, with a threshold to limit the spatial range of particles that involved. The starting point of region growing is chosen manually. The algorithm compares the reflectivity of current point with each one of its four neighbors. If their difference is less than the threshold, the neighbors are accepted into the extracted region. The comparison and acceptance of new points are repeated until all the neighbors of the region have difference larger than the threshold compared with the reflectivity of their accepted neighbors. The threshold is chosen manually by deciding if the desired region is extracted.

The extracted region is considered to contain the same population of particles. The algorithm can be successful when there is enough change of reflectivity at the edge of a region. Although usually it cannot extract a certain region due to the lack of change of reflectivity between different group of particles, the purpose of such extraction is only for testing the retrieval of PSD in some case. Hopefully the change of PSD of the same population of particles can be detected at different height.

The ice particle sizes are assumed to follow the normalized gamma distribution [20] with shape parameter $\mu = 0$ (an exponential PSD). $\mu = 0$ is a typical value for snow aggregates [18]. When $\mu = 0$, the PSD function N(D) ($mm^{-1}m^{-3}$) becomes:

$$N(D) = N_w e^{\frac{-3.67D}{D_0}} \tag{5.21}$$

where N_w is the intercept parameter ($mm^{-1}m^{-3}$), D_0 the median volume diameter (mm), D the melted-equivalent diameter of the ice particles (mm) [18]. In Equation 5.21, the variable in N(D) is D rather than D_{max}. When the particle mass was retrieved using Yang2000, D_v was once calculated (Equation 2.16,Section 5.3), but it was in centimeter. After the conversion of the unit from cm to mm, D_v becomes D. In this research, number concentration (NOP) of particles are presented in base-10 logarithmic scale, and thus a linear function of PSD in logarithm can be fitted to retrieved results:

$$log_{10}(N(D)) = -\frac{3.67D}{ln(10)D_0} + \frac{ln(N_w)}{ln(10)} \tag{5.22}$$

The N_w and D_0 can then be derived from the fitted parameters and Equation 5.22.

In practice, the 2D histogram of NOP versus D is obtained with a certain bin size. A straight line represented by Equation 5.22 is fitted to the 2D histogram. The bin size of D is different from 1mm, and thus a unit conversion is needed in order to keep the unit of log10(N(D)) as $log10(mm^{-1}m^{-3})$. A value should be added to the right side of the fitted Equation 5.22 for such conversion. For example, if the bin size of D is 0.02mm, the added value should be $log10(1/0.02)$.

The bin size of 2D histogram affects the fitted line, but such effect is not studied in this research. The number of bins of D and NOP in histogram are both set as 50 regardless of the range of them.

5.8. Estimating the maximum potential DPIA caused by liquid

To estimate the maximum potential DPIA caused by supercooled liquid, the cloud base is extracted from reflectivity profiles at 35GHz by searching for the lowest height-time bins with valid reflectivity measurements at each time step. To prevent extracting incorrect cloud base, sometimes noise below cloud base in the reflectivity profiles need to be removed manually.

By assuming that all the supercooled liquid concentrates at cloud base for all time steps, one can derive maximum possible DPIA caused by liquid using LWP from radar measurements. The attenuation coefficient per unit mass k_a (dBm^2kg^{-1}) is calculated as [24]:

$$k_a = 81.863 \times \frac{Im(-K)}{\lambda} \tag{5.23}$$

where λ is the radar wavelength (m) and K the Clausius-Mossotti factor defined in terms of the complex dielectric constant ϵ:

$$K = \frac{\epsilon - 1}{\epsilon + 2} \tag{5.24}$$

where ϵ for water is a function of temperature T for different frequency. The ϵ-T relation from [67] is exploited and the temperature at cloud base is obtained from microwave radiometer. Therefore, the DPIA assuming all liquid located at cloud base can be calculated by:

$$DPIA(t) = 2 \times LWP \times (k_{a,94} - k_{a,35})/sin(Elv) \tag{5.25}$$

When Westbrook2006 is employed to retrieve particle size (Figure 5.3), the DPIA(t) in this case will move the entire curve in Figure 5.3 upwards with a distance equal to DPIA(t), which means that for the same particle size the measured DWR becomes larger. Therefore, one can calculate the error of particle size caused by such movement of the curve for the entire range of DWR (0-8.5dB). In Figure 5.6, the effect of 0.4dB of DPIA on DWR-size relation is shown as an example. The blue curve is the original DWR-size relation (Westbrook2006) while the red curve is the DWR-size relation with DPIA equal to 0.4dB. The difference of retrieved D_{max} (the difference of red and blue curves) is shown in black.

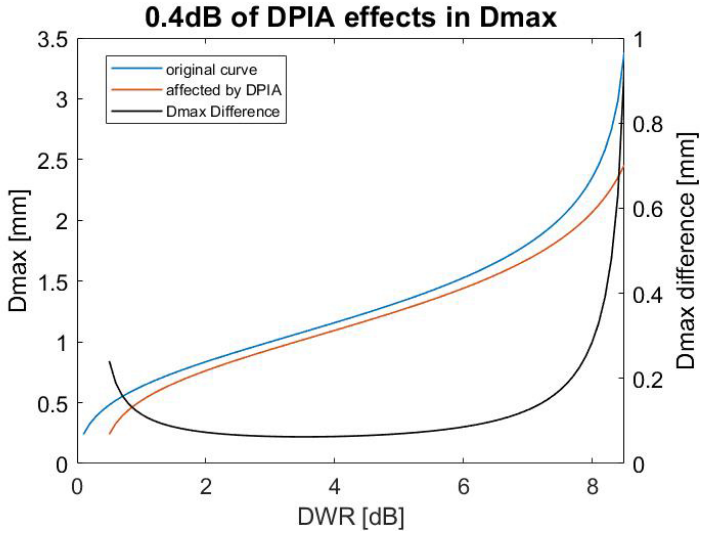

Figure 5.6: An example of the impact of DPIA on DWR-size relation (Westbrook2006 with r_g converted into D_{max}).

One can notice that due to the shape of the curve, the error of D_{max} is larger at the both ends of DWR range. The calculation of D_{max} difference in Figure 5.6 can be performed for all the time steps, and profiles of the error of D_{max} can be obtained. Furthermore, the error in particle size can be propagated into the error in mass using the m(D) relation of Yang2000 (Figure 5.7). In Figure 5.7, the original DWR-mass relation (Westbrook2006 together with Yang2000, blue curve) and the DPIA-affected relation (red curve) are shown. The difference between the two curves is shown in black.

Unlike DWR-size relation, the difference of mass is large only when the particle is large. The reason is that the mass increases nearly as the cube of the diameter (Yang2000) or, at least, nearly the square of the diameter (BF95 and Lerber17). Hence, for small diameter, the mass exhibits a gradual increase, while for large diameter, the mass experiences a more rapid growth as the diameter expands. This effect surpasses the impact of the large diameter difference for small particles (Figure 5.6), leading to a seemingly monotonic increase in mass difference as DWR increases (Figure 5.7).

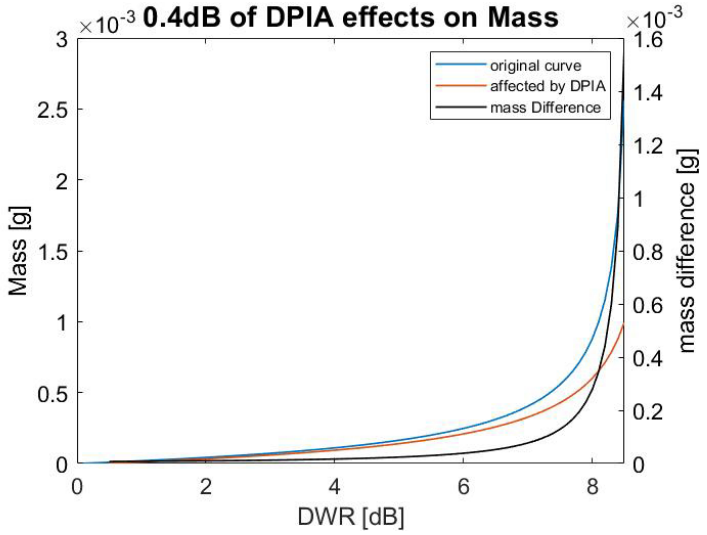

Figure 5.7: An example of the effect of DPIA on DWR-mass relation (Westbrook2006 together with Yang2000).

Similarly, profiles of the error of mass can also be obtained for all the time steps with DPIA(t).

5.9. Conclusion

The retrieval procedure of maximum dimension, aspect ratio, density, number concentration and IWC are described in detail in this chapter. Then retrieval of PSD from SR results is illustrated. The estimation of the DPIA from supercooled liquid is also introduced. The same procedure can be applied to height-time profiles of radar measurement (except the retrieval of PSD), which is called bulk retrieval as mentioned in Section 2.7. The impact of bulk retrieval will be discussed in the following section.

6

Results and Discussion

Two MPC events with retrieved results are studied and discussed below. Both events fulfill the requirement of low LWP (<100 g/m^2). The first event (Event A) is the test case of the retrieval process. It occurs from 18:00 to 19:00 on 26th January, 2021. Its DWR profiles are mostly within the range of 0 to 8.5dB while its ZDR profiles generally exhibit relatively low values, which is relatively ideal. The second event (Event B) occurs from 19:00 to 20:00 on the same day, with DWR profiles larger than 8.5 dB in some parts and regions of large ZDR.

For both events, the radar measurement profiles and LWP are shown. For the first event, spectral retrieval results including spectra and profiles of retrieved properties are shown. Comparison of IWC and IWP with the result from an empirical model are discussed and the reasons behind large retrieved IWP are studied. Particle size distribution for a certain region in the cloud is shown. Besides, in Section 6.1.2, the bulk retrieval results of the first event is exploited to compare the impacts of using different m(D) relations, while the differences between spectral and bulk retrieval results are discussed in Section 6.1.3, including IWP and NOP. Also, the maximum potential DPIA caused by liquid is shown in Section 6.1.4. For the second event (Section 6.2), the focus is on discussing the loss of valid velocity bins and subsequent effect on IWC and IWP. The reasons behind the loss are discussed (Section 6.2.2). The BR IWC is compared with SR IWC to see if it is better under this circumstance (Section 6.2.3).

6.1. Event A

The radar measurements profiles of event A are shown in Figure 6.2 to provide an overview of the event. As shown in Figure 6.2 (a) and (b), the whole cloud is well above freezing level (blue line), while the LWP measured by radiometer and radar are both above sensitivity level (Figure 6.1) but not more than $100g/m^2$. The cloud can be considered as an altostratus according to [68]. The convection at cloud top produces ice particles and they fall along clear fall streaks (Figure 6.2 (a) and (b)). The reflectivity profiles at 35GHz contain more points at cloud top and bottom than the profiles at 94GHz because the sensitivity of radar at 94GHz is lower. The blue stripe at about 1300m in Figure 6.2 (b) are caused by noise of the radar at 35GHz. From 18:20 to 18:40 and after 18:50, large particles are probably formed at the middle of the cloud (Figure 6.2 (c)). DWR can be negative when regions (from 18:00-18:10 at 3000m and parts at cloud top and bottom) with tiny particles are affected by noise. The regions where DWR$_{KaW}$ value is larger than 8-10dB have a high possibility of being riming regions [33].The larger the DWR$_{KaW}$ within a region, the higher the possibility of riming it has. Nevertheless, the composition of ice crystals within the aggregates also influences (s)DWR. In Figure 6.2 (d), some non-spherical particles can be seen from 18:00 to 18:20 with ZDR up to 0.5dB. Compared with the cases (a) and (d) in [22], the ZDR in the profiles later than 18:20 is probably small enough to ignore the effect of the elevation angle of radar on DWR, but it can't rule out some large sZDR. However, before 18:20 the DWR should be larger than the value hypothetically measured by a vertically-pointing radar due to such effect.

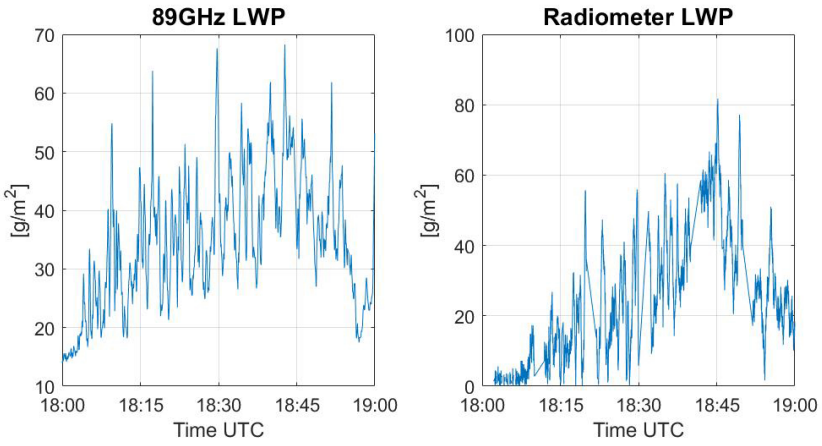

Figure 6.1: LWP measurements of Event A. Left: LWP measured by the receiver on 94GHz radar (with same pointing direction as the radar beam). Right: LWP measured by the vertically-pointing radiometer.

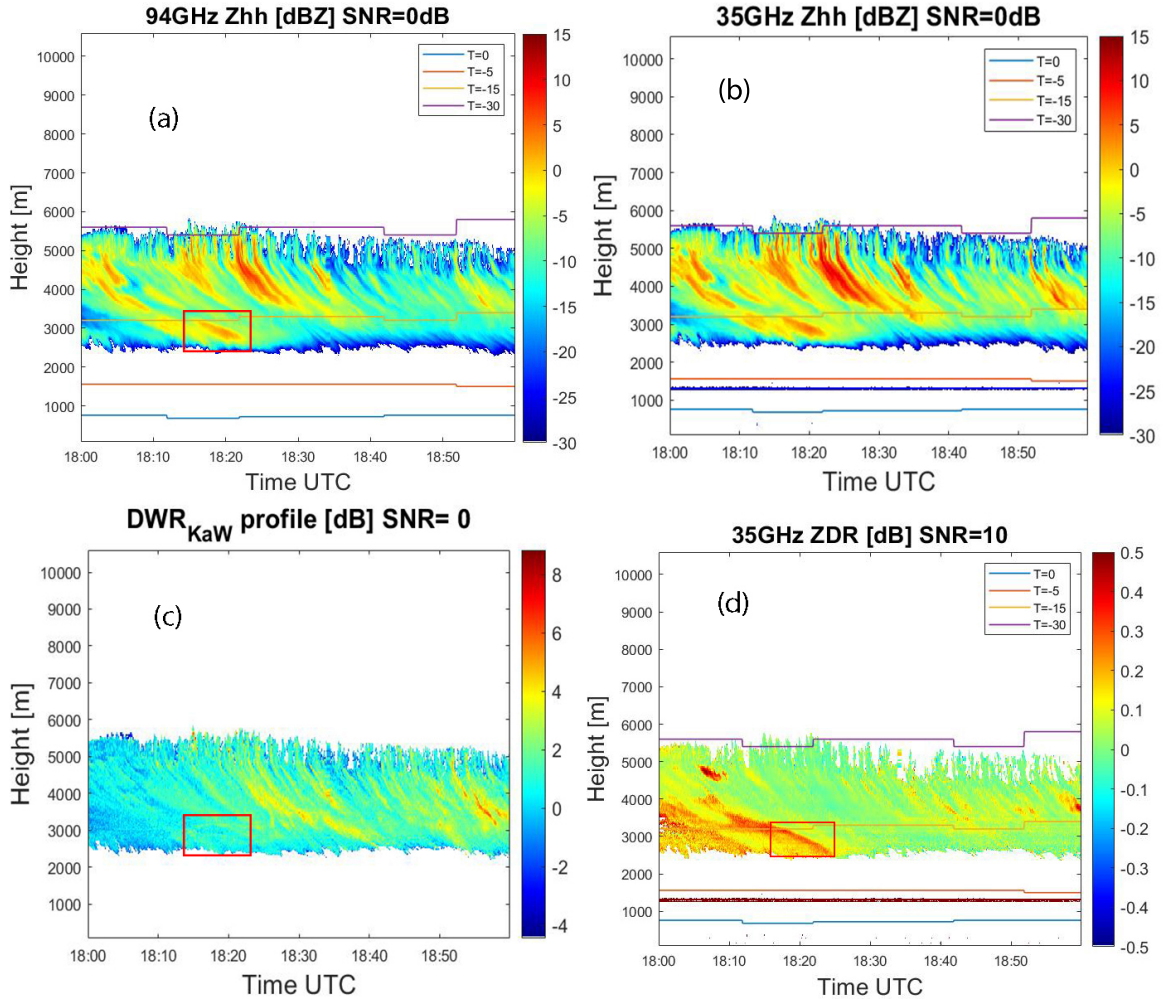

Figure 6.2: Radar measurement profiles with gas attenuation correction and ZDR calibration of Event A: (a) Reflectivity at 94GHz (b) Reflectivity at 35GHz (c) Dual-wavelength ratio (d) Differential reflectivity at 35GHz. The curves in (a) (b) and (d) represent the temperature. The regions within a red box are for discussion.

In Figure 6.2, at 3000m at around 18:20, a group of ice particles (red box) exhibits high reflectivity at both 35GHz and 94GHz, but the DWR profiles indicate that their size is not large. Therefore the

concentration of particles is expected to be high. The ZDR in the same region is large compared to other region, and thus relatively small AR is expect. Since the ZDR profiles (Figure 6.2 (d)) were applied to a noise level removal of 10dB, the velocity bins that involve in profiles' calculation are less than the other three profiles.

6.1.1. Spectral Retrieval Results

The assumption that each velocity bin contains one type of particles in spectral retrieval allows detailed description of the population of particles, which is expected to provide better results than bulk retrieval considering that its assumption is less realistic. Additionally, spectral retrieval enables the acquisition of particle size distribution.

6.1.1.1 Resulting spectra

An example of resulting spectrograms from spectral retrieval are given below. In Figure 6.3 and Figure 6.4, input Doppler spectra of sDWR, sZDR and sZ_{hh35} are shown along with resulting spectra of D_{max}, AR and number concentration of particles at 18:29:32. sDWR and sZhh are corrected for gas attenuation, while the sZDR is calibrated as mentioned in Section 5.4.1. The resulting spectra lose some valid velocity bins during the retrieval process.

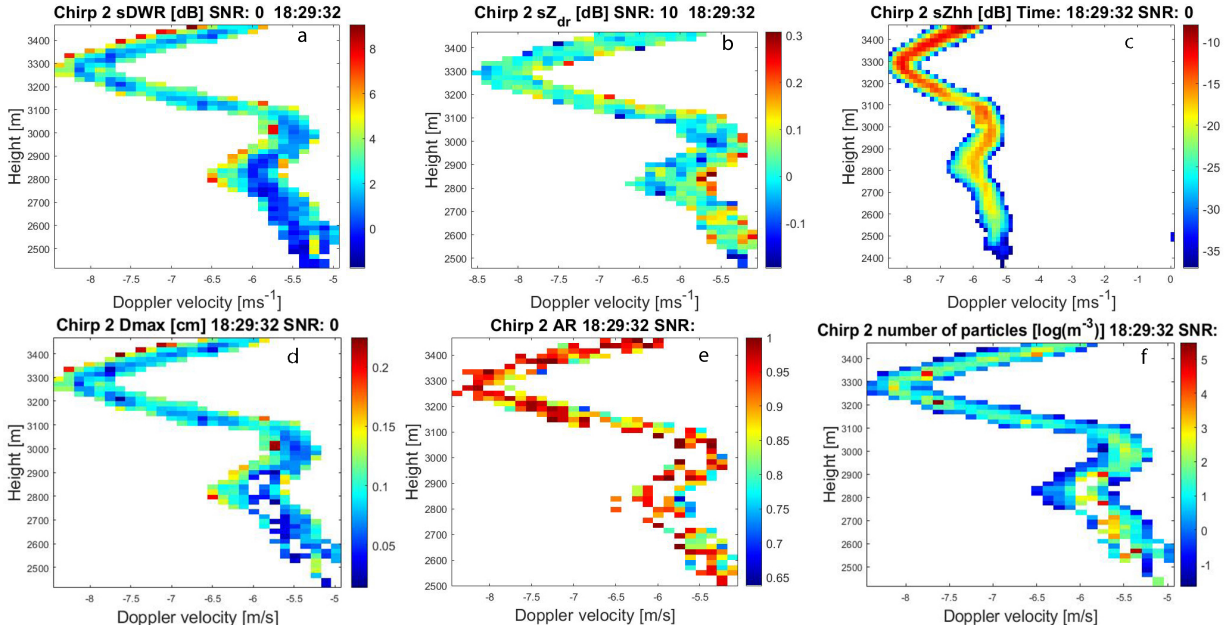

Figure 6.3: Chirp 2 spectra: (a) sDWR (b) sZ_{dr} (c) sZ_{hh35} (d) D_{max} (e) AR (f) NOP of 18:29:32 on 26 January 2021 (Event A)

The blank velocity bins in D_{max} and NOP of Chirp 2 (Figure 6.3 (d) (f)) are caused by negative DWR after $DPIA_{gases}$ correction, while the extra blank bins in the spectra of AR (figure (e)) come from higher noise removal level (SNR=10dB) and ZDR calibration because negative sZ_{dr} are removed. Bins with large sZ_{dr} have small AR, which is reasonable. In Figure 6.3 (d), large particles can be seen at the left side of the spectra with large absolute Doppler velocity, which is consistent with the fact that large particles usually fall faster. In Figure 6.3 (e), particles with small AR appear at the right side of the spectra, which is consistent with the fact that small particles tend to be more non-spherical.

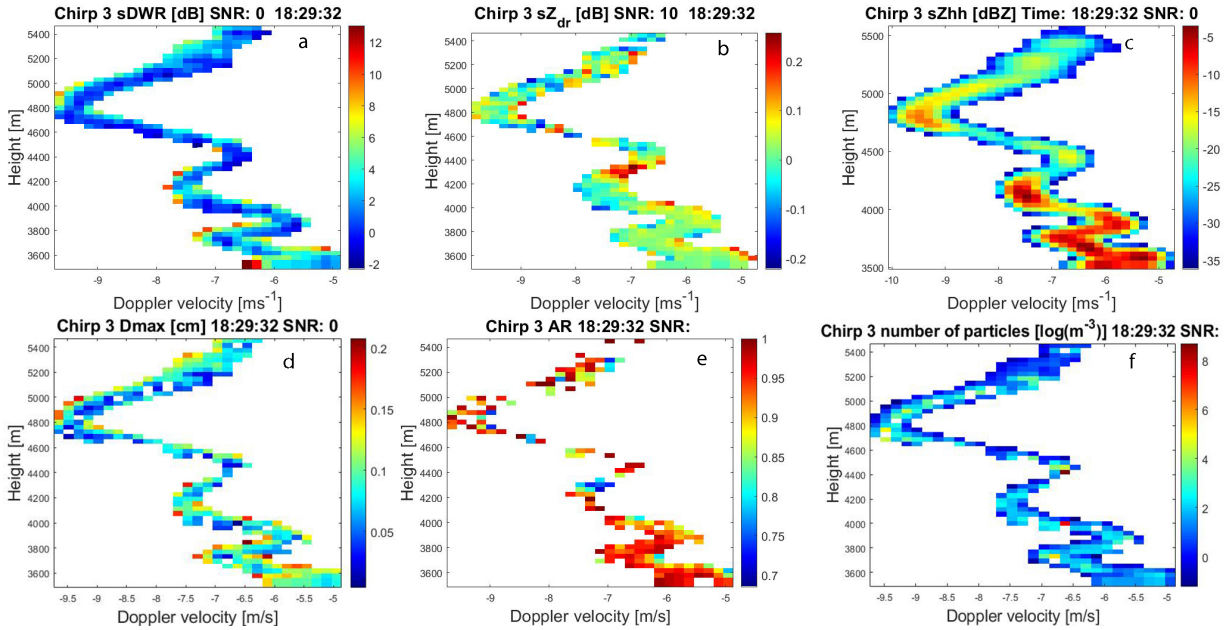

Figure 6.4: Chirp 3 spectra: (a) sDWR (b) sZ_{dr} (c) sZ_{hh35} (d) D_{max} (e) AR (f) NOP of 18:29:32 on 26 January 2021 (Event A)

In Figure 6.4 (e), the spectra of AR lost quite some bins compared with sZ_{dr} in (b). In both Chirp 2 and Chirp 3, AR spectra has less valid bins than NOP and D_{max}. To determine how the number of valid bins changes during retrieval process, the remaining valid bins after each steps are counted. The statistics are shown in Section D.

6.1.1.2 Particle Size Distribution

A group of particles is extracted from the reflectivity profiles at 35GHz of Event A using the approach described in Section 5.7. The reflectivity profiles at 35GHz of the extracted region are shown in Figure 6.5 left, while NOP of the region is shown in the right. The inset within the left figure indicates the position of the region within the entire profiles. In the left figure, the reflectivity profiles indicate that two populations of particles next to each other are extracted. The earlier one ranges from about 5300m to 3800m and the later one ranges from about 4900m to 3600m. In the right figure, it is shown that the number concentration of ice particles is larger at higher altitude.

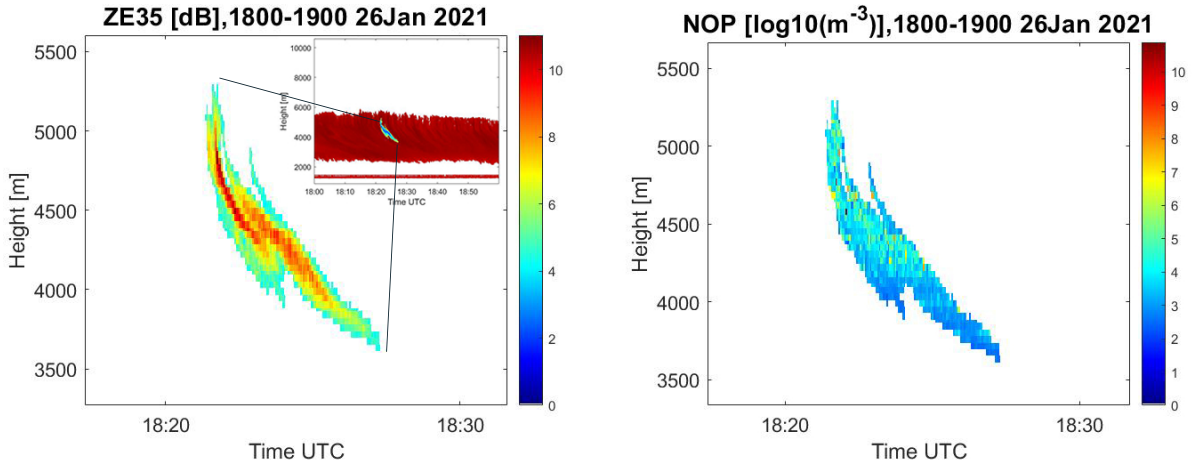

Figure 6.5: Left: The reflectivity profile at 35GHz of the extracted region. Right: The number concentration of the extracted region.

In Figure 6.6 left, the average SR D_{max} is shown. Overall, the size of ice particles is increasing while

falling. SRIWC shown in Figure 6.6 right exhibits some consistency with the NOP profiles in Figure 6.5 right, which is consistent with a finding in Section 6.1.2: NOP variation plays a bigger role in IWC than mass variation. The retrieved SRIWC is smaller at lower altitude.

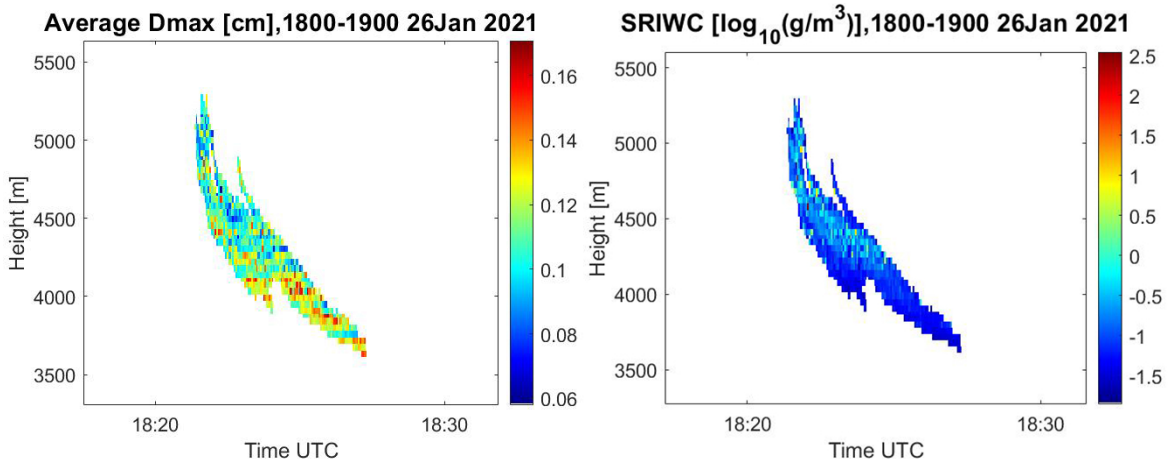

Figure 6.6: Left: Average (SR) D_{max} of the extracted region. Right: SRIWC of the extracted region.

In Figure 6.7, the 2D histograms of the retrieved spectral equi-volume diameter versus spectral NOP are shown with different height range (3500-5300m) for the extracted region in Figure 6.5. The log10(N(D)) fitted to the 2D histogram (green lines) and the log10(N(D)) after unit conversion (red lines) are shown for each height range. The increasing D_0 and the decreasing N_w as height decreases indicate that small particles with high concentration become larger particles with low concentration as they fall. The aggregation is expected to play a major role during this process. Such trend reverses slightly from 4500m to 4000m, probably because the inclusion of a new population of particles with high concentration and small size (Figure 6.5 left). A phenomenon that supports this claim is that in Figure 6.7 (d), two different N(D) can be observed vaguely in the points of histogram. But the spread of points can be observed as early as in figure (b), which corresponds to the starting height of the new population of particles (Figure 6.5 left).

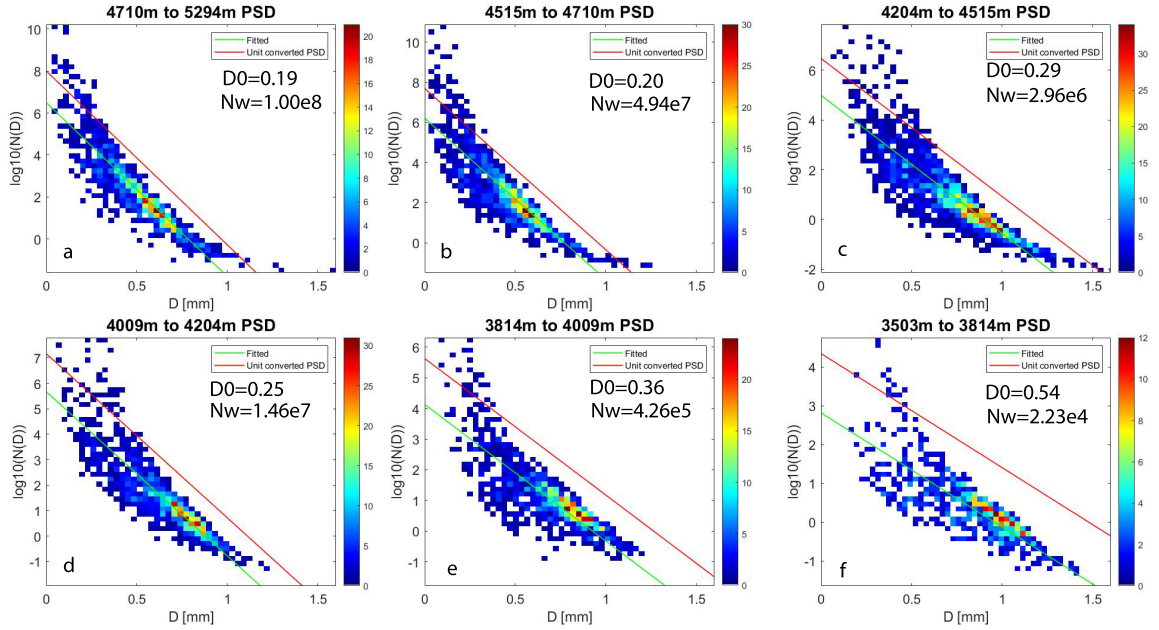

Figure 6.7: The 2D histograms of the retrieved spectral equi-volume diameter versus spectral NOP of height range: (a)4700-5300m, (b)4500-4700m, (c)4200-4500m, (d)4000-4200m, (e)3800-4000m, (f)3500-3800m. The green lines are the log10(N(D)) fitted to the histogram with unit dependent on the size of diameter bin. The red lines are the log10(N(D)) with the unit of $\text{mm}^{-1}\text{m}^{-3}$. The median volume diameter D_0 and the intercept parameter N_w are shown for each N(D) (red lines).

The fitted log10(N(D)) for every 200m is shown in Figure 6.8 left from 3500-4900m, while the derived D_0 and log10(N_w) for every 200m are shown in Figure 6.8 right. Figure 6.8 confirms the conclusion which was obtained from Figure 6.7: As the population of particles falls, the number concentration decreases but the size of particles increases.

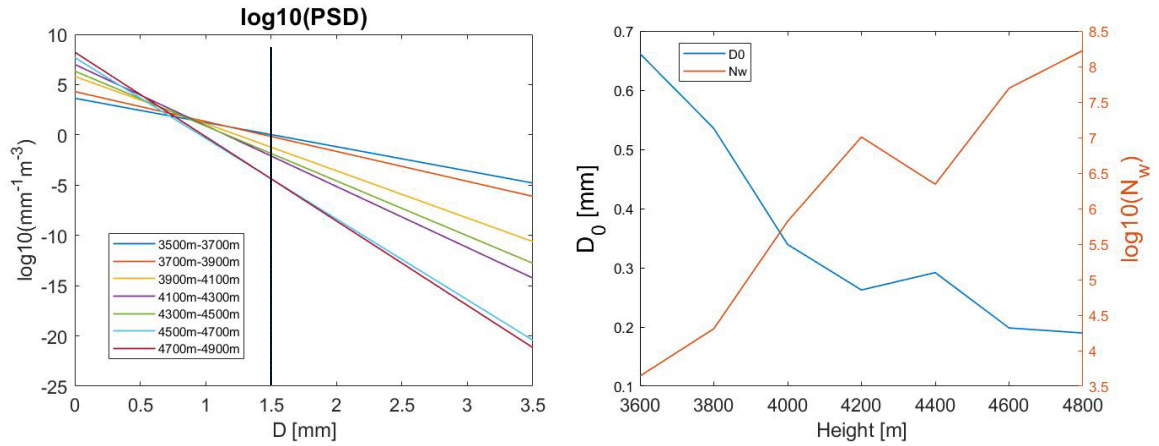

Figure 6.8: Left: Fitted log10(N(D)) ($\text{mm}^{-1}\text{m}^{-3}$) for different height range. The black vertical line represents the upper limit of D that involve in the fitting. Right: The D_0 and log10(N_w) for different height. The values in x axis are the midpoints of the height ranges.

6.1.1.3 Resulting profiles

The retrieved spectra of maximum dimension, aspect ratio, density and number concentration of particles can be used to produce height-time profiles. For D_{max}, AR and density, the equal-weighted average of values in each resulting spectrum are calculated to create height-time profiles (Figure 6.9 (a)(c)(d)). The number of particles (NOP, m^{-3}) of all velocity bins are summed up in each spectrum before taking logarithm with a base of 10 (Figure 6.9 (b)). The profiles of average mass are not shown

because mass is directly linked to size and therefore they have very similar profiles.

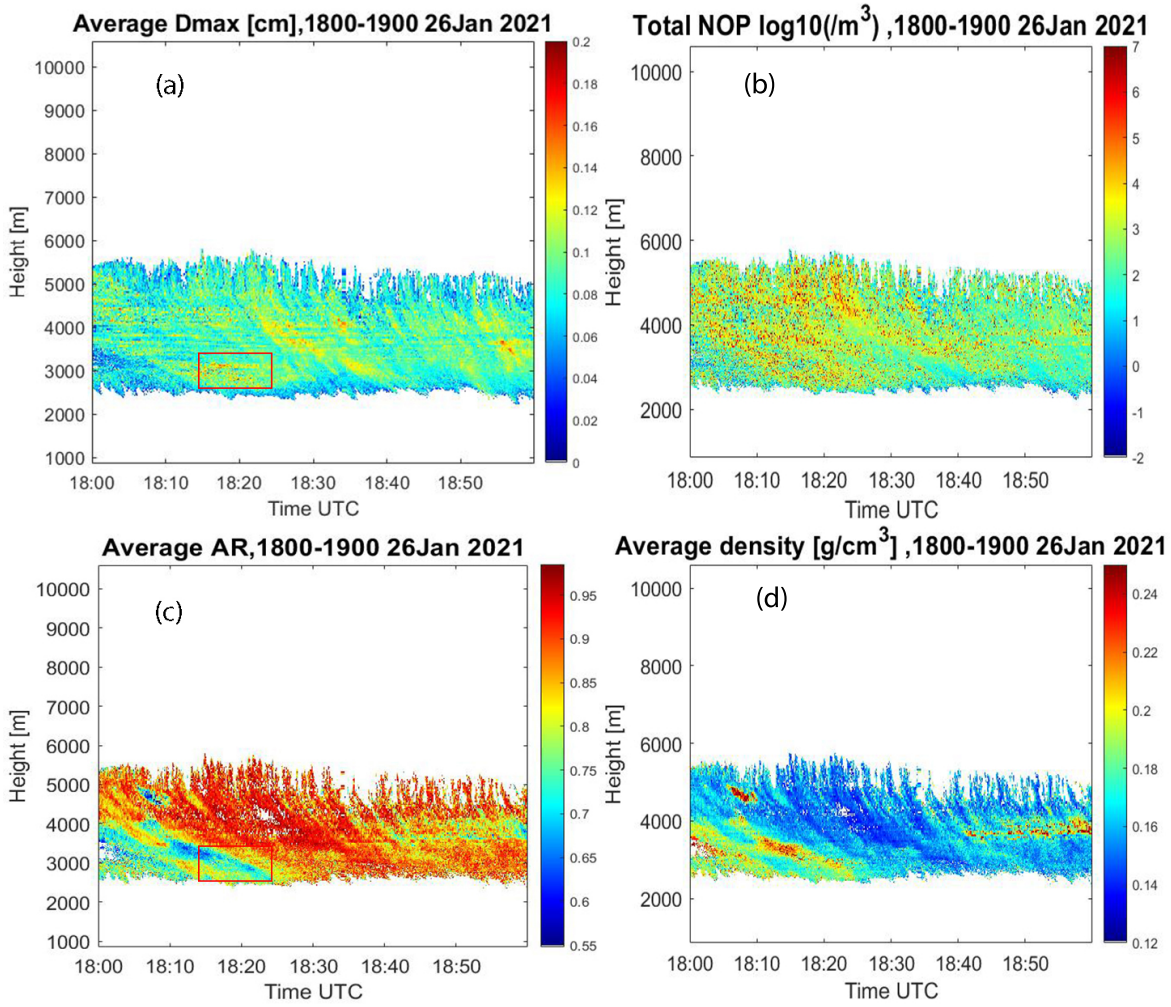

Figure 6.9: Resulting profiles of Event A: (a) Average maximum dimension (b) Total number concentration of particles (c) Average aspect ratio (d) Average density. The regions in red boxes are for discussion.

Figure 6.9 (a) shows reasonable correlation with DWR profiles in Figure 6.2 (c), though D_{max} profiles are more noisy. The dissimilarities arise from the removal of certain velocity bins and the fact that the average D_{max} is calculated using spectra of D_{max}, in contrast to the calculation of DWR using sDWR. The average AR in Figure 6.9 (c) has good correlation with ZDR profiles in Figure 6.2 (d), which agrees with the fact that higher ZDR indicates more non-spherical shape. The average density shown in Figure 6.9 (d) is larger at the regions with smaller AR. In Figure 6.9 (b), the profiles of NOP seem to be the noisiest. The reason behind this is not clear. It could be the introduction of spectral reflectivity at 35GHz. The sDWR that D_{max} profiles are based on is a difference of two spectral reflectivities and some common variation might be removed, while for sZDR a higher noise removal level (10dB) was applied, which could result in less noisy profiles of AR and density. Another possibility is the difference in calculation of the profiles, since only NOP profiles are a summation of resulting spectra. The region within the red box has low AR and high NOP as expected from observed profiles in Figure 6.2.

It is worth mentioning that Figure 6.9 (a) exhibits some horizontal stripes which don't exist in Figure 6.2 (a) (b). The underlying problem is brought by wind shear which affects the width of spectra (above noise level). The issue arises when the retrieval is conducted at the spectral level and the resulting profiles are calculated by taking the average, because height-time profiles of radar observable are not computed using the average of spectral observables as resulting spectra. In order to clarify the effect of wind shear in the width of spectra, the absolute value of the gradient of the mean Doppler ve-

locity (35GHz) in range direction is calculated and shown in Figure 6.10 left, while the width of spectra (WOS) at 35GHz is shown in Figure 6.10 right. The width of spectra is defined as the range of Doppler velocity of a spectrum where spectral reflectivity is larger than the noise level.

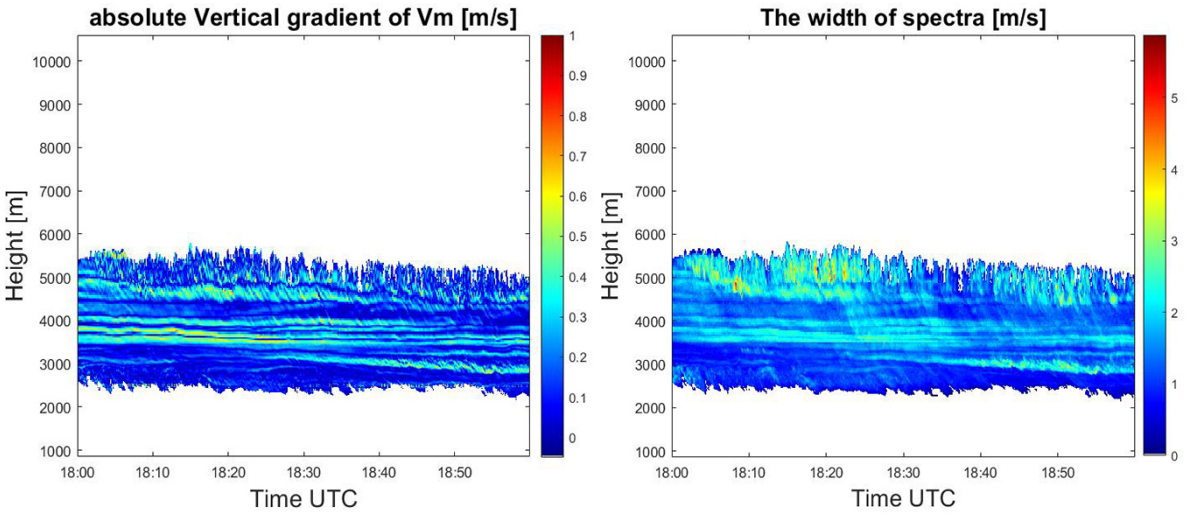

Figure 6.10: Absolute vertical (range) gradient of mean Doppler velocity (left) and the width of spectra (right) of Event A.

The stripes in both figures in Figure 6.10 have the same locations as the stripes in Figure 6.9 (a). By comparing the two figures in Figure 6.10, one can conclude that the width of spectra is large where the velocity gradient is large. Besides, some patterns of fall streaks can be seen in WOS. The large WOS near cloud top at around 18:00 and 18:20 are probably due to strong turbulence whose motion is perpendicular to radar beam and therefore doesn't exhibit in vertical gradient. The chance that it's caused by the presence of large particles is small because the location is at the cloud top.

Figure 6.10 also indicates that deriving terminal velocity from spectra is not feasible, though it can potentially be very useful information in determining riming events. The reason is that there's no way to quantify the spectral broadening due to wind shear reliably in this cases. Additionally, there is a lack of accurate horizontal wind profiles with high temporal resolution.

6.1.1.4 A first analysis of IWC and IWP

Ice water content (IWC) profiles are derived using retrieved mass and NOP spectra, as described in Section 5.6. The IWC derived from the empirical relation (Equation 5.19) is also employed for comparison. Both profiles are shown below (Figure 6.11):

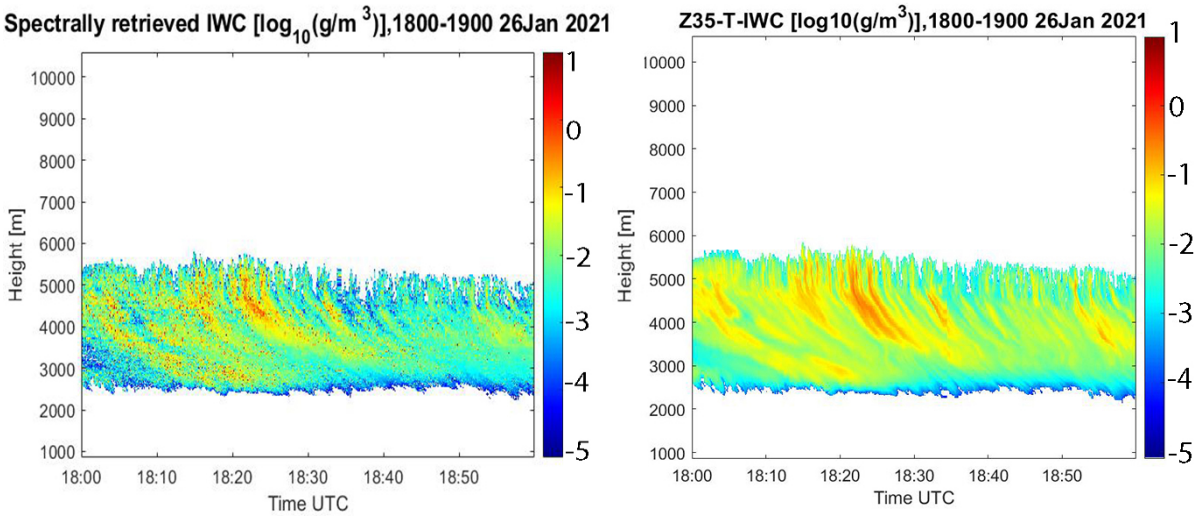

Figure 6.11: SR IWC (left) and empirical IWC (right) of Event A.

Spectral retrieved IWC profiles (SRIWC) (Figure 6.11 left) are much noisier than empirical IWC profiles (Figure 6.11 right) and with less successfully retrieved height-time bins due to the removal of data in retrieval process. This mainly happens at cloud top and bottom because of the low sensitivity of radar at 94GHz. Also, the SRIWC has smaller values at cloud bottom and top. Overall, the mean of SRIWC is smaller than empirical IWC, which is confirmed in the histogram of differential IWC in Figure 6.12 left. The difference is computed as:

$$log_{10}(SRIWC) - log_{10}(IWC_{em}) \tag{6.1}$$

Considerable number of bins exhibit larger SRIWC than empirical IWC despite a negative mean of the difference. In Figure 6.12 right, the relative error is computed as:

$$(SRIWC - IWC_{em})/IWC_{em} \tag{6.2}$$

The number of bins with negative and positive relative error are shown in the right figure.

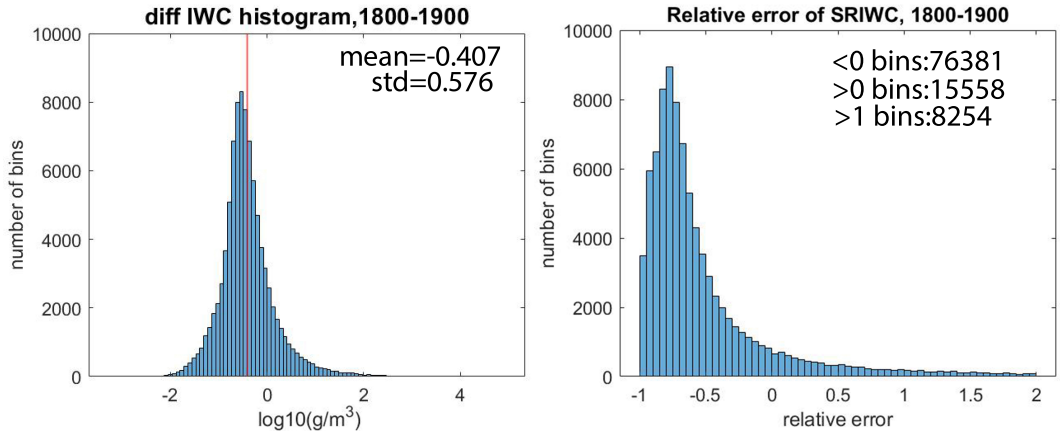

Figure 6.12: Left: Histogram of IWC difference in dB between SR IWC profiles and empirical IWC profiles. The red line represents the mean of the difference. Right: Histogram of relative error between SRIWC and empirical IWC of Event A

Figure 6.12 right confirms the conclusion reached from the left figure. Small amount of bins exhibit extremely large SRIWC. Ice water path (IWP,g/m^2) for SRIWC and empirical IWC profiles are calculated as described in Section 5.6 and shown in Figure 6.13. In Figure 6.13 left, original IWP of SRIWC

is shown while both IWP are compared in Figure 6.13 right. The SR IWP in the right figure (orange curve) is smoothed using moving average with window size of 36 seconds.

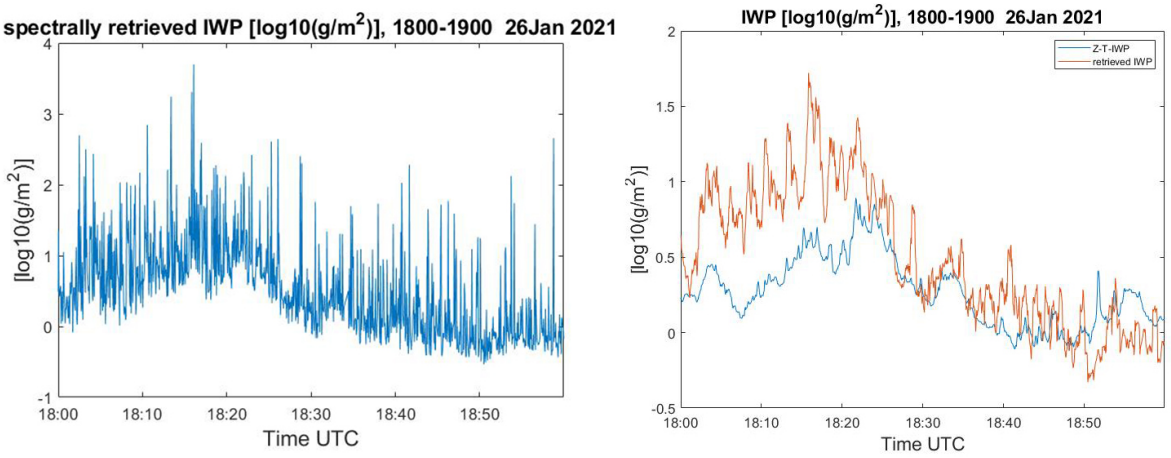

Figure 6.13: IWP of Event A. Left: Spetrally retrieved IWP. Right: Comparison of Z-T-IWP and smoothed retrieved IWP (moving average of 36 seconds).

The original spectral retrieved IWP (SRIWP) is very noisy (Figure 6.13 left) due to the noise in SRIWC profiles. Many obvious outliers are much larger, instead of smaller, than the smoothed IWP, which is consistent with the phenomenon in Figure 6.12 right. The SRIWP increases since 18:00 and reaches peak at about 18:17. Then it gradually decreases and remains at a low level. In Figure 6.13 right, The empirical IWP (blue curve) is smaller than SRIWP (orange curve) during 18:00 to 18:20 and larger for most of the time from 18:50 to 19:00. Two IWP are similar to each other from 18:20 to 18:45. The reasons behind their difference can be complicated. One noteworthy phenomenon related to this difference is the existence of large sZDR during 18:00 to 18:20 (Figure 6.14). Total sZDR is calculated by summing up all valid sZDR (dB) at each time step. The decrease of total sZDR (orange curve) and differential IWP (blue curve) happens simultaneously at around 18:25 (Figure 6.14). The connection between them remains unclear, but it is possibly related to the viewing geometry of radar [22].

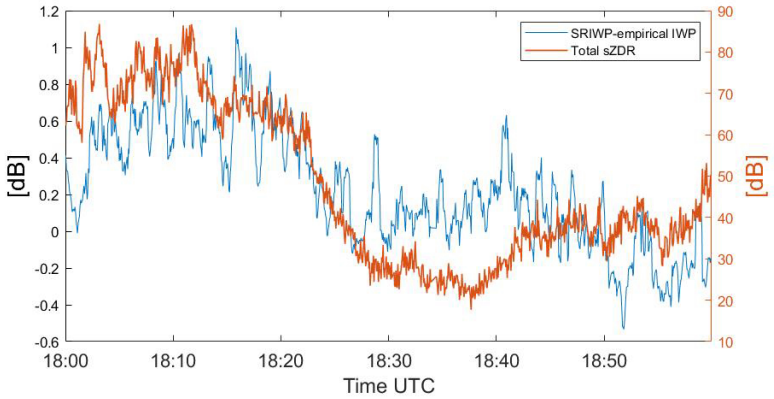

Figure 6.14: The total sZDR at every time step (orange curve) and the difference between SRIWP and empirical IWP (blue curve) in logarithm.

The Figure 6.11, Figure 6.12 and Figure 6.13 together reveal something more. One would expect that SRIWP is generally smaller than empirical IWP from Figure 6.11. However Figure 6.13 is out of such expectation. From Figure 6.12 one might conclude that the noisy points in SRIWC profiles with large values (Figure 6.11 left) could have significant impact on SRIWP (Figure 6.13).

6.1.2. More analysis of m(D) using bulk retrieved results

The bulk retrieval is based on the assumption that each radar volume contains a number of identical ice particles, which is more difficult to fulfill than in the case of spectral data. To assess the impact of different mass-size relations in the retrieval process, the retrieved results using three m(D) relations are compared using Event A. The m(D) involved in comparison are introduced in Section 2.6. Bulk retrieved profiles are used for the comparison of m(D) relations since they're directly calculated from integrated radar measurements and won't be affected by the process of averaging or summing up result spectra with eventually missing data.

The mass-size relations compared are modified BF95 [52] (Equation 2.15), Yang2000 [21] (Equation 2.16) and Lerber17 [47] (Equation 2.19). To provide a intuitive view of three relations, the density versus D_{max} of a spheroid with AR equal to 0.6 is plotted in Figure 6.15:

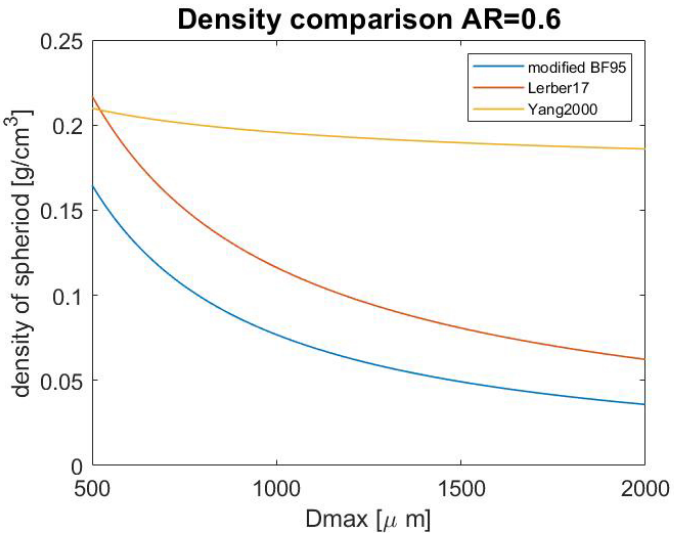

Figure 6.15: The density of a spheroid versus D_{max} with AR equal to 0.6 for Lerber17 (red curve), Yang2000 (yellow curve) and modified BF95 (blue curve).

Figure 6.15 shows that Yang2000 exhibits near constant density with value larger for most size range than the other two relations. Both are power-law relations, and Lerber17 provides larger value than modified BF95, because the former is derived from slight-rime condition.

The BR profiles of particle density, mass, number concentration and AR using different m(D) functions are shown in Figure 6.16, Figure 6.17, Figure 6.18 and Figure 6.19, respectively.

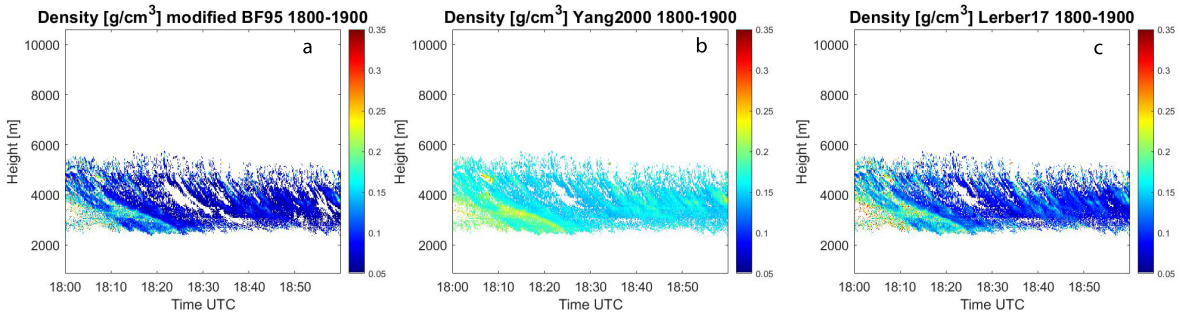

Figure 6.16: Density profiles from bulk retrieval using m(D) of : (a) modified BF95, (b) Yang2000 and (c) Lerber17.

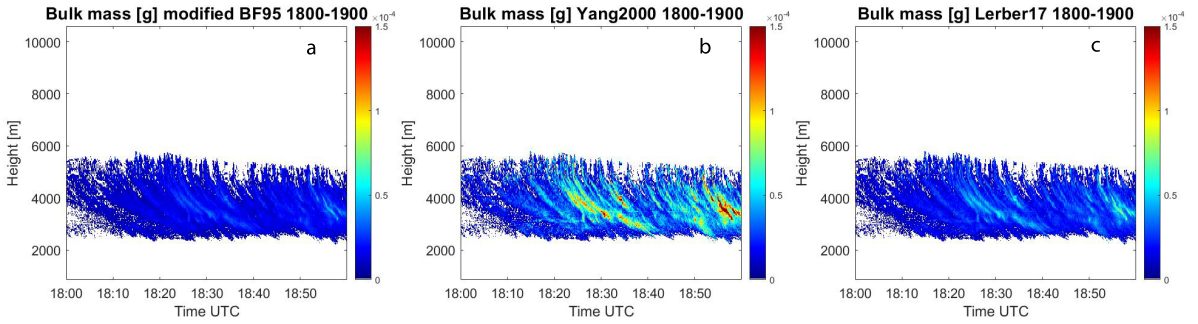

Figure 6.17: Mass profiles from bulk retrieval using m(D) of : (a) modified BF95, (b) Yang2000 and (c) Lerber17.

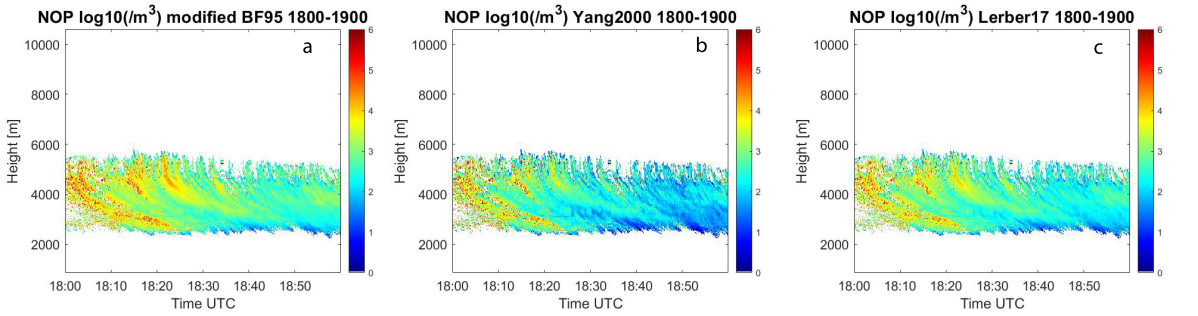

Figure 6.18: Profiles of NOP from bulk retrieval using m(D) of : (a) modified BF95, (b) Yang2000 and (c) Lerber17.

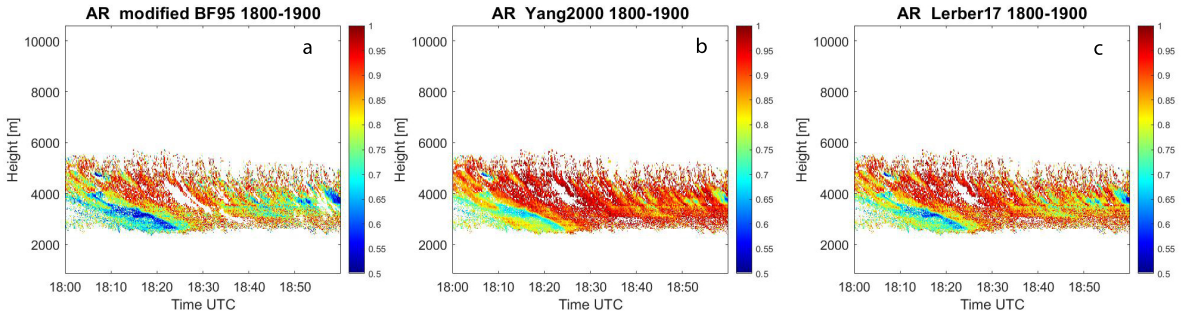

Figure 6.19: AR profiles from bulk retrieval using m(D) of : (a) modified BF95, (b) Yang2000 and (c) Lerber17.

In Figure 6.16, the density retrieved using Yang2000 is overall larger than the other two m(D), which is expected from Figure 6.15. The Lerber17 (Figure 6.16 (c)) provide density slightly higher than modified BF95 (Figure 6.16 (a)). Consequently, AR profiles of Yang2000 (Figure 6.19 (b)) are overall larger than the other two, since for a given ZDR, a particle with higher density should have a more spherical shape (Figure 5.4 right). The AR profiles of modified BF95 (Figure 6.19 (a)) therefore exhibit the lowest AR. The mass profiles of Yang2000 shown in Figure 6.17 (b) are significantly larger than the others due to higher density. The enhancement of mass is stronger for larger particles because of what is shown in Figure 6.15. For the NOP profiles, it is known that the radar reflectivity is mainly dependent on the size of particles and slightly dependent on AR except their concentration. It has been shown that the dependence of radar reflectivity on mass (density) is significant (Figure 4.7). For a given radar reflectivity, less number concentration of particles is needed when the density of particles are larger.

The density (Figure 6.16) and AR (Figure 6.19) profiles of different m(D) obviously contain different number of points. In both figures, the profiles of modified BF95 contain least points. As mentioned in Section 2.6.1, the modified BF95 results in more extreme values of retrieved AR and density when used with T-matrix. In this case, it can sometimes lead to overshooting the limits of ZDR LUT during

iteration in the retrieval process, and therefore less valid points are left in the profiles. Increasing the range of density in ZDR LUT can mitigate the loss of points especially for BF95, but it means more unrealistic results are kept in the profiles. The limits of density in ZDR LUT ($0.05 g/cm^3$ to $0.6 g/cm^3$) already encompasses density much larger than the possible density of an ice aggregate (Figure 6.15), which keeps the density that violate the presumption of Rayleigh-Gans theory. The lower limit ($0.05 g/cm^3$) also covers most of aggregate cases. Thus it is not necessary to increase the range of ZDR LUT in order to keep unrealistic results. Besides, the loss of points doesn't affect the purpose of comparing the effect of different m(D) in retrieval.

With BR NOP and mass, the BR IWC profiles are computed and shown in Figure 6.20. The IWC profiles are quite similar to each other, despite the evident differences in other profiles caused by different m(D). Combining Figure 6.17 and Figure 6.18, one can find out that the regions with larger NOP compared with other NOP profiles tend to have a smaller BR mass compared with other BR mass profiles. It is the radar reflectivity that provides such a constrain on IWC (Equation 2.3). Thus the IWC for a certain region can remain similar. However, one can still notice that BRIWC of Yang2000 is smaller than the other two. Considering Figure 6.17 and Figure 6.18, the smaller BRIWC of Yang2000 should result from the much smaller BR NOP of Yang2000.

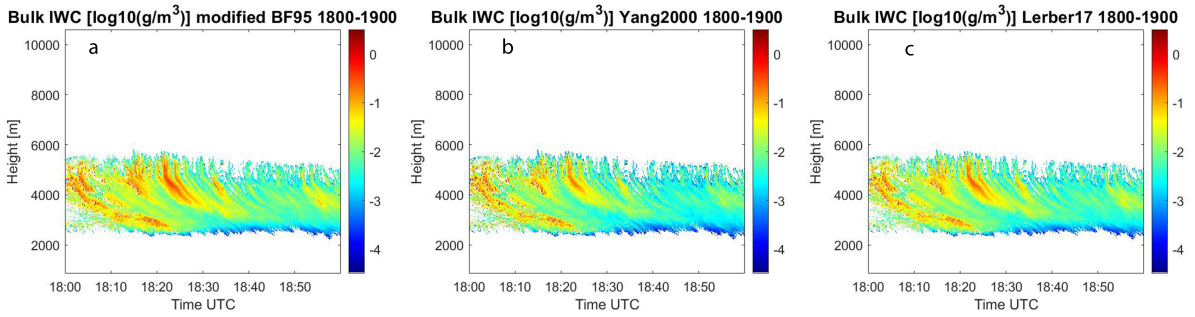

Figure 6.20: IWC profiles from bulk retrieval using m(D) of : (a) modified BF95, (b) Yang2000 and (c) Lerber17.

The relative difference between BR IWC retrieved using three m(D) relations and the IWC retrieved using the empirical relation are calculated and shown in Figure 6.21. In this case, the relative difference is computed as

$$(BRIWC - IWC_{em})/BRIWC \tag{6.3}$$

with linear value of IWC (g/m^3). The denominators are chosen to be different BRIWC instead of the empirical IWC because it leads to a larger range of relative difference, which is much better for visualization in this case. Overall, the IWC using modified BF95 (Figure 6.21 (a)) is closest to empirical IWC while the IWC using Yang2000 (Figure 6.21 (b)) tends to be much smaller than empirical IWC in later that hour. In the cloud regions with large ZDR in early hour (Figure 6.2), three BRIWC profiles exhibit larger value than empirical IWC. The spatial correlation between larger IWC and ZDR (AR) profiles indicates that the large IWC in these regions are connected to their large ZDR.

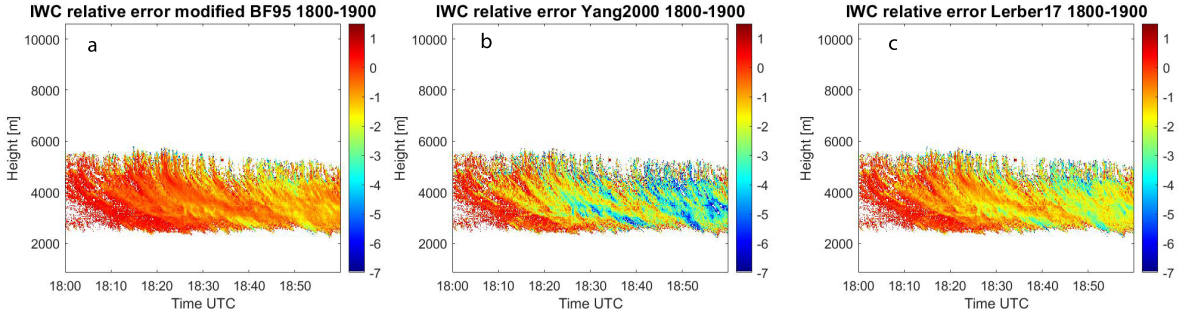

Figure 6.21: relative error of IWC profiles between empirical model and bulk retrieval with m(D) of : (a) modified BF95, (b) Yang2000 and (c) Lerber17.

The histograms of the relative difference of BR and empirical IWC (Equation 6.3) are shown in Figure 6.22 but with the empirical IWC as the denominator. The total number of bins in each of the three profiles is 82342, while the number of bins with negative relative error is included in each figure. Overall, the BR IWC with different m(D) are all prone to be smaller than empirical IWC regardless of m(D), but considerable amount of bins also exhibit positive difference.

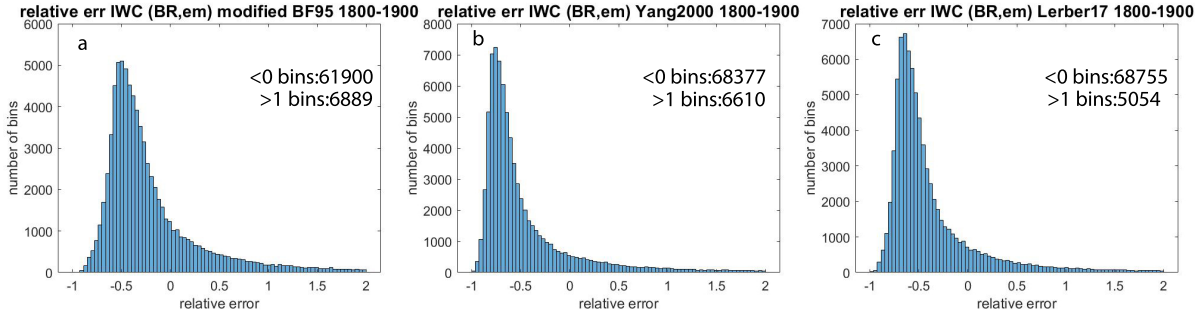

Figure 6.22: Histograms of relative error of IWC between empirical model and bulk retrieval with m(D) of : (a) modified BF95, (b) Yang2000 and (c) Lerber17.

The 2D histograms of relative error versus empirical IWC corresponding to three scenarios in Figure 6.22 are shown in Figure 6.23. Compared to the figures in the second row, figures in the first row indicate that BRIWC tend to be large than empirical IWC when IWC is small. The error of the smallest BRIWC can be extremely large. BRIWC of Lerber17 (figure (c)) exhibits positive error in a relatively smaller range of IWC_{em} (0-0.08 g/m^3). The figures in the second row indicate a predominance of large negative relative errors (below -0.9) and the distribution of negative error is clearly different for three m(D). The range of IWC_{em} where most bins concentrate is from about 0.15-0.25 g/m^3 for modified BF95, 0.06-0.15 g/m^3 for Yang2000 and 0.1-0.2 g/m^3 for Lerber17. Overall, large negative error exists at a wide range of empirical IWC. BRIWC of modified BF95 exhibits least bins with negative error.

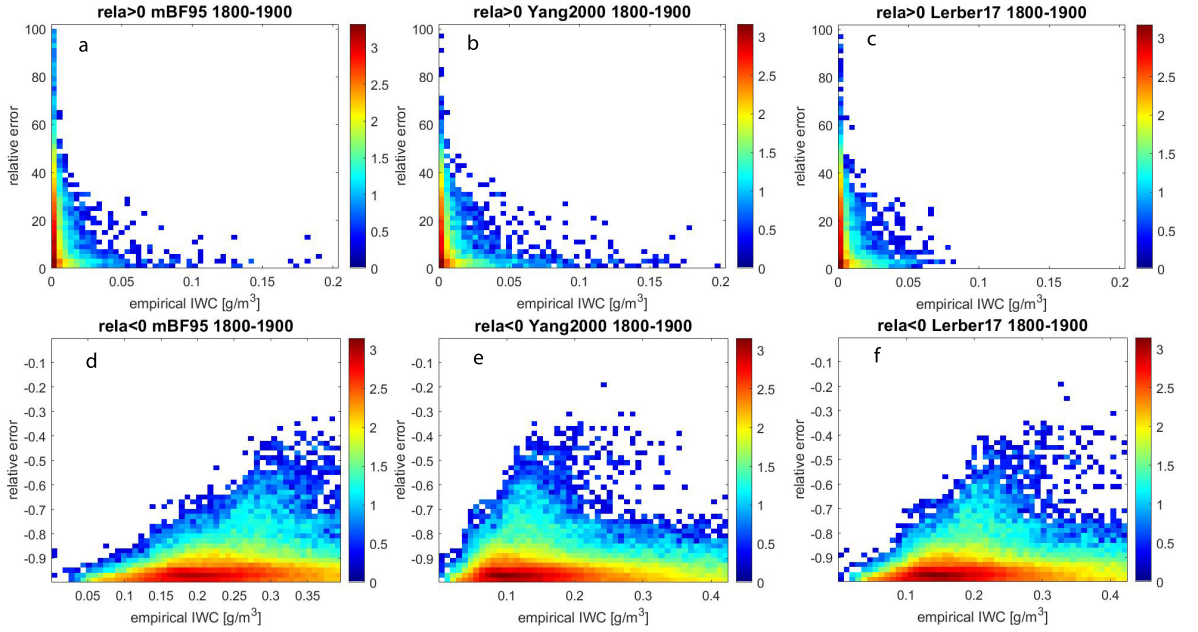

Figure 6.23: 2D histograms of relative error vs. empirical IWC corresponding to three scenarios in Figure 6.22: When relative error > 0: (a) modified BF95, (b) Yang2000 and (c) Lerber17. When relative error < 0: (d) modified BF95, (e) Yang2000 and (f) Lerber17. The color represents the number of bins, displayed on a logarithmic scale with a base of 10.

To give an intuitive view of the difference of BR and empirical IWC, the histograms of difference

between BR and empirical IWC are shown in Figure 6.24. The difference is calculated as:

$$log_{10}(BRIWC) - log_{10}(IWC_{em}) \tag{6.4}$$

The mean and standard deviation of the difference are shown in histograms. The absolute mean difference of BRIWC using modified BF95 is the smallest in three m(D), while the Yang2000 results to the largest bias.

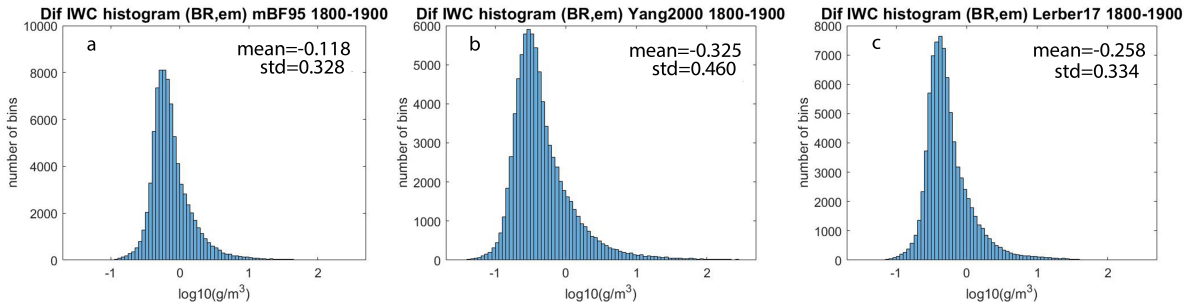

Figure 6.24: Histograms of difference of IWC between empirical model and bulk retrieval with m(D) of : (a) modified BF95, (b) Yang2000 and (c) Lerber17.

The small IWC from both BR and SR, when compared with empirical IWC, might (partly) result from overestimation of particle size. An overestimation of size and subsequently mass might result from the presence of supercooled liquid at low altitude (Section 6.1.4) and the effect of viewing geometry of radar [22]. As one can see from the comparison of BR profiles above, large retrieved mass (Yang2000, Figure 6.17 (b)) leads to small NOP (Figure 6.18 (b)) according to Section 5.5. Then small NOP determines that IWC is also small, because the increase of mass is not enough to compensate the decrease of NOP. The usage of T-matrix instead of better scattering models for aggregates (e.g. methods based on Rayleigh-Gans theory) in the retrieval of NOP should lead to larger NOP and thus larger IWC when mass retrieval is not affected, because soft spheroid underestimates the backscatter for large aggregates [44]. The effect of potential riming on retrieved IWC is uncertain, though riming is considered insignificant in this event. For rimed aggregates, the size will be overestimated by Westbrook2006 (Section 2.5.2), but this will partly compensate the usage of a m(D) for unrimed aggregates in retrieval of mass. The impact of riming on the retrieved NOP is also unclear. Hence, as a combination of NOP and mass, the impact of riming on retrieved IWC is uncertain.

6.1.3. Comparison of bulk and spectral retrieval results

The comparison of BR and SR retrieval results can reveal their consistency. The profiles of retrieved AR, D_{max} and density are computed differently for BR and SR in terms of averaging within a spectrum. Hence, only IWC (IWP) and NOP profiles can be quantitatively compared, as they both represent integrated quantities.

Unlike BR profiles whose valid height-time bins are directly visible, SR profiles are typically affected by the loss of velocity bins with valid data. Therefore, before the comparison of BR and SR results, it is good to know how serious the loss of valid velocity bins is in SR profiles. To give an overview of the loss of bins in SR profiles, preserved bins ratio is calculated for every time step by dividing the number of velocity bins containing retrieved NOP with the number of velocity bins that contain sDWR (no limit to sDWR value). For Event A, the preserved bins ratio is shown in Figure 6.25.

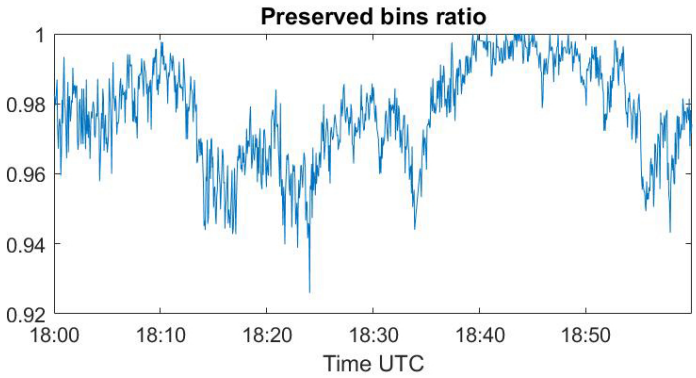

Figure 6.25: The preserved bins ratio of Event A.

From Figure 6.25, one can conclude that most of the velocity bins initially with data are kept, and therefore contribute in SRIWC, SRIWP and SRNOP profiles. Hence, the difference between SR and BR profiles of IWC(IWP) and NOP are not expected to be caused mainly by the loss of bins during spectral retrieval.

6.1.3.1 Comparison of IWP

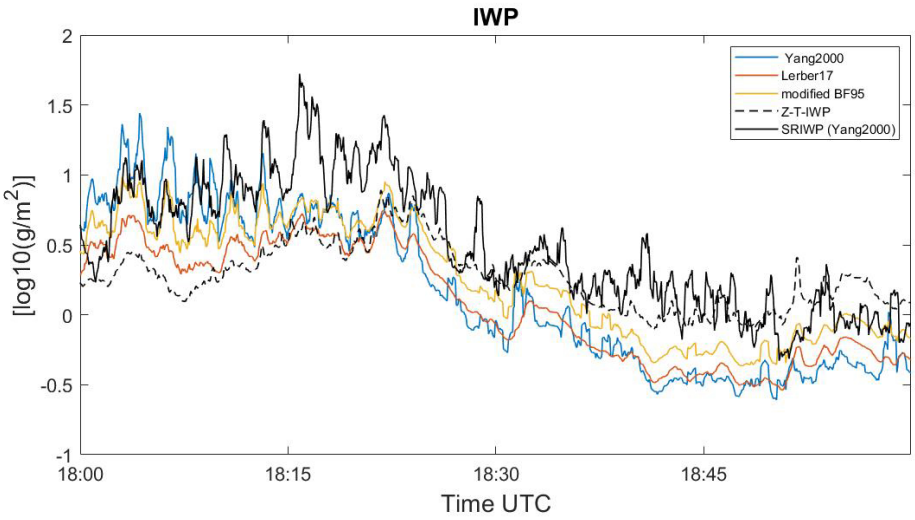

Figure 6.26: IWP from bulk retrieval with three m(D): Yang2000 (blue curve), Lerber17 (red curve), modified BF95 (yellow curve). The SRIWP (black solid line) and empirical IWP (black dash line) are also shown.

The bulk retrieved IWP (BRIWP) using different m(D) are compared with SRIWP and empirical IWP in Figure 6.26. All BRIWP tend to be smaller than empirical IWP from 18:25 to 19:00 while the SRIWP is closest to empirical IWP during this period. From 18:00 to 18:25, however, all retrieved IWP tends to be larger than empirical IWP. Nevertheless, BRIWP gradually approaches empirical IWP as time approaches 18:25. The IWP of Lerber17 is closest to empirical IWP during this time. Overall, BRIWP of Yang2000 is the one most different from empirical IWP for entire hour. Notably, SRIWP is found to be larger than BRIWP during most of the time.

6.1.3.2 Comparison of NOP

In order to compare the NOP profiles from bulk and spectral retrieval, the histograms of the difference between them are plotted in Figure 6.27, with different m(D) for bulk retrieval. The difference is computed as:

$$log_{10}(BRNOP) - log_{10}(SRNOP)$$

The BR NOP with Lerber17 (Figure 6.27 (c)) exhibits the minimum absolute mean difference compared to SR NOP, while the other two BRNOP have similar bias with opposite sign. One may expect the bulk and spectral retrieved NOP both using Yang2000 should be closest to each other, but this is not the case.

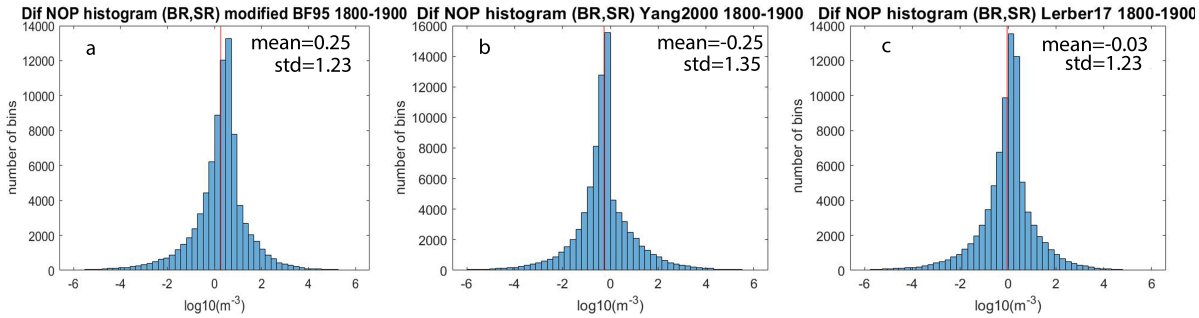

Figure 6.27: Histograms of NOP difference between spectral and bulk retrieval with m(D) of : (a) modified BF95, (b) Yang2000 and (c) Lerber17. The red lines indicate the mean bias. The spectral retrieval always use Yang2000.

To provide another perspective of the difference, the relative difference is computed for BR and SR profiles of NOP as:

$$(BRNOP - SRNOP)/SRNOP$$

and the histograms of relative difference are shown in Figure 6.28. The total number of bins in three scenarios is 82339, while the number of bins with negative relative difference is included in Figure 6.28.

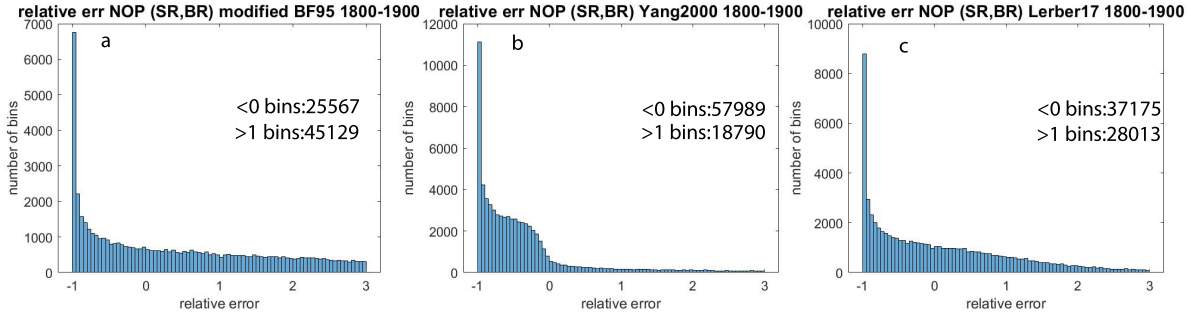

Figure 6.28: Histograms of relative NOP difference between spectral and bulk retrieval with m(D) of : (a) modified BF95, (b) Yang2000 and (c) Lerber17. The spectral retrieval always uses Yang2000.

In Figure 6.28 (b), the relative error of BRNOP using Yang2000 is concentrated in the negative part of the x-axis, a feature not observed in figures (a) and (c). This indicates that SRNOP generally tends to be larger than BRNOP when Yang2000 is used. For modified BF95 and Lerber17, more BRNOP tends to be larger than SRNOP. In figure (a), BRNOP using modified BF95 results in the most bins with larger BRNOP than SRNOP which used Yang2000 in default.

6.1.4. The impact of ignoring the attenuation caused by liquid in retrieval

As introduced before, the DPIA of potential supercooled liquid is ignored in (s)DWR, as the MPC events are with low LWP. However, such practice can result in some error in retrieved results. Such error in the worst case is estimated as described in Section 5.8 for D_{max} and mass. The discussion only considers the extra DPIA that supercooled liquid could cause. The riming effect of aggregates is not discussed here.

Firstly, the maximum potential DPIA caused by supercooled liquid is estimated for event A as described in Section 5.8. The cloud base (red dash curve) is shown in Figure 6.29 left and the resulting DPIA for this case is shown in Figure 6.29 right.

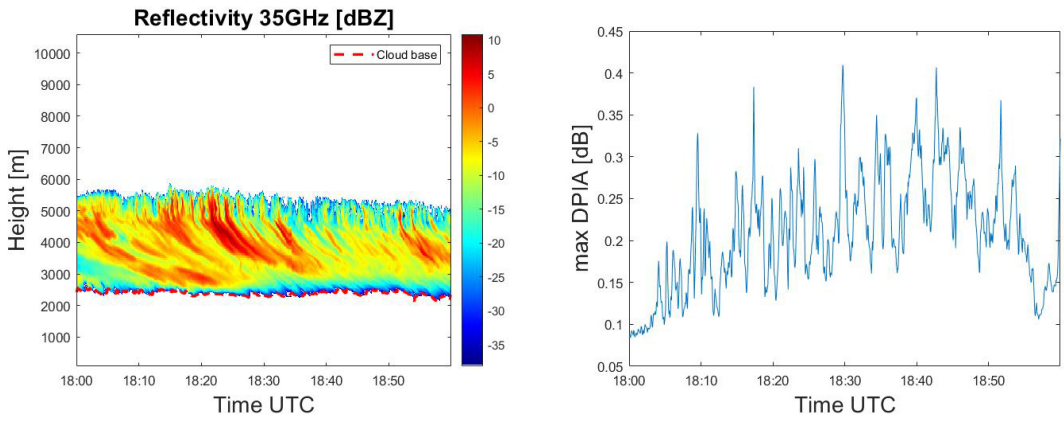

Figure 6.29: Event A. Left: The extracted cloud base. Right: Maximum potential DPIA

The potential DPIA of liquid in DWR will lead to potential error in size retrieval process. The largest possible DPIA caused by liquid is about 0.4dB at 18:30. In Figure 6.30, the maximum potential error of D_{max} (figure a) and mass (figure b) resulting from DPIA of liquid is shown. They're calculated as described in Section 5.8. When a sDWR value is measured at a given time, the maximum potential error of D_{max} and mass caused by supercooled liquid is given by the color. Also, the potential relative error of D_{max} and mass in logarithm are computed for Figure 6.30 (a) and (b) and shown in figure (c) and (d). For D_{max}, the potential relative error is computed as:

$$log10((D_{max,r} - D_{max,t})/D_{max,t}) \tag{6.5}$$

where the $D_{max,r}$ and $D_{max,t}$ are the D_{max} with and without the contribution of potential DPIA from liquid, respectively. The relative error of mass is computed similarly in logarithm.

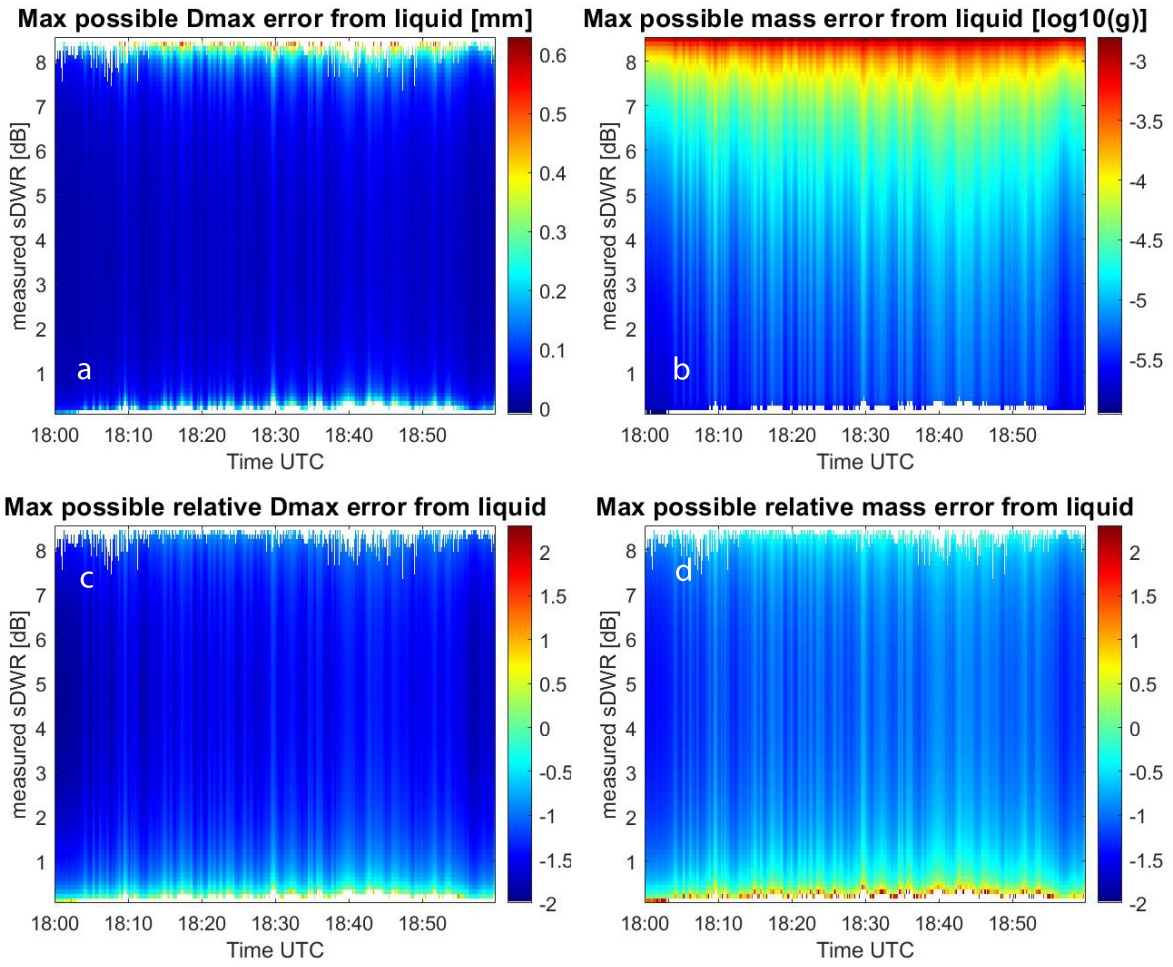

Figure 6.30: Maximum potential D_{max} error (a) and mass error (b) by ignoring liquid. Maximum potential relative error of D_{max} (c) and mass (d) in dB.

For a particle with DWR close to retrieval limits, the possible error of D_{max} is larger (figure (a)), as explained in Section 5.8. However, the possible error of mass is large only when the particle size is large, as shown in Figure 6.30 (b). For particle size, the potential relative error of the smallest particles can be quite large (figure (c)), but for most cases the relative error can be about 10% (deep blue color, -1 in the figure). The potential relative error of particle mass is especially large for small particles (figure (d)), and for many cases the potential relative error can be about 30% (light blue color, -0.5 in the figure). Overall, the potential relative error of mass is larger than that of D_{max}. One can conclude that with under-corrected attenuation or any other extra positive contribution in (s)DWR, the mass is more affected than D_{max}. But this conclusion is only conclude for the m(D) of Yang2000.

6.1.5. Summary

Event A is the test case for the retrieval process, with all conditions relatively ideal (low LWP, small ZDR and proper DWR). The retrieved spectra are consistent with previous findings and can be utilized to derive exponential PSD. The SR profiles also exhibit consistency with each other, though they're noisier and affected by wind shear. The SRIWC is noisy and generally smaller than empirical IWC. The SRIWP appears to be enlarged by the presence of non-spherical particles. Compared to power-law m(D), the Yang2000 results in larger retrieved density, smaller NOP, more spherical shape and eventually smaller IWC. But BR and SR IWC are all prone to be smaller than empirical IWC. Also, BRNOP is generally smaller than SRNOP when Yang2000 is applied. When supercooled liquid is ignored, the potential relative error of mass is larger than that of D_{max}.

6.2. Event B

Event B is the next hour of Event A. This event reveals some more weaknesses of the retrieval process, especially the usage of DWR-size relation for unrimed aggregates in possibly rimed aggregates and in the case of slanted-viewing radar. Figure 6.31 presents the radar measurement profiles of this case. During 19:20 to 19:43, DWR (Figure 6.31 (c)) exhibits large values with some parts over 10dB. The reason will be looked into later. The DWR of the lower cloud from 19:55 to 20:00 also approaches 8dB. In Figure 6.31 (d), ZDR of about 1dB can be seen during 19:10 to 19:38 in the lower part of the cloud, while the largest ZDR occurs at around 19:50. The upper cloud from 19:40 to 20:00 is probably not a cloud with much supercooled liquid but an ice cloud, though its ZDR and DWR are close to zero. The ZDR above 5900m cannot be calibrated for the reason mentioned in Section 5.4.1. Hence, ZDR of the upper cloud should be slightly positive because all the known calibration values (dB) are negative. In this case it should contains mostly tiny ice particles, since LWP during that time is small. The largest LWP was measured at around 19:42 by radar receiver (Figure 10 right) with more than $90g/m^2$. Overall, slight riming is expected in this cloud.

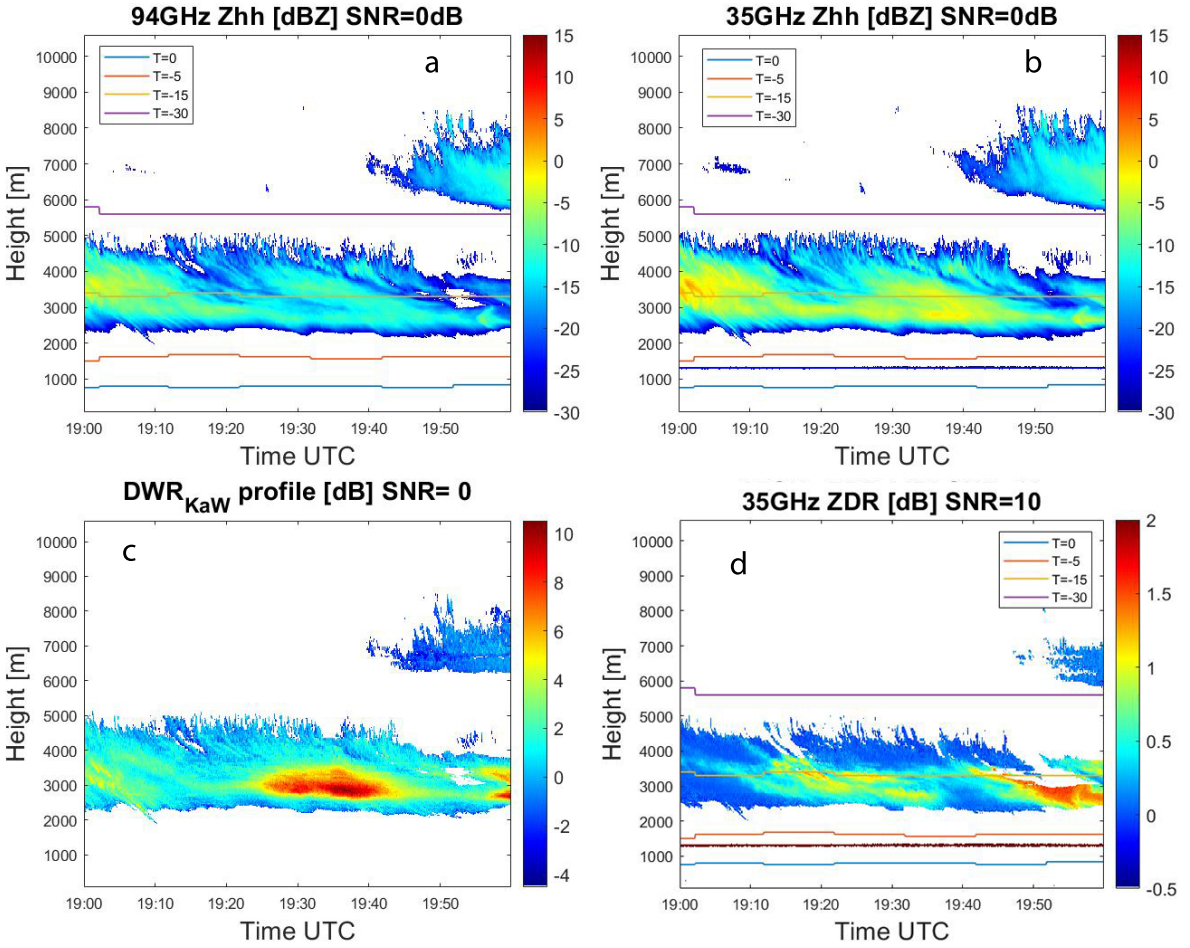

Figure 6.31: Radar measurement profiles with correction and calibration of Event B: The order and names of figures are same as Figure 6.2

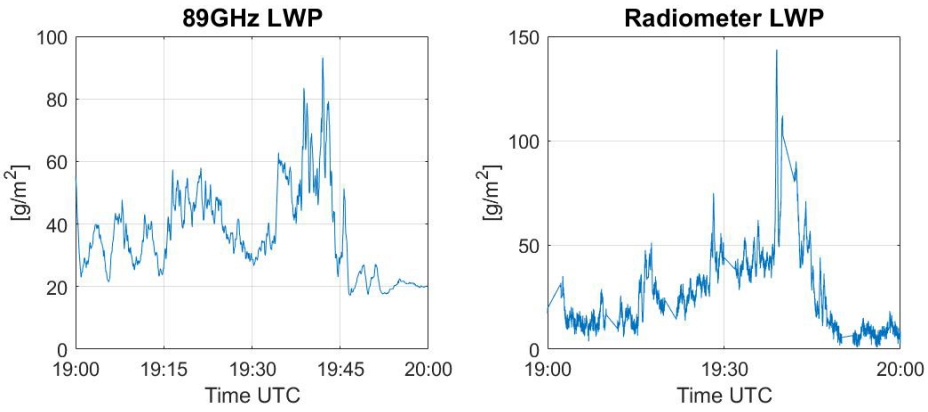

Figure 6.32: LWP measurements of Event B. Left: LWP measured by the receiver on the radar at 94GHz. Right: LWP measured by vertically-pointing radiometer.

6.2.1. Spectral retrieved results

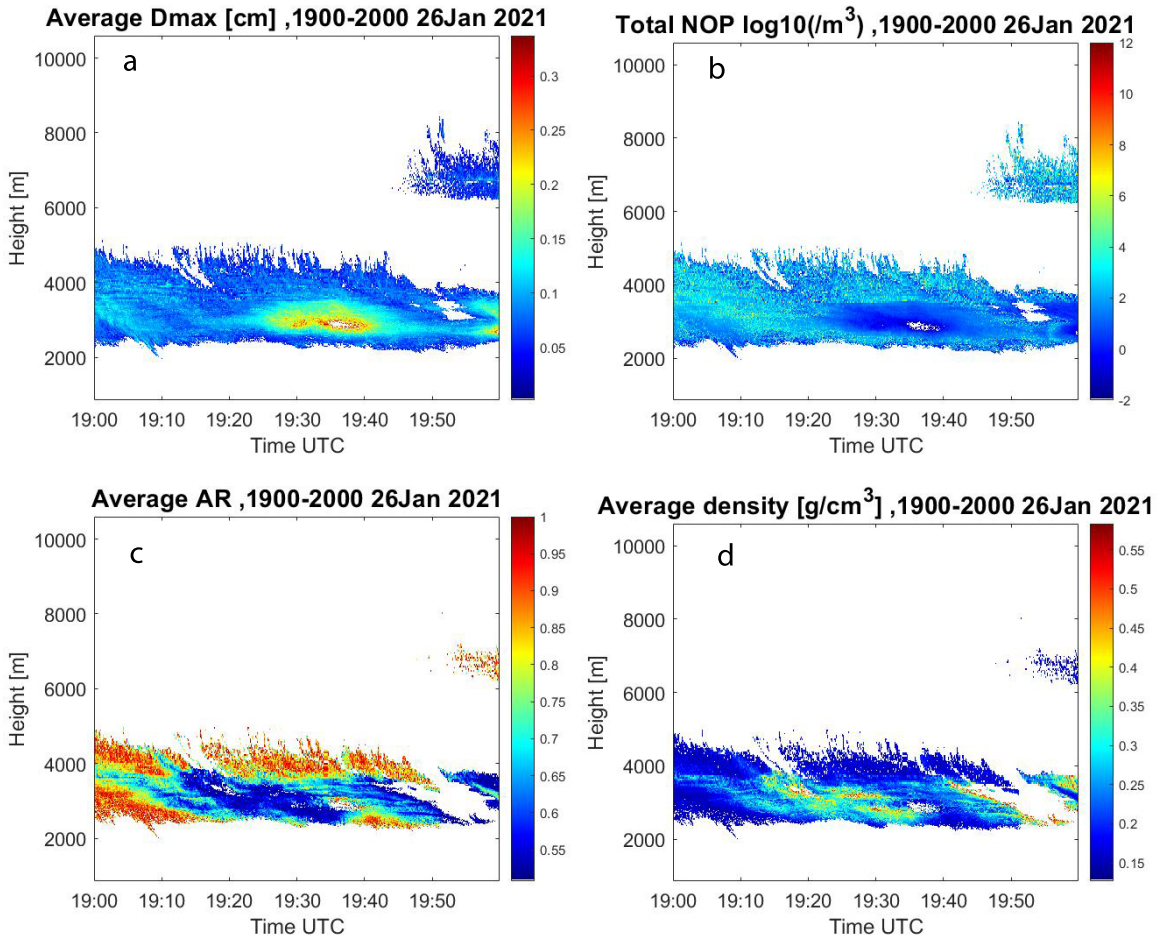

Figure 6.33: Resulting profiles of Event B. Same as Figure 6.9.

The SR profiles are shown in Figure 6.33. In all the retrieved profiles, the missing part at around 19:35 is due to sDWR which is larger than maximum allowed input of 8.5dB. The low value of NOP near the missing region is probably also due to the same reason. The extra missing parts in AR and density profiles are due to the limit of ZDR LUT. Overall, although consistency remains in resulting profiles, the quality is seriously affected for different reasons.

The SRIWC profiles are shown in Figure 6.34 left and compared with the empirical IWC (Figure 6.34 right). The quality of the SRIWC in Figure 6.34 left is not satisfying. From 19:00 to 19:20 SRIWC is consistent with empirical IWC despite being noisier and generally smaller, while for the rest of the hour SRIWC is significantly smaller. As confirmed by comparing IWP in Figure 6.35 left, the retrieved IWC is smaller for most of the time during 19:20 to 20:00.

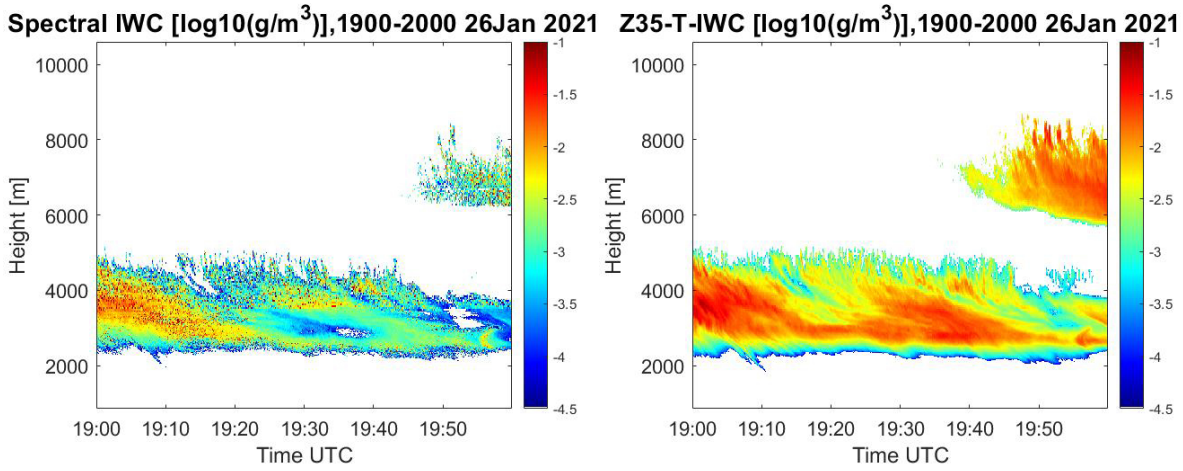

Figure 6.34: SR IWC (left) and empirical IWC (right) of Event B.

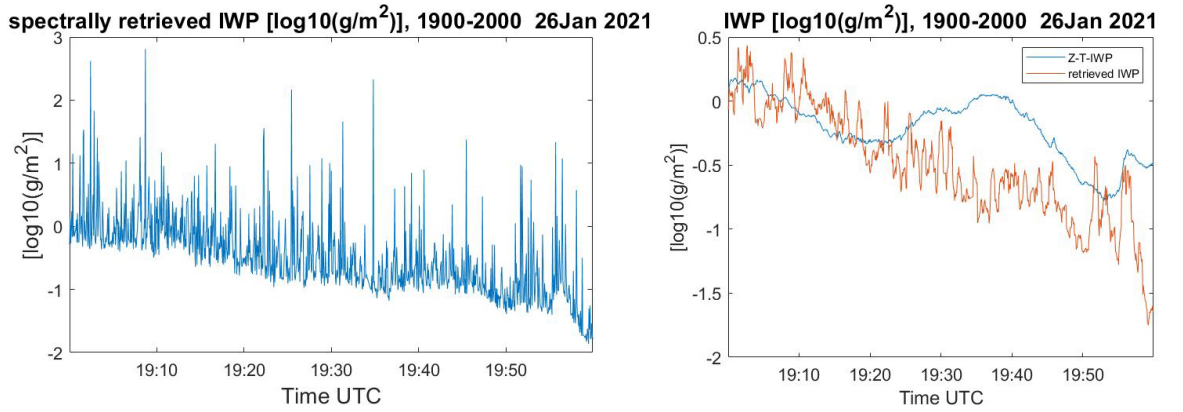

Figure 6.35: IWP of Event B. Left: SR IWP. Right: Comparison of empirical IWP and smoothed SR IWP (moving average of 36 seconds).

The loss of many valid velocity bins due to large sDWR is considered to be the main cause of the smaller IWC in Figure 6.35 right. This conclusion can be reached by calculating the ratio between the number of bins with sDWR larger than 8.5dB and number of bins with positive sDWR at each time step, which is shown in Figure 6.36. The good correspondence of the time ranges with large ratio and the smaller IWP (Figure 6.35 right) indicates that they have direct connection.

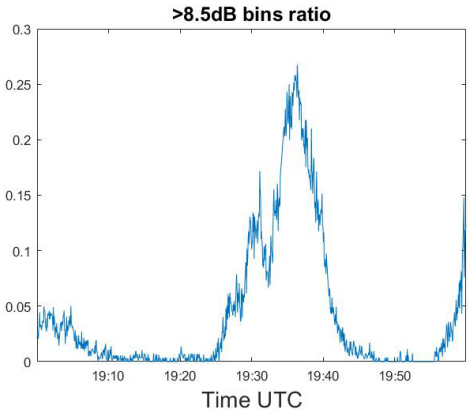

Figure 6.36: Event B: The ratio between the number of bins with sDWR larger than 8.5dB and the number of bins with positive sDWR at each time step.

6.2.2. What can be the cause of large sDWR

In the case of slant-viewing radar, both riming and large sZDR can result in a sDWR larger than 8.5 dB, if the type of aggregates is not considered. One can notice that the ZDR profiles in Figure 6.31 (d) at around 19:30 doesn't correspond well to the region with large DWR in Figure 6.31 (c) at the same time. Thus it is reasonable to suspect that the cause of the region with large DWR at that time is riming, though other causes might be possible. According to the DWR-size relation Westbrook2006 [39], unrimed aggregates can't exhibit DWR_{KaW} larger than about 8.5dB, though [33] found that the limit can be a bit larger. To determine the cause of large sDWR in this case, histograms are plotted for sDWR larger than 8.5dB (Figure 6.37 left) and corresponding sZDR (Figure 6.37 right) for each time step. The LWP measured by radar receiver is also overlapped in both figures to characterize the possibility of riming. Two time intervals are shown with green lines (a and b) to be discussed.

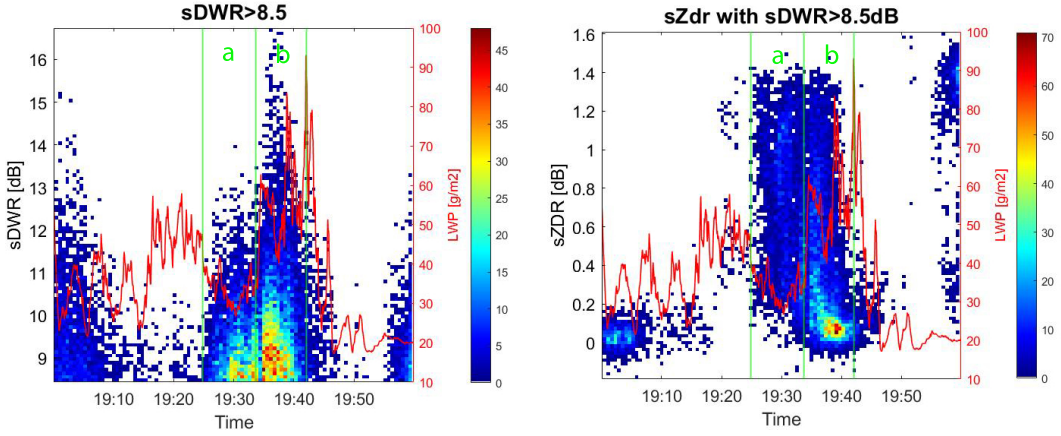

Figure 6.37: Event B. The histogram of number of velocity bins of sDWR larger than 8.5dB (left) and the histogram of corresponding sZDR (right) at all time step. Two time intervals a and b are shown by green lines.

In Figure 6.37 left and right, both time ranges (a and b) contain sDWR larger than 8.5dB as well as large sZDR. However in the time interval a, the LWP is significantly lower than time range b. At about 19:37, the histogram of sDWR exhibits a peak of sDWR while there are more bins with large sZDR (0.2 to 0.4dB) in the histogram of sZDR. Thus for time interval b, the cause of large sDWR can be both the large sZDR and riming. For time interval a, it is expected that the large sZDR plays a bigger role in the large sDWR than in interval b, but one can't rule out the effect of riming despite the lower LWP. It is also worth mentioning that LWP is not a decisive indicator of riming. Spatial relation between radar beam and the fall streak of ice particles is unknown, and therefore rimed particles can be produced outside the radar beam and then enter the beam. The time range between 19:00 and 19:10 exhibits sZDR close to zero, but at the same the sDWR exhibits quite some large values and LWP is relatively

low. It's hard to say what is the cause of large sDWR in this case. As mentioned in [33], the maxima of DWR_{KaW} can reach 12dB for aggregates of bullet rosettes, but it's not possible to distinguish in current radar observation. In conclusion, since the real size, shape and density of particles are unknown, it is challenging to disentangle different effects on DWR in radar measurements.

6.2.3. Comparison of BR and SR IWC

BRIWC is expected to be less affected by the extreme values in sDWR due to the integrated variables it is based on. The SRIWC, on the other hand, suffers from the loss of valid velocity bins. To find out if the bulk retrieval can help improve the IWC profiles with the presence of large (s)DWR in event B, the BR IWC is shown in Figure 6.38 (a) to compare with SR IWC (Figure 6.38 (b)) and empirical IWC (Figure 6.38 (c)). Both SR and BR IWC use Yang2000.

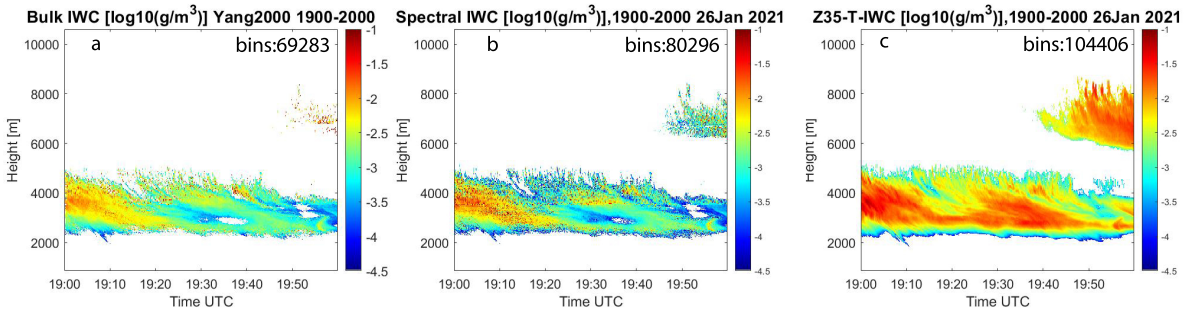

Figure 6.38: Event B: (a) BR IWC (b) SR IWC (c) Empirical IWC. The number of points in the profiles are shown in each figure.

In Figure 6.38, although SR IWC contains more points than BR IWC, it is also much noisier. The SR IWC contains more points because even if some bins are removed due to small particle size (small sDWR) and noise (The upper cloud later this hour) or sDWR larger than 8.5dB (19:30-19:40, around 3000m), other bins in the sDWR are still valid to contribute in profiles. This can also explain why SR IWC is noisier, as some valid velocity bins lack representation in the entire spectrum. But in bulk retrieval, a height-time bin is either kept or removed, which means that there are no spectra partly kept. In Figure 6.39, the histogram of the difference between SR, BR IWC and empirical IWC are shown. The differences are computed the same as Equation 6.1 and Equation 6.4.

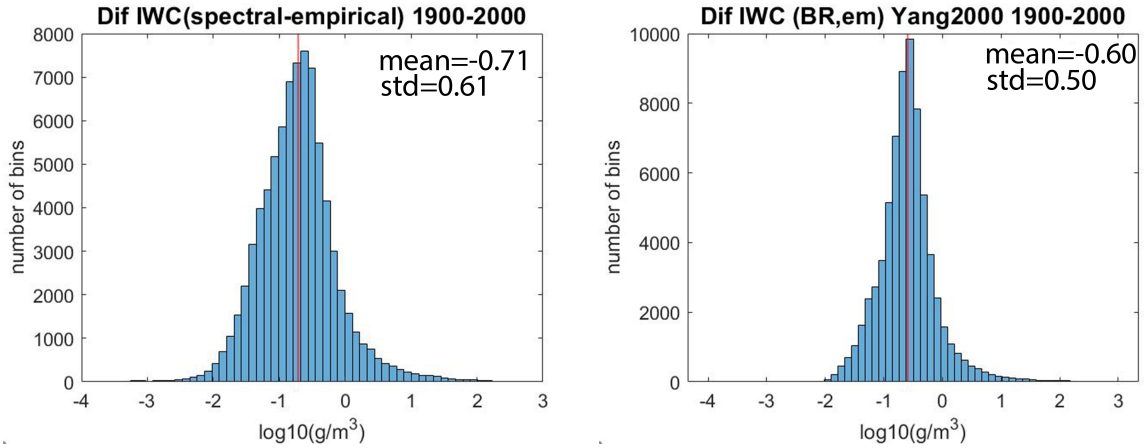

Figure 6.39: Event B differential IWC Histograms. Left: Difference between SR IWC and empirical IWC. Right: Difference between BR IWC and empirical IWC.

From Figure 6.39, one can conclude that the BR IWC has a mean closer to empirical IWC and a smaller standard deviation, though both retrieved IWC are generally smaller than empirical IWC, similar to event A.

6.2.4. The potential DPIA caused by LWP

Similar to Event A, the DPIA of LWP hypothetically concentrated at the cloud bottom is derived. The maximum potential DPIA caused by supercooled liquid is shown in Figure 6.40 right with the extracted cloud base in the left figure. The potential DPIA is not large compare to event A. The maximum potential DPIA at about 19:42 is the largest value (0.57dB) during this hour.

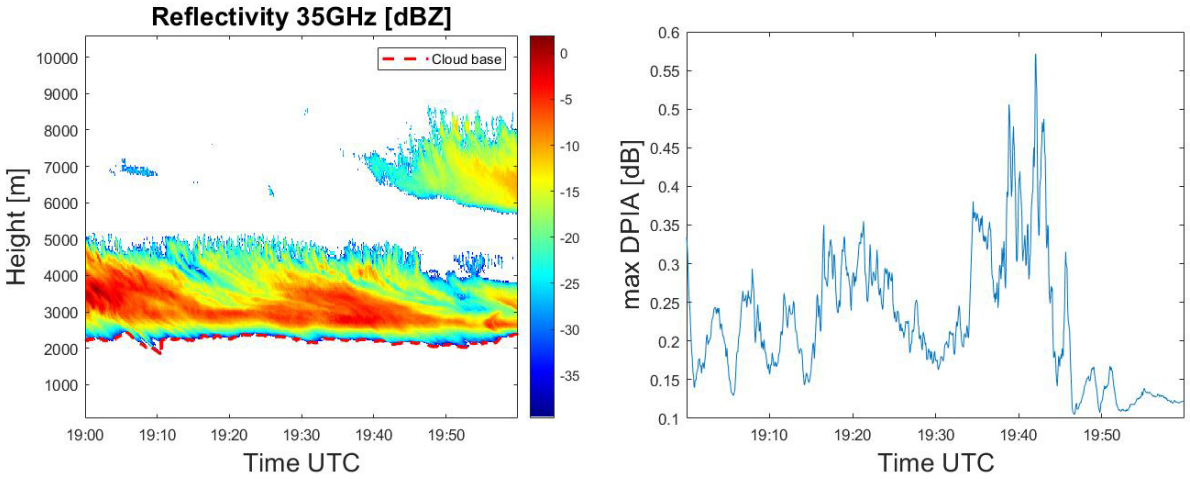

Figure 6.40: The potential DPIA from LWP of Event B. Left: The extracted cloud base. Right: Maximum potential DPIA caused by supercooled liquid

6.2.5. Summary

Event B is a case with (s)DWR larger than 8.5dB and large ZDR. The loss of valid sDWR results in small IWC and IWP. The cause of large sDWR is complicated and can't be determined with existing measurements. In this case, the BRIWC and SRIWC have different advantages and disadvantages, but they're both affected by the loss of valid sDWR.

7

Conclusions and Recommendations

This chapter concludes all the findings in the research of microphysical retrieval within mixed-phase clouds with low liquid water path, which involved radar measurements of sDWR, sZDR and sZhh. Some recommendations are proposed for future studies on the same topic. The conclusions below are reached by studying the two events (Event A and B):

7.1. Conclusions

How can we design a semi-physical process to retrieve spectra of aggregate size, density, aspect ratio and number concentration in mixed-phase clouds using cloud radar measurements?
To assist the development of retrieval process, scattering simulations employing the T-matrix were conducted to study the sensitivity of radar measurements to the microphysical properties of ice particles. ZDR is found to be mainly affected by density and overall shape (aspect ratio) of ice particles, while radar reflectivity depends more on size and mass of ice particles.

The differential attenuation of supercooled liquid could not be estimated reliably, and therefore mixed-phase cloud events with low liquid water path were selected to limit such contribution in sDWR and DWR. With mixed-phase cloud events selected, spectra dealiased and sDWR computed, calibration of sZDR and gas attenuation correction of sDWR and sZhh were applied. Using DWR-size relation Westbrook2006 from [39], m(D) relation derived from Yang2000 [21] and look-up tables produced by T-matrix simulation, the spectral D_{max}, density, mass, aspect ratio and number concentration of particles were obtained from sDWR, sZDR and sZhh. The Westbrook2006 is considered to be more suitable for mixed-phase cloud with low liquid water path than the relation derived from T-matrix because it takes the internal structure of aggregates into account, though it is originally derived for unrimed aggregates and vertically-pointing radar. The usage of Yang2000 can bring reasonable aspect ratio when T-matrix is involved in the retrieval [18]. The iteration process in the retrieval of aspect ratio and density works well, and hence correctly converged results can be obtained. The number concentration of particles was retrieved with the approach from [17], but T-matrix was used instead for its simplicity. IWC, which can be computed using retrieved mass and number concentration of particles, is a byproduct of the microphysical retrieval process.

Are there cases for which we can retrieve the aggregate size distribution?
The test case was studied for this purpose. The 2D histograms of log10(N(D)) versus D exhibit linear pattern, which is consistent with previous findings that the exponential function is suitable for aggregates [18]. By fitting straight lines to the 2D histograms at different height ranges, N(D) were retrieved for a population of particles. The retrieved D_0 increases while N_w decreases as ice particles fall. This aligns well with what is expected for aggregation process.

What's the difference between ice water content retrieved based on a purely empirical relation and the semi-physical process proposed?
Using the retrieved mass and number concentration profiles, the IWC profiles were computed and compared with empirical IWC profiles [66]. In general, although spectral retrieved IWC is noisier, there's

good spatial correlation between them. However, the spectral retrieved IWC is suspected to be affected by the existence of non-spherical particles and larger IWC was retrieved. On the other hand, spectral retrieved IWC is vulnerable to the loss of valid velocity bins and exhibit smaller value than empirical IWC when this occurs. Overall, the retrieval of IWC is feasible based on the spectral retrieved mass and number concentration, but some challenges limit the quality of spectral retrieved IWC.

How does the usage of different mass-size relations affect retrieval results?
The proposed retrieval process was applied to bulk variables. Without the need to average for obtaining height-time profiles, bulk retrieval is convenient for comparing results intuitively. Bulk retrieved microphysical properties with different m(D) were compared. The m(D) Yang2000 provides a large, near constant density for aggregates compared to common power-law relations. It leads to large retrieved mass, smaller number concentration of particles and more spherical overall shape. The usage of Yang2000 has significant impact on retrieved aspect ratio when T-matrix is used, which is consistent with the conclusion in [18]. On the other hand, the usage of m(D) providing low density such as modified BF95 [52] results in more non-spherical retrieved shape and larger number concentration of particles. In terms of IWC, the influence of different m(D) is not quite evident on bulk retrieved IWC. The modified BF95 provides mean bulk retrieved IWC closest to the empirical IWC while Yang2000 leads to the smallest IWC overall. In conclusion, the mass-size relation has significant impact on all retrieved microphysical properties except maximum dimension.

What are the differences between retrievals based on bulk variables compared to spectral data?
The comparison between bulk and spectral retrieved profiles revealed that bulk retrieved profiles are smoother but with less points (height-time bins with valid results). The bulk and spectral retrieved profiles generally exhibit close values, but spectral retrieval leads to noisier profiles. Besides, spectral retrieved profiles of aspect ratio, density and maximum dimension are affected by wind shear. The bulk and spectral retrieved profiles of aspect ratio, density and D_{max} cannot be compared quantitatively, because these spectral retrieved profiles were computed by averaging spectral results, which is different from bulk retrieved profiles. Thus, only IWC and number concentration profiles can be quantitatively compared. In terms of IWC, bulk retrieved IWC exhibits larger value in regions where spectral retrieved IWC suffers from the loss of data points, while spectral retrieved IWC profiles can provide values where bulk retrieved IWC can't. Overall, bulk retrieved IWC has a closer mean to empirical IWC, though both bulk and spectral retrieved IWC exhibit smaller mean compared with empirical IWC. In terms of number concentration, the mean difference between spectral and bulk retrieved number concentration is relatively small.

How does the neglect of the differential attenuation caused by supercooled liquid affect the retrieved size and mass?
The differential attenuation caused by liquid was taken into account in DWR-size relation (Westbrook2006) and DWR-mass relation (Westbrook2006 plus Yang2000) in the simulation, in order to study the potential consequences. With Westbrook2006 applied to the DWR_{KaW}, the maximum dimension is overestimated for the largest and smallest retrievable particles when the differential attenuation is ignored. Such overestimation is more severe for the largest retrievable particles than the smallest. When Yang2000 is exploited subsequently to retrieve mass, the overestimation of mass occurs especially to the largest retrievable particles. In terms of relative error, the one of maximum dimension is particularly large for the smallest particles, which is similar to the one of mass. However, the relative error of mass is overall larger than that of maximum dimension.

7.2. Recommendations

As one can notice in the previous section, conclusions from this research are primarily drawn from two case studies. To draw more robust conclusions, future studies should investigate additional mixed-phase cloud events with low liquid water path.

7.2.1. Radar hardware

Currently the sensitivity of the radar at 94GHz is lower than that at 35GHz. Parts of spectra (sDWR and sZ_{hh94}) were lost due to such issue, which include the smallest and largest particles. The spectra at 94GHz also appear noisier than those at 35GHz. Hence, increase of the power of radar at 94GHz

is essential to enhancing its sensitivity and improving the quality of its Doppler spectra. If the width of spectrum at 94GHz can be the same or even larger than that at 35GHz, the calculated DWR will be more accurate and the information of the tiniest and largest particles can be reserved.

Besides, since the regions where rimed particles exist and the degree of riming are unknown, it is not possible to employ different m(D) relations for different cloud regions based on riming condition. This will cause error in retrieved IWC which is sensitive to mass. Having a radar pointing towards the zenith can provide mean Doppler velocity profiles and help determine the riming events in clouds by providing terminal velocity. This can be realized by changing the elevation angle of a radar once a while or having a second radar.

In this research, an ice particle that is too large for DWR-size relation Westbrook2006 [39] is possible and can cause underestimation of particle size, though it was shown in Section 5.3 that it is expected to be uncommon. The reason is that a large particle might be within the oscillation part of backscattering cross section function and the DWR-size relation is no longer monotonically increasing as shown in Figure 5.3. In this case, triple frequency is a powerful ability of cloud radars, because with a third lowest frequency, the second DWR is able to provide information about size for larger particles. Recent studies about ice clouds or mixed-phase clouds start to exploit the potential of extra information provided by a third frequency. The extra information is related to the inner structure of ice particles, which was not able to obtain from dual frequencies. An extra frequency lower than 35GHz will be helpful for not only the size retrieval of larger particles [17] but also for detection of riming and revealing PSD [33, 31]. Moreover, an extra lower frequency (e.g. Ku band) is practically unattenuated by even large ice particles (e.g. snowflake), and therefore can be used to correct the attenuation due to ice at higher frequencies [7].

7.2.2. Retrieval process

The limitation of the usage of T-matrix in aggregates has been mentioned previously. Although the usage of the m(D) of Yang2000 to some extend compensates the error brought by T-matrix related to retrieval of aspect ratio, it results in large retrieved density and mass, which is unrealistic. Therefore, the usage of T-matrix along with Yang2000 m(D) is a kind of compromise. To obtain mass, density, number concentration and IWC with better quality, one can consider using power-law m(D) in the retrieval process of mass and number concentration, while using Yang2000 for the retrieval of aspect ratio. However, it would be nice to use power-law m(D) in the entire retrieval process because they're more common, widely studied and based on in-situ measurements. But in this case, scattering models such as DDA or RGA need to be used simultaneously and T-matrix should be given up in the retrieval. Moreover, although the DWR-size relation Westbrook2006 can be used in slightly riming cases with limited bias, it can't deal with large slightly-rimed aggregates with DWR larger than about 8.5dB. This limitation can be very challenging to deal with, since it appears to require detailed knowledge about the degree of riming of aggregates. Much more research is needed in order to apply different DWR-size relations according to the degree of riming.

The retrieved profiles of IWC and NOP could benefit from the combination of spectral retrieved and bulk retrieved profiles. Spectral retrieved profiles have better coverage while bulk retrieved profiles are less noisy. It is possible to come up with an approach to keep both advantages. For the density profiles, the bulk average density is a better approach to present retrieved results. It can be computed using IWC and the total volume of ice particles. Using retrieved microphysical properties to reproduce radar measurements which were not involved in retrieval and compare them with the original radar measurements can be a potential approach for verifying the consistency of the methodology.

Current retrieval process focuses on ice aggregates in cold clouds as previous research related to ice clouds [17], but ice crystals also exist in cold clouds, especially at lower temperature. The prevalence of aggregation depends on number concentration, mass, shape of ice particles and environmental factors (temperature, turbulence and vapor pressure etc.). In future research, it would be nice to treat ice aggregates and crystals differently in retrieval process, though the improvement brought by such practice is uncertain.

7.2.3. Forward modelling

In future studies, scattering simulations using DDA could be used together with realistic microphysical models to study ice particles with complex internal structure. A good summary of such models is given in [35]. A more realistic forward model will benefit the retrieval using radar measurements. The irreplaceability of DDA shows itself in the case of partly rimed aggregates. Neither T-matrix nor Rayleigh-Gans approximation can deal with such kind of ice particles without bringing extra bias.

The limits of studies on the effect of the elevation angle of radar on DWR has also been mentioned before. For large particles with small aspect ratio, the retrieval inevitably includes systematic bias. Hence, a correction of DWR-size relation when radar is not vertically-pointing [39] needs to be studied for general aggregates, preferably using DDA. The ZDR can be used to estimate how much the retrieved size deviates from the size retrieved from vertically-pointing radar at a certain elevation angle for a given aspect ratio. It can provide a crucial correction to DWR for a radar which is acquiring DWR and polarimetric measurements at the same time. The conclusions can help in the case of mixed-phase cloud where riming happens. The difficulty of disentangling the contribution from riming and observation geometry in DWR in Section 6.2.2 might be mitigated by applying such correction, though whether riming affects such correction remains unknown.

In this research, the neglect of ice differential attenuation causes some error in further retrieval. A simulation of forward scattering cross section can be used to provide the estimation of differential attenuation of ice particles, since enough microphysical properties have been initially retrieved for the entire population of ice particles. Then with the correction of the DPIA of ice, final retrieved results can be obtained by repeating the retrieval. But one should notice that radar attenuation correction is subject to mathematical instabilities that can lead to small errors multiplying in a positive feedback loop [7]. Although T-matrix can be used for simulation of forward scattering, it is suggested to use more advanced forward models to avoid large bias.

7.2.4. More types of instruments

Validation of retrieval results

There's no way to directly verify the quality of the results in this research. Although the empirical IWC provides a simple check to retrieved IWC, the retrieved size, mass, aspect ratio and number of particles are not validated using independent data sources. In-situ measurements can be obtained in the future to help validate the result of retrieval. The two-dimensional cloud microphysical optical array probes that can measure PSD [66] are commonly used on plane. It can be used to derive aspect ratio and maximum dimension of ice particles. The IWC can be obtained using a combination of total water content probe and Lyman fluorescence water vapor sensor (FWVS) [46] or a counterflow virtual impactor (CVI) [69]. However, the locations of in-situ measurements are often different from radar measurements and hence the validation remains challenging. In practice, the in-situ measurements which are closest (both spatially and temporally) to radar measurements should be used for validation. Validation of IWC and number concentration are expected to be convenient because there are direct in-situ measurements of them. However, verifying the maximum dimension, density, and aspect ratio can be more challenging, as the same quantities measured by instruments and retrieved from radar signals typically involve different observation geometries and definitions.

Information about riming and supercooled liquid

The lack of information about supercooled liquid and riming affects the retrieval. A depolarization lidar can provide depolarization ratio and backscatter intensity measurements. The depolarization ratio will be close to zero and backscatter intensity will be large when there's a liquid layer in cold clouds. These distinct features allow the determination of the locations of supercooled liquid droplets and helps attenuation correction [70]. Besides, knowing the locations of supercooled liquid means that unrimed regions are known. This might provide assistance in determining the cause of large DWR (Section 6.2.2) since riming effect might be ruled out.

Better estimation of gas attenuation

A radiosonde can be used to provide accurate height profiles of humidity, temperature and air pressure. Unlike a microwave radiometer which is a remote sensing approach, radiosonde makes in-situ

measurements which are considered more reliable. Radiosondes offer better spatial resolution compared to radiometers and have the capability to measure air pressure which cannot be measured by radiometers. The measurements of radiosondes will probably enhance the accuracy of gas attenuation correction compared to using the output of a weather model.

Bibliography

[1] A. J. Heymsfield, C. Schmitt, A. Bansemer, A. Gettelman, P. R. Field, C. Liu, *et al.*, "Contributions of the liquid and ice phases to global surface precipitation: Observations and global climate modeling," *Journal of the Atmospheric Sciences*, vol. 77, no. 8, pp. 2629–2648, 2020.

[2] J. Mülmenstädt, O. Sourdeval, J. Delanoë, and J. Quaas, "Frequency of occurrence of rain from liquid-, mixed-, and ice-phase clouds derived from a-train satellite retrievals," *Geophysical Research Letters*, vol. 42, no. 15, pp. 6502–6509, 2015.

[3] A. Korolev, G. McFarquhar, P. R. Field, C. Franklin, P. Lawson, Z. Wang, E. Williams, S. J. Abel, D. Axisa, S. Borrmann, *et al.*, "Mixed-phase clouds: Progress and challenges," *Meteorological Monographs*, vol. 58, pp. 5–1, 2017.

[4] C. Andronache, *Mixed-phase Clouds: Observations and Modeling*. Elsevier, 2017.

[5] M. D. Shupe, S. Y. Matrosov, and T. Uttal, "Arctic mixed-phase cloud properties derived from surface-based sensors at sheba," *Journal of the atmospheric sciences*, vol. 63, no. 2, pp. 697–711, 2006.

[6] J. Hallett and S. Mossop, "Production of secondary ice particles during the riming process," *Nature*, vol. 249, no. 5452, pp. 26–28, 1974.

[7] J. Leinonen, M. D. Lebsock, S. Tanelli, O. O. Sy, B. Dolan, R. J. Chase, J. A. Finlon, A. von Lerber, and D. Moisseev, "Retrieval of snowflake microphysical properties from multifrequency radar observations," *Atmospheric Measurement Techniques*, vol. 11, no. 10, pp. 5471–5488, 2018.

[8] J. Verlinde, M. P. Rambukkange, E. E. Clothiaux, G. M. McFarquhar, and E. W. Eloranta, "Arctic multilayered, mixed-phase cloud processes revealed in millimeter-wave cloud radar doppler spectra," *Journal of Geophysical Research: Atmospheres*, vol. 118, no. 23, pp. 13–199, 2013.

[9] S. Alexander, G. McFarquhar, R. Marchand, A. Protat, É. Vignon, G. Mace, and A. Klekociuk, "Mixed-phase clouds and precipitation in southern ocean cyclones and cloud systems observed poleward of 64° s by ship-based cloud radar and lidar," *Journal of Geophysical Research: Atmospheres*, vol. 126, no. 8, p. e2020JD033626, 2021.

[10] R. J. Hogan, P. Field, A. Illingworth, R. Cotton, and T. Choularton, "Properties of embedded convection in warm-frontal mixed-phase cloud from aircraft and polarimetric radar," *Quarterly Journal of the Royal Meteorological Society: A journal of the atmospheric sciences, applied meteorology and physical oceanography*, vol. 128, no. 580, pp. 451–476, 2002.

[11] M. D. Shupe, P. Kollias, S. Y. Matrosov, and T. L. Schneider, "Deriving mixed-phase cloud properties from doppler radar spectra," *Journal of Atmospheric and Oceanic Technology*, vol. 21, no. 4, pp. 660–670, 2004.

[12] E. P. Luke, P. Kollias, and M. D. Shupe, "Detection of supercooled liquid in mixed-phase clouds using radar doppler spectra," *Journal of Geophysical Research: Atmospheres*, vol. 115, no. D19, 2010.

[13] J. Bühl, P. Seifert, A. Myagkov, and A. Ansmann, "Measuring ice-and liquid-water properties in mixed-phase cloud layers at the leipzig cloudnet station," *Atmospheric Chemistry and Physics*, vol. 16, no. 16, pp. 10609–10620, 2016.

[14] R. J. Hogan, M. P. Mittermaier, and A. J. Illingworth, "The retrieval of ice water content from radar reflectivity factor and temperature and its use in evaluating a mesoscale model," *Journal of Applied Meteorology and Climatology*, vol. 45, no. 2, pp. 301–317, 2006.

[15] D. Zhang, Z. Wang, A. Heymsfield, J. Fan, and T. Luo, “Ice concentration retrieval in stratiform mixed-phase clouds using cloud radar reflectivity measurements and 1d ice growth model simulations,” *Journal of the Atmospheric Sciences*, vol. 71, no. 10, pp. 3613–3635, 2014.

[16] S. Y. Matrosov, C. G. Schmitt, M. Maahn, and G. de Boer, “Atmospheric ice particle shape estimates from polarimetric radar measurements and in situ observations,” *Journal of atmospheric and oceanic technology*, vol. 34, no. 12, pp. 2569–2587, 2017.

[17] A. I. Barrett, C. D. Westbrook, J. C. Nicol, and T. H. Stein, “Rapid ice aggregation process revealed through triple-wavelength doppler spectrum radar analysis,” *Atmospheric Chemistry and Physics*, vol. 19, no. 8, pp. 5753–5769, 2019.

[18] E. Tetoni, F. Ewald, M. Hagen, G. Köcher, T. Zinner, and S. Groß, “Retrievals of ice microphysical properties using dual-wavelength polarimetric radar observations during stratiform precipitation events,” *Atmospheric Measurement Techniques*, vol. 15, no. 13, pp. 3969–3999, 2022.

[19] F. Tridon, A. Battaglia, and P. Kollias, “Disentangling mie and attenuation effects in rain using a ka-w dual-wavelength doppler spectral ratio technique,” *Geophysical Research Letters*, vol. 40, no. 20, pp. 5548–5552, 2013.

[20] V. N. Bringi and V. Chandrasekar, *Polarimetric Doppler weather radar: principles and applications*. Cambridge university press, 2001.

[21] P. Yang, K. Liou, K. Wyser, and D. Mitchell, “Parameterization of the scattering and absorption properties of individual ice crystals,” *Journal of Geophysical Research: Atmospheres*, vol. 105, no. D4, pp. 4699–4718, 2000.

[22] S. Y. Matrosov, M. Maahn, and G. De Boer, “Observational and modeling study of ice hydrometeor radar dual-wavelength ratios,” *Journal of Applied Meteorology and Climatology*, vol. 58, no. 9, pp. 2005–2017, 2019.

[23] J. Dias Neto, S. Kneifel, D. Ori, S. Trömel, J. Handwerker, B. Bohn, N. Hermes, K. Mühlbauer, M. Lenefer, and C. Simmer, “The triple-frequency and polarimetric radar experiment for improving process observations of winter precipitation,” *Earth System Science Data*, vol. 11, no. 2, pp. 845–863, 2019.

[24] F. Tridon, A. Battaglia, and S. Kneifel, “Estimating total attenuation using rayleigh targets at cloud top: applications in multilayer and mixed-phase clouds observed by ground-based multifrequency radars,” *Atmospheric Measurement Techniques*, vol. 13, no. 9, pp. 5065–5085, 2020.

[25] R. J. Hogan, N. Gaussiat, and A. J. Illingworth, “Stratocumulus liquid water content from dual-wavelength radar,” *Journal of Atmospheric and Oceanic Technology*, vol. 22, no. 8, pp. 1207–1218, 2005.

[26] K. Lamer, M. Oue, A. Battaglia, R. J. Roy, K. B. Cooper, R. Dhillon, and P. Kollias, “Multifrequency radar observations of clouds and precipitation including the g-band,” *Atmospheric Measurement Techniques*, vol. 14, no. 5, pp. 3615–3629, 2021.

[27] H. Li, A. Korolev, and D. Moisseev, “Supercooled liquid water and secondary ice production in kelvin–helmholtz instability as revealed by radar doppler spectra observations,” *Atmospheric Chemistry and Physics*, vol. 21, no. 17, pp. 13593–13608, 2021.

[28] T. Vogl, M. Maahn, S. Kneifel, W. Schimmel, D. Moisseev, and H. Kalesse-Los, “Using artificial neural networks to predict riming from doppler cloud radar observations,” *Atmospheric Measurement Techniques*, vol. 15, no. 2, pp. 365–381, 2022.

[29] L. Mosimann, “An improved method for determining the degree of snow crystal riming by vertical doppler radar,” *Atmospheric research*, vol. 37, no. 4, pp. 305–323, 1995.

[30] C. G. Schmitt, K. Sulia, Z. J. Lebo, A. J. Heymsfield, V. Przybyo, and P. Connolly, “The fall speed variability of similarly sized ice particle aggregates,” *Journal of Applied Meteorology and Climatology*, vol. 58, no. 8, pp. 1751–1761, 2019.

[31] S. Mason, C. Chiu, R. Hogan, D. Moisseev, and S. Kneifel, “Retrievals of riming and snow density from vertically pointing doppler radars,” *Journal of Geophysical Research: Atmospheres*, vol. 123, no. 24, pp. 13–807, 2018.

[32] S. Kneifel, A. von Lerber, J. Tiira, D. Moisseev, P. Kollias, and J. Leinonen, “Observed relations between snowfall microphysics and triple-frequency radar measurements,” *Journal of Geophysical Research: Atmospheres*, vol. 120, no. 12, pp. 6034–6055, 2015.

[33] S. L. Mason, R. J. Hogan, C. D. Westbrook, S. Kneifel, D. Moisseev, and L. von Terzi, “The importance of particle size distribution and internal structure for triple-frequency radar retrievals of the morphology of snow,” *Atmospheric Measurement Techniques*, vol. 12, no. 9, pp. 4993–5018, 2019.

[34] S. Y. Matrosov, A. Heymsfield, and Z. Wang, “Dual-frequency radar ratio of nonspherical atmospheric hydrometeors,” *Geophysical research letters*, vol. 32, no. 13, 2005.

[35] J. Tyynelä and A. von Lerber, “Validation of microphysical snow models using in situ, multifrequency, and dual-polarization radar measurements in finland,” *Journal of Geophysical Research: Atmospheres*, vol. 124, no. 23, pp. 13273–13290, 2019.

[36] T. C. Choy, *Effective medium theory: principles and applications*, vol. 165. Oxford University Press, 2015.

[37] M. I. Mishchenko, L. D. Travis, and D. W. Mackowski, “T-matrix computations of light scattering by nonspherical particles: A review,” *Journal of Quantitative Spectroscopy and Radiative Transfer*, vol. 55, no. 5, pp. 535–575, 1996.

[38] M. A. Yurkin and A. G. Hoekstra, “The discrete-dipole-approximation code adda: capabilities and known limitations,” *Journal of Quantitative Spectroscopy and Radiative Transfer*, vol. 112, no. 13, pp. 2234–2247, 2011.

[39] C. Westbrook, R. Ball, and P. Field, “Radar scattering by aggregate snowflakes,” *Quarterly Journal of the Royal Meteorological Society: A journal of the atmospheric sciences, applied meteorology and physical oceanography*, vol. 132, no. 616, pp. 897–914, 2006.

[40] J. Leinonen, S. Kneifel, and R. J. Hogan, “Evaluation of the rayleigh–gans approximation for microwave scattering by rimed snowflakes,” *Quarterly Journal of the Royal Meteorological Society*, vol. 144, pp. 77–88, 2018.

[41] J. Leinonen, “High-level interface to t-matrix scattering calculations: architecture, capabilities and limitations,” *Optics express*, vol. 22, no. 2, pp. 1655–1660, 2014.

[42] J. Leinonen and W. Szyrmer, “Radar signatures of snowflake riming: A modeling study,” *Earth and Space Science*, vol. 2, no. 8, pp. 346–358, 2015.

[43] J. Leinonen and D. Moisseev, “What do triple-frequency radar signatures reveal about aggregate snowflakes?,” *Journal of Geophysical Research: Atmospheres*, vol. 120, no. 1, pp. 229–239, 2015.

[44] R. J. Hogan and C. D. Westbrook, “Equation for the microwave backscatter cross section of aggregate snowflakes using the self-similar rayleigh–gans approximation,” *Journal of the Atmospheric Sciences*, vol. 71, no. 9, pp. 3292–3301, 2014.

[45] J. Leinonen, D. Moisseev, and T. Nousiainen, “Linking snowflake microstructure to multi-frequency radar observations,” *Journal of Geophysical Research: Atmospheres*, vol. 118, no. 8, pp. 3259–3270, 2013.

[46] P. R. Brown and P. N. Francis, “Improved measurements of the ice water content in cirrus using a total-water probe,” *Journal of Atmospheric and Oceanic Technology*, vol. 12, no. 2, pp. 410–414, 1995.

[47] A. von Lerber, D. Moisseev, L. F. Bliven, W. Petersen, A.-M. Harri, and V. Chandrasekar, "Microphysical properties of snow and their link to ze–s relations during baecc 2014," *Journal of Applied Meteorology and Climatology*, vol. 56, no. 6, pp. 1561–1582, 2017.

[48] J. D. Locatelli and P. V. Hobbs, "Fall speeds and masses of solid precipitation particles," *Journal of Geophysical Research*, vol. 79, no. 15, pp. 2185–2197, 1974.

[49] C. D. Westbrook, R. Ball, P. Field, and A. J. Heymsfield, "Universality in snowflake aggregation," *Geophysical research letters*, vol. 31, no. 15, 2004.

[50] K.-i. Maruyama and Y. Fujiyoshi, "Monte carlo simulation of the formation of snowflakes," *Journal of the atmospheric sciences*, vol. 62, no. 5, pp. 1529–1544, 2005.

[51] T. H. Stein, C. D. Westbrook, and J. Nicol, "Fractal geometry of aggregate snowflakes revealed by triple-wavelength radar measurements," *Geophysical Research Letters*, vol. 42, no. 1, pp. 176–183, 2015.

[52] R. J. Hogan, L. Tian, P. R. Brown, C. D. Westbrook, A. J. Heymsfield, and J. D. Eastment, "Radar scattering from ice aggregates using the horizontally aligned oblate spheroid approximation," *Journal of Applied Meteorology and Climatology*, vol. 51, no. 3, pp. 655–671, 2012.

[53] D. Moisseev, A. von Lerber, and J. Tiira, "Quantifying the effect of riming on snowfall using ground-based observations," *Journal of Geophysical Research: Atmospheres*, vol. 122, no. 7, pp. 4019–4037, 2017.

[54] S. Y. Matrosov, "A dual-wavelength radar method to measure snowfall rate," *Journal of Applied Meteorology*, vol. 37, no. 11, pp. 1510–1521, 1998.

[55] R. J. Hogan, A. J. Illingworth, and H. Sauvageot, "Measuring crystal size in cirrus using 35-and 94-ghz radars," *Journal of Atmospheric and Oceanic Technology*, vol. 17, no. 1, pp. 27–37, 2000.

[56] N. Küchler, S. Kneifel, U. Löhnert, P. Kollias, H. Czekala, and T. Rose, "A w-band radar–radiometer system for accurate and continuous monitoring of clouds and precipitation," *Journal of Atmospheric and Oceanic Technology*, vol. 34, no. 11, pp. 2375–2392, 2017.

[57] P. Wang, "Dealiasing of doppler spectra for cloud radar at 94 ghz," *student thesis*, 2023.

[58] E. O'Connor, "Custom collection of model data from cabauw between 1 and 31 jan 2021," 2023.

[59] "Recommendation itu-r p.676-10: Attenuation by atmospheric gases," *Radiocommunication Sector of International Telecommunication Union*, 2013.

[60] C. D. Westbrook, R. Ball, and P. Field, "Corrigendum: Radar scattering by aggregate snowflakes," *Quarterly Journal of the Royal Meteorological Society: A journal of the atmospheric sciences, applied meteorology and physical oceanography*, vol. 134, no. 631, pp. 547–548, 2008.

[61] J. Niu, L. D. Carey, P. Yang, and T. H. V. Haar, "Optical properties of a vertically inhomogeneous mid-latitude mid-level mixed-phase altocumulus in the infrared region," *Atmospheric Research*, vol. 88, no. 3-4, pp. 234–242, 2008.

[62] P. R. Field, "Aircraft observations of ice crystal evolution in an altostratus cloud," *Journal of the Atmospheric Sciences*, vol. 56, no. 12, pp. 1925–1941, 1999.

[63] C. Westbrook, R. Ball, P. Field, and A. J. Heymsfield, "Theory of growth by differential sedimentation, with application to snowflake formation," *Physical Review E*, vol. 70, no. 2, p. 021403, 2004.

[64] P. R. Field and A. J. Heymsfield, "Aggregation and scaling of ice crystal size distributions," *Journal of the atmospheric sciences*, vol. 60, no. 3, pp. 544–560, 2003.

[65] H. Y. L. Mak, "Peering into the heart of thunderstorm clouds: Insights from cloud radar and spectral polarimetry," *Master thesis*, 2023.

[66] A. Protat, J. Delanoë, D. Bouniol, A. Heymsfield, A. Bansemer, and P. Brown, “Evaluation of ice water content retrievals from cloud radar reflectivity and temperature using a large airborne in situ microphysical database,” *Journal of applied meteorology and climatology*, vol. 46, no. 5, pp. 557–572, 2007.

[67] D. Turner, S. Kneifel, and M. Cadeddu, “An improved liquid water absorption model at microwave frequencies for supercooled liquid water clouds,” *Journal of Atmospheric and Oceanic Technology*, vol. 33, no. 1, pp. 33–44, 2016.

[68] U. Lohmann, F. Lüönd, and F. Mahrt, *An introduction to clouds: From the microscale to climate*. Cambridge University Press, 2016.

[69] A. J. Heymsfield, A. Bansemer, C. Schmitt, C. Twohy, and M. R. Poellot, “Effective ice particle densities derived from aircraft data,” *Journal of the atmospheric sciences*, vol. 61, no. 9, pp. 982–1003, 2004.

[70] M. D. Shupe, “A ground-based multisensor cloud phase classifier,” *Geophysical Research Letters*, vol. 34, no. 22, 2007.

Appendix

A. Comparison of DWR profiles from LV1 and LV0 products

The calculation of DWR using LV0 data was described in details in Section 5.2.1. The removal of extra parts of 35GHz spectra reduces the value of DWR. The reason for doing this is that only the common part of both spectra should be used to calculate DWR. The effect of such calculation manner can be seen when LV0 DWR (Figure 1 left) is compared with LV1 DWR (Figure 1 right) which is computed simply using two reflectivity profiles from LV1 product (Figure 1 right). Reflectivity profiles from LV1 are summation of the whole spectra for both 35GHz and 94GHz.

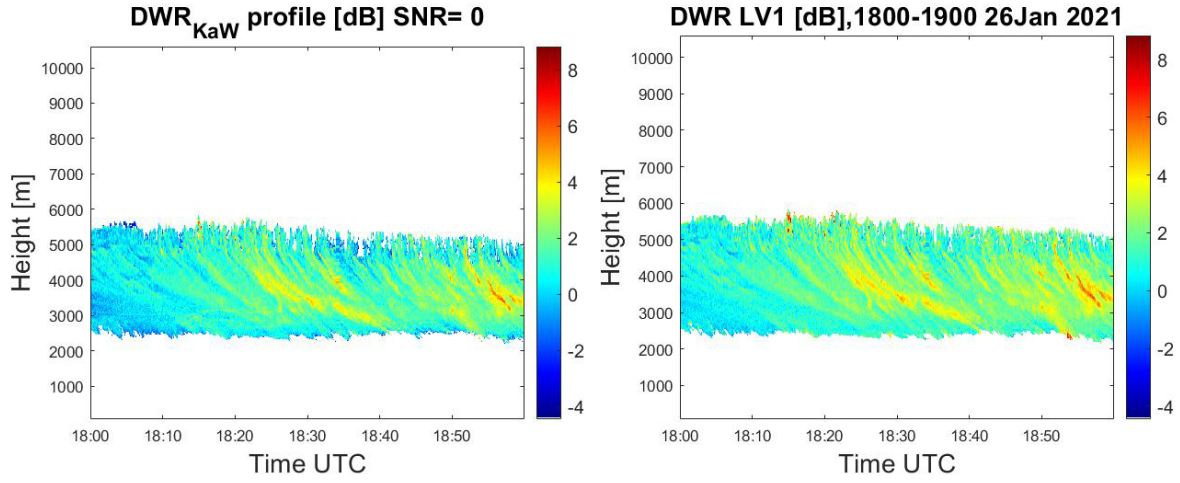

Figure 1: Left: LV0 DWR. Right: LV1 DWR. Both profiles are corrected for gas attenuation.

In Figure 1, most part of LV1 DWR profile (right) has a larger value than LV0 DWR (left). Besides, some outliers in LV1 DWR (right) near cloud top and bottom disappear in LV0 DWR (left). Therefore, the LV0 DWR is considered to be better than LV1 DWR.

B. Retrieving LWC profiles for mixed-phase cloud using sDWR

In this section, an abandoned direction of research is presented with some advice for future studies. In this section, the reasons why it is not feasible to retrieve LWC profiles from sDWR with the data I have are presented, which includes hardware limits such as radar sensitivity and physical limits like small DPSA of Ka and W band. The irregular shape of ice particles also increases the difficulty. Although it is attractive to make such retrieval, a success might not be close due to a series of challenges.

In [19], a method for retrieving liquid water content (LWC) from rain using sDWR was proposed. The sDWR of rain can be divided into 4 parts, among which are two important parts: The one representing small droplets is the Rayleigh plateau and the other one for larger droplets is a peak due to Mie effect (Figure 2). Both features stably exist in sDWR of rain. In Figure 2, the numbers at the top of the figure represent different parts of sDWR of rain. Part 1 is a noise region where reflectivities are lower than their noise level. Part 2 is the Rayleigh plateau. Part 3 is an upsloping Mie region and part 4 a peak and valley Mie region [19].

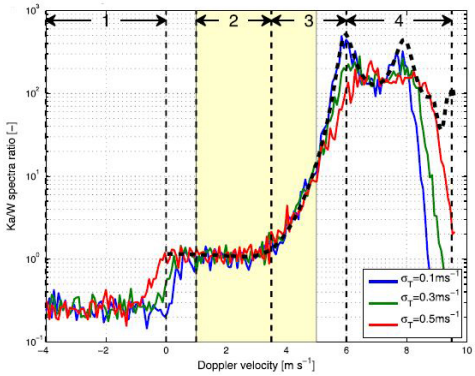

Figure 2: Figure 1 (a) from Tridon et. al. 2013 [19]. Simulations of the Ka/W sDWR for different turbulence intensities

The Rayleigh plateau is a part of sDWR with relatively constant value at a certain radar range. Its level mainly represents the value of DPIA caused by rain and grows as range increases. The equation of DPIA is given in Equation 2.5.

Once the level of Rayleigh plateau for most ranges is retrieved, the LWC profile can be obtained, since [19]:

$$DPIA_{rain} = 2\int_0^r (\alpha_{Ka}(s) - \alpha_W(s))ds = 2\int_0^r (k_{Ka}(s) - k_W(s))LWC(s)\ ds \tag{1}$$

where k_{Ka} and k_W are the attenuation coefficients per unit mass ($dB\ m^2 kg^{-1}$) of Ka band and W band dependent on temperature. The gas attenuation should be corrected before applying this method (Section 5.2.2). With temperature profile and the DPIA of raindrop at different ranges, the LWC profile $LWC(r)$ can be derived.

The same retrieval process was attempted to be applied to MPC, with the intention of recovering the spatial distribution and amount of supercooled liquid water. However, the difficulty in extracting the Rayleigh plateau from sDWR of MPC prevents further progress. The difficulty is that no clear, convincing and stably-existed Rayleigh plateau in sDWR can be found for MPC in the radar data. More details are discussed and explained using the best found case (2200-2300 26Jan 2021).

B.1. Case 22:00-23:00 26Jan 2021

The case 22:00-23:00 26Jan 2021 is considered to be a good case for LWC retrieval attempt in MPC because it has a very thick cloud (Figure 3) with considerable amount of LWP, with the maximum LWP of about $400g/m^2$ (Figure 4 left). The whole cloud is right below the freezing point of water (blue curves in Figure 3) and many processes was happening in the cloud. In Figure 3 (c), one of the most important features is the region with large DWR value started from 22:25 at about 3000m and extended to 2000m at 23:00. The DWR reaches more than 13dB in some part of this region, though some of the value might due to large ZDR in the same region [22]. At about 22:37, a vague vertical stripe of relatively high DWR can be seen from 5000m to the top of the cloud. The cause of the stripe is the large DPIA caused by hydrometers below 5000m along the radar beam. The time of this stripe also corresponds to the time of the peak of LWP (Figure 4), which indicates that considerable amount of supercooled liquid might exist below 5000m at that moment. In Figure 3 (d), there's a region with significant ZDR at around 3000m from 22:13 to 22:30, while in figure (a)(b) and (c) the same region exhibits low reflectivity and DWR compared to neighboring region. This indicates that some tiny ice particles with very non-spherical shape exist in that region with relatively low concentration.

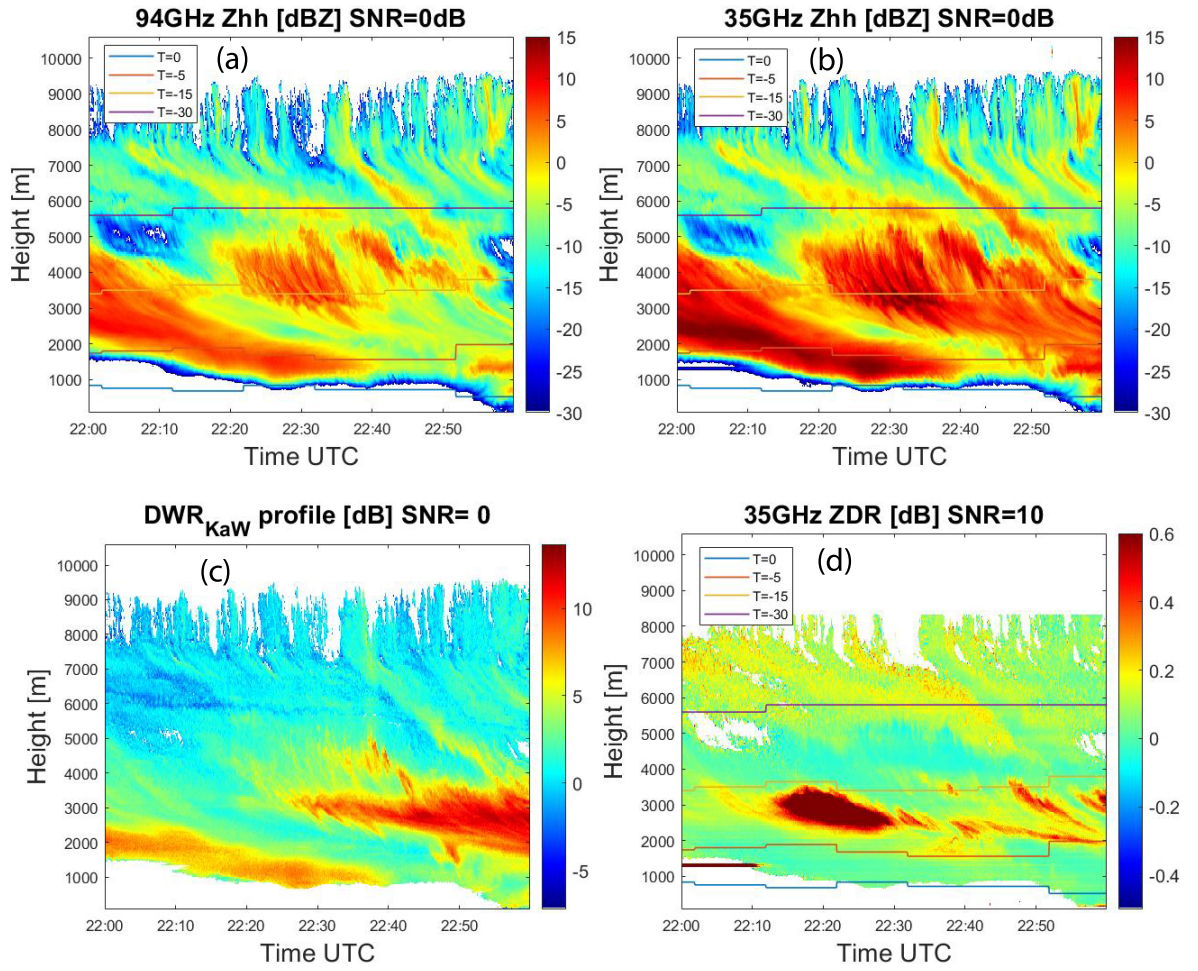

Figure 3: Radar measurement profiles with gas attenuation correction and ZDR calibration of Case 22:00-23:00 26Jan 2021: (a) Reflectivity at 94GHz (b) Reflectivity at 35GHz (c) Dual-wavelength ratio (d) Differential reflectivity at 35GHz. The curves in (a) (b) and (d) represents the temperature.

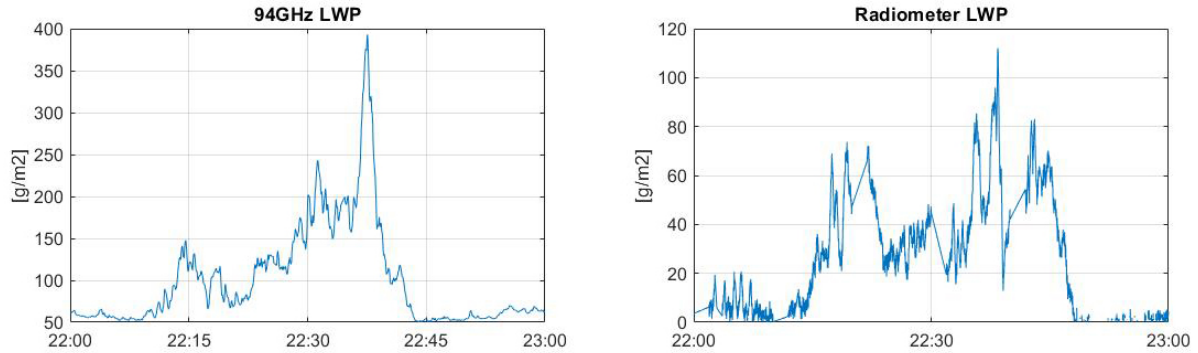

Figure 4: LWP measurement at 22:00-23:00 on 26 January, 2021. Left: LWP measured by the receiver on radar at 94GHz. Right: LWP measured by vertically pointing radiometer.

B.1.1 Low sensitivity of radar at 94GHz

The first reason for the difficulty of extracting Rayleigh plateau is the low sensitivity of radar at 94GHz compared to the radar at 35GHz. The narrower spectra at 94GHz due to low sensitivity lead to the loss of a part of sDWR for small particles where the Rayleigh plateau is expected to be. In Figure 5, two examples of spectral reflectivity are shown at different height for the same time. It's very common that

sZ_{hh} of 94GHz (blue dash line) has narrower Doppler velocity range than sZ_{hh} of 35GHz (red solid line).

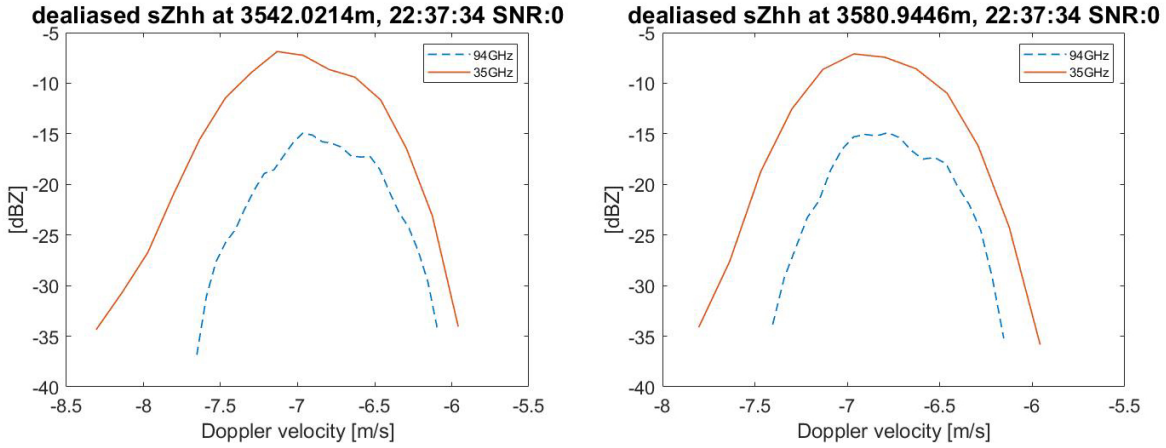

Figure 5: Dealiased sZ_{hh} of 94GHz and 35GHz at 3542m (Left) and 3580m (Right) at 22:37:34 on 26Jan.

Thus the Rayleigh plateau might not even exist in the sDWR. The remaining parts of Rayleigh plateau that survive this will be relatively noisy and very narrow, which increase the challenge of extraction. Figure 6 left shows the two sDWR corresponding to the Figure 5. These are the only few spectra that can bring relatively clear Rayleigh plateaus which are considered to be from $-7m/s$ to $-6.2m/s$ in Figure 6 left. It's quite common to have a significant large sDWR on the right end and destroy the feature of Rayleigh plateau. However, the reason for this is still unclear.

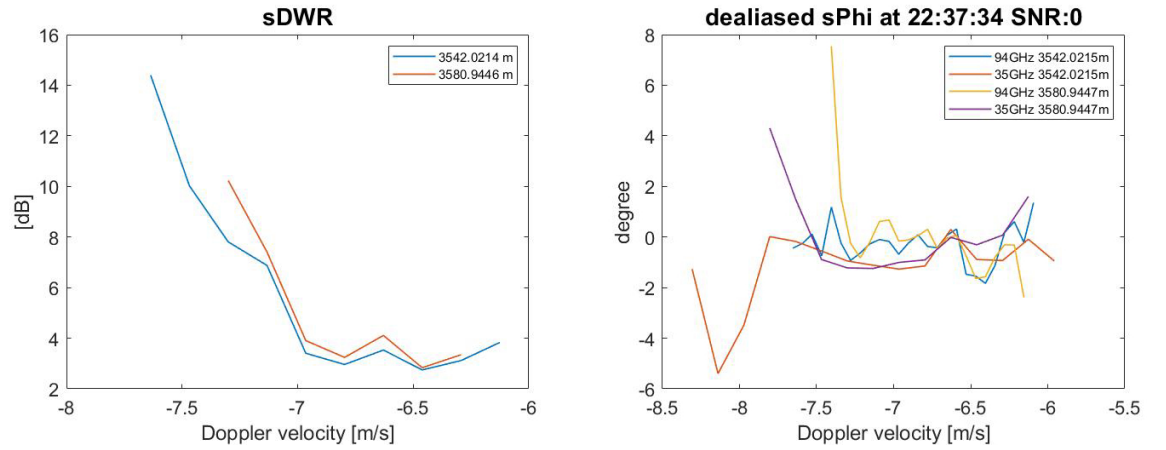

Figure 6: Left: sDWR corresponding to the two height in Figure 5. Right: sPhi corresponding to the two height and frequencies in Figure 5.

On the contrary, the spectral width of rain is much wider than in non-convective MPC (about $1m/s$) as shown in Figure 2, which allows a much wider (more than $2m/s$) and recognizable Rayleigh plateau at 94 and 35GHz. What's worse, the spectral differential phase (sPhi) at 94GHz is very noisy, which renders the effort of distinguishing the start of Mie peak (confirmation of the Rayleigh plateau) from sPhi failed. In Figure 6 right, the spectral differential phase of the same cases are shown. The large deviation on the left ends indicates the start of Mie regime while a relatively smooth parts on the right are Rayleigh plateaus. Only the sPhi of 94GHz (blue and yellow curves in Figure 6 right) is needed for determining where the start of Mie regime is, but they're noisier in flat parts than sPhi of 35GHz (red and purple curves). Besides, in most situations sPhi is extremely noisy with strong deviation on the right ends and no patterns can be identified as in Figure 6 right.

To give an overview of the problems in sDWR, the spectrograms of the most promising time (22:37:34) for extracting Rayleigh plateau are shown in Figure 7. The width of spectra is large compared to other time steps and the highest LWP presents at this time. The spectra of sDWR are aligned to their minimum absolute Doppler velocity on the right end to better exhibit their width. The only altitude range for extracting Rayleigh plateau convincingly is from about 3500m to 4300m Figure 7 right) where relatively stable sDWR plateaus exist at the right end. For other altitudes, the sDWR is bothered by all kinds of mysterious effects and no Rayleigh plateaus can be found. For example, the prevailing large values at the minimum Doppler velocity bins (e.g. from about 1300m to 2500m) and a small peak of sDWR at about 5000m at around 15th velocity bins need convincing explanation. Such phenomena diminish the hope of finding Rayleigh plateaus, not to mention that for other cases, the sDWR are usually much narrower than Figure 7 and haunted by the same issues.

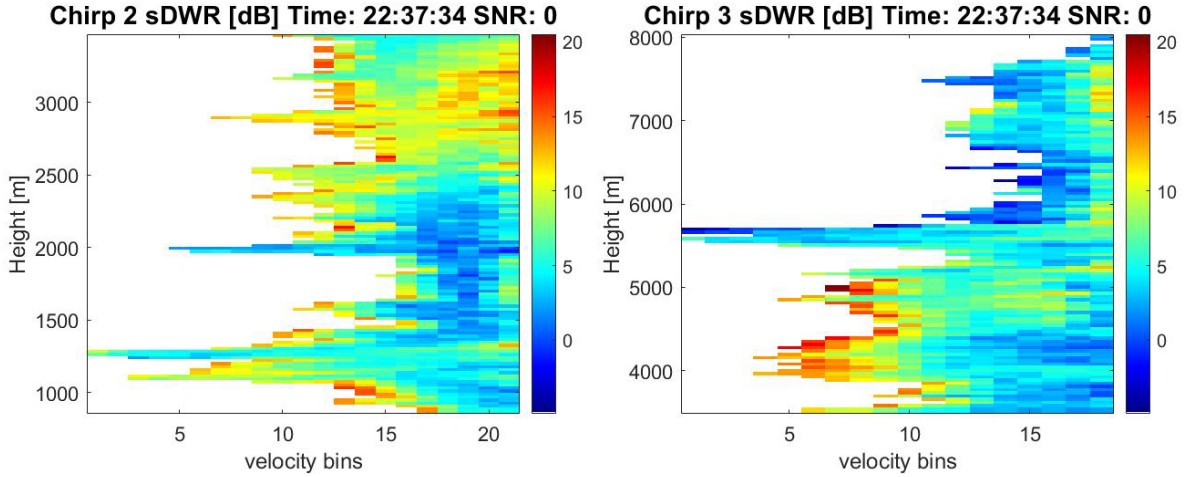

Figure 7: The spectrograms of sDWR of Chirp 2 (left) and Chirp 3 (right) at 22:37:34 on 26Jan 2021 without correction of gas attenuation

To applied the method in [19], ideally, reliable extraction of Rayleigh plateau is needed at several altitudes which spread across the entire radar beam range, so that the DPIA of supercooled liquid between these altitudes can be detected by the levels of Rayleigh plateau.

B.1.2 The effect of non-vertical elevation angle of radar

Another disadvantage is that the sDWR of non-spherical particles is affected by the elevation angle of radar, as mentioned in Section 2.5.2 and Section 2.1.2. Some velocity bins with small particles which should have been identified as part of Rayleigh plateau can exhibit large sDWR value due to non-sphericity of those particles. Since a quantitative relation about such effect needs further study, it is very challenging to distinguish this phenomenon.

B.1.3 Small DPIA from supercooled liquid

Besides, an intrinsic difficulty lies in the relation between the two-way specific attenuation ($2(k_{Ka}(r) - k_W(r))$ in Equation 1) (DPSA) of pure liquid water and temperature. Figure 8 shows the relation between DPSA of liquid water and temperature at 35GHz and 94GHz, which is calculated according to [67]. As temperature increases, the DPSA of liquid water also increases.

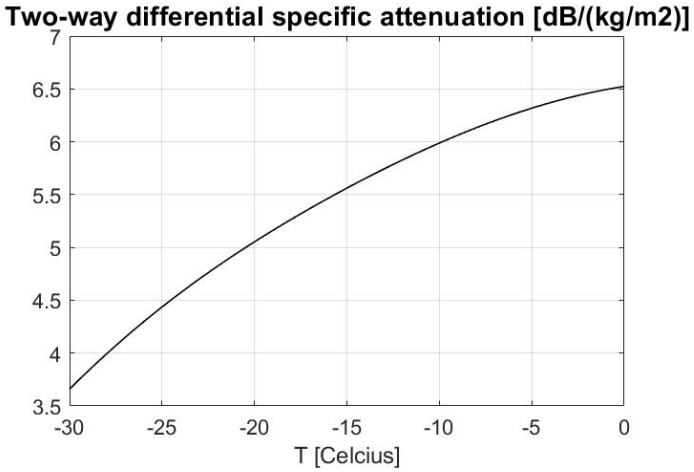

Figure 8: Two-way specific attenuation at 35GHz and 94GHz of supercooled liquid water versus temperature

The issues is that the magnitude of such DPSA is too small for my retrieval purpose. At $-15°$, $1kg/m^2$ of supercooled liquid water can produce about 5.5dB of DPIA that can be shown in the level of Rayleigh plateau. However, the highest LWP in all MPC cases is about $400g/m^2$ and it lasts for no more than two minutes. This LWP can create about 2.6dB of DPIA in DWR even at $0°C$ (the warmest temperature), which is not much compared to the noise in sDWR. In reality the supercooled liquid is usually distributed within several hundreds of meters height below freezing point and the DPIA must be less than 2.6dB. Other found MPC cases usually have LWP from 100 to 200 g/m^2, which can be converted into 0.65dB to 1.3dB of DPIA at $0°C$. This amount of increase in the level of Rayleigh plateau can easily be hidden by noise.

B.2. Conclusion

The extraction of Rayleigh plateau in sDWR for ice cloud or MPC is intrinsically more challenging than in rain due to narrower width of spectra and small DPSA caused by supercooled liquid water. Additional challenges are from our radar elevational angle and low sensitivity of radar at 94GHz. A additional limitation of such method is that if the supercooled liquid layer is at the cloud top which usually has low SNR, any similar attempts to extract Rayleigh plateaus might fail since there's no enough sDWR spectra above the liquid layer. In the Arctic such situation is very common [5].

For future studies with the same goal, it is suggested that a vertically-pointing radar should be used, unless the effect of non-spherical particles and the elevation angle of radar in DWR is further studied. The figure 1 in [24] can provide some information about the suitable radar frequencies for such purpose, which is also calculated using [67]. The lower frequency in two radar wavelengths should be lower than 35GHz (e.g. Ku band or lower frequency) in order to increase the DPSA caused by supercooled liquid, but the higher frequency should not be higher than 94GHz because Mie regime will occupy more part in the sDWR for ice particles in clouds and make Rayleigh plateau narrower. Improving the radar sensitivity at the higher frequency is essential. Also, the differential attenuation of ice particles needs to be estimated carefully to minimize the error of LWC. Convective clouds with supercooled liquid might be better cases for such purpose, since the width of spectra in such cases is much larger than in stratiform clouds.

C. Event C

The third MPC event occurs from 20:00 to 21:00 on 26 January, 2021. The third event of MPC with low LWP is shown below with some retrieval results. This case is complicated and challenging to analyse and explain. There are two layers of cloud and they are connected to each other (Figure 9). The upper cloud contains mainly small particles while many bins in the lower cloud has sDWR larger than 8.5dB (Figure 9). However some regions in the lower cloud exhibit large ZDR. The retrieved profiles lose many bins due to extreme values in DWR and ZDR (Figure 11). The SRIWC of the upper cloud is very

noisy possibly because it is dominated by tiny ice particles at high altitude and therefore the SNR is low (Figure 12 left). The underestimation of IWP in later hour is mainly due to the lack of velocity bins with results.

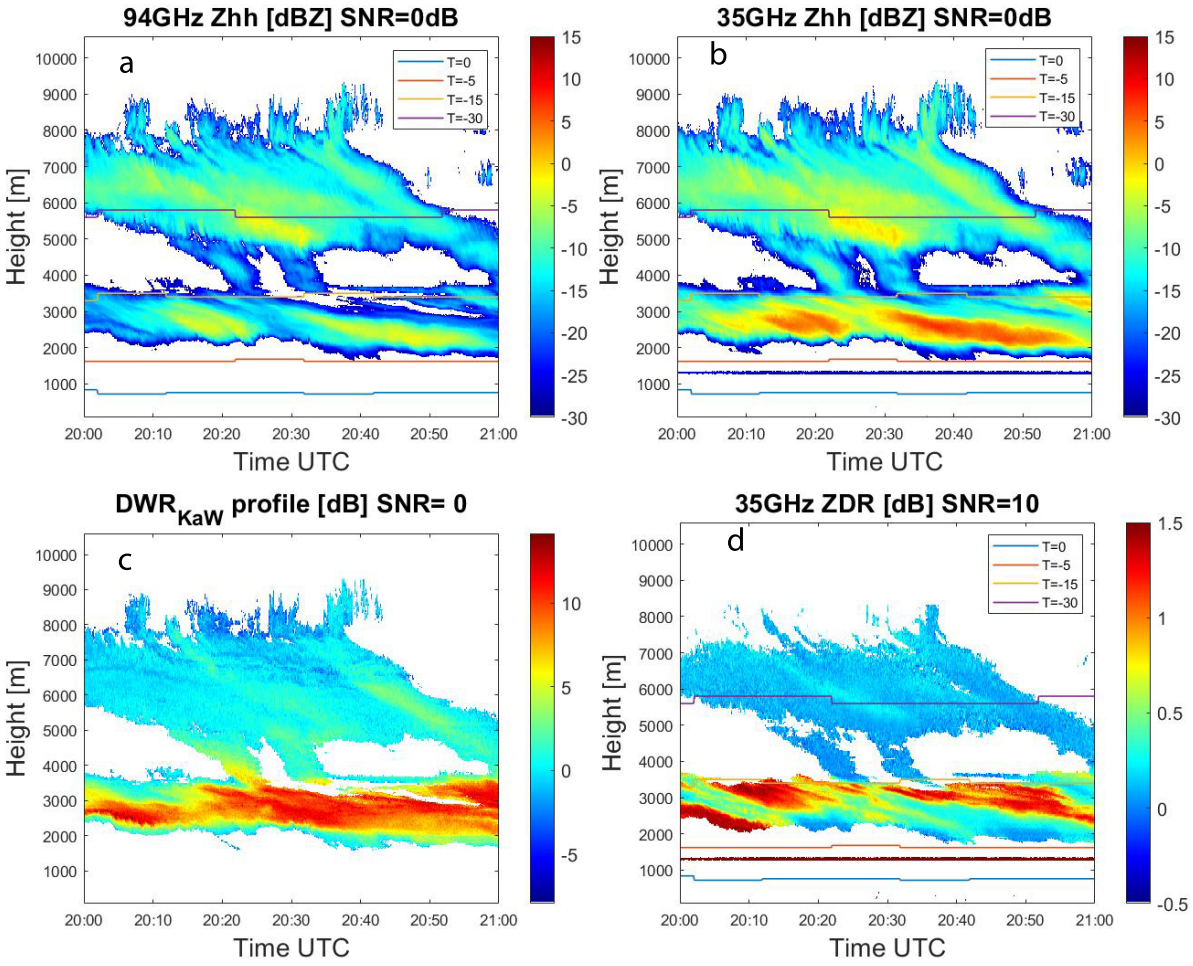

Figure 9: Radar measurement profiles with correction and calibration of Case 2000-2100 26Jan 2021: The order and names of figures are same as Figure 3

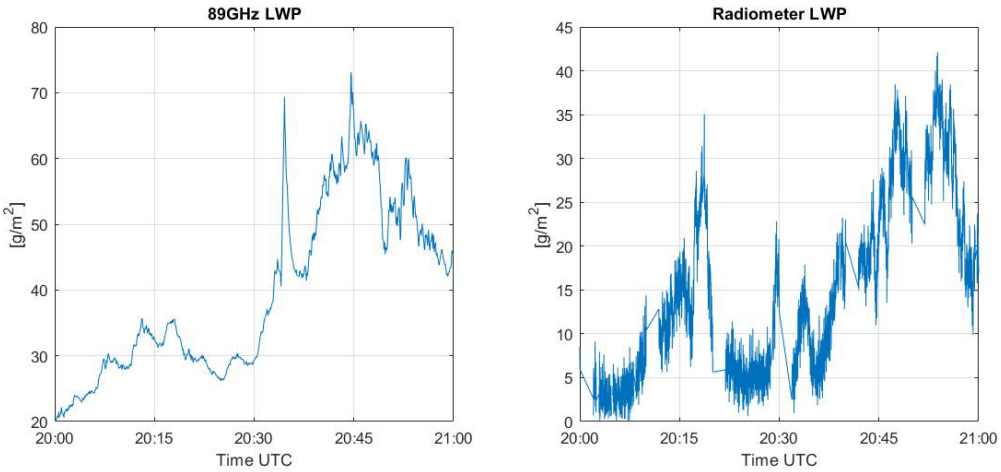

Figure 10: LWP measurement at 2000-2100 on 26 January, 2021. Left: LWP measured by the receiver on 94GHz radar. Right: LWP measured by vertically pointing radiometer.

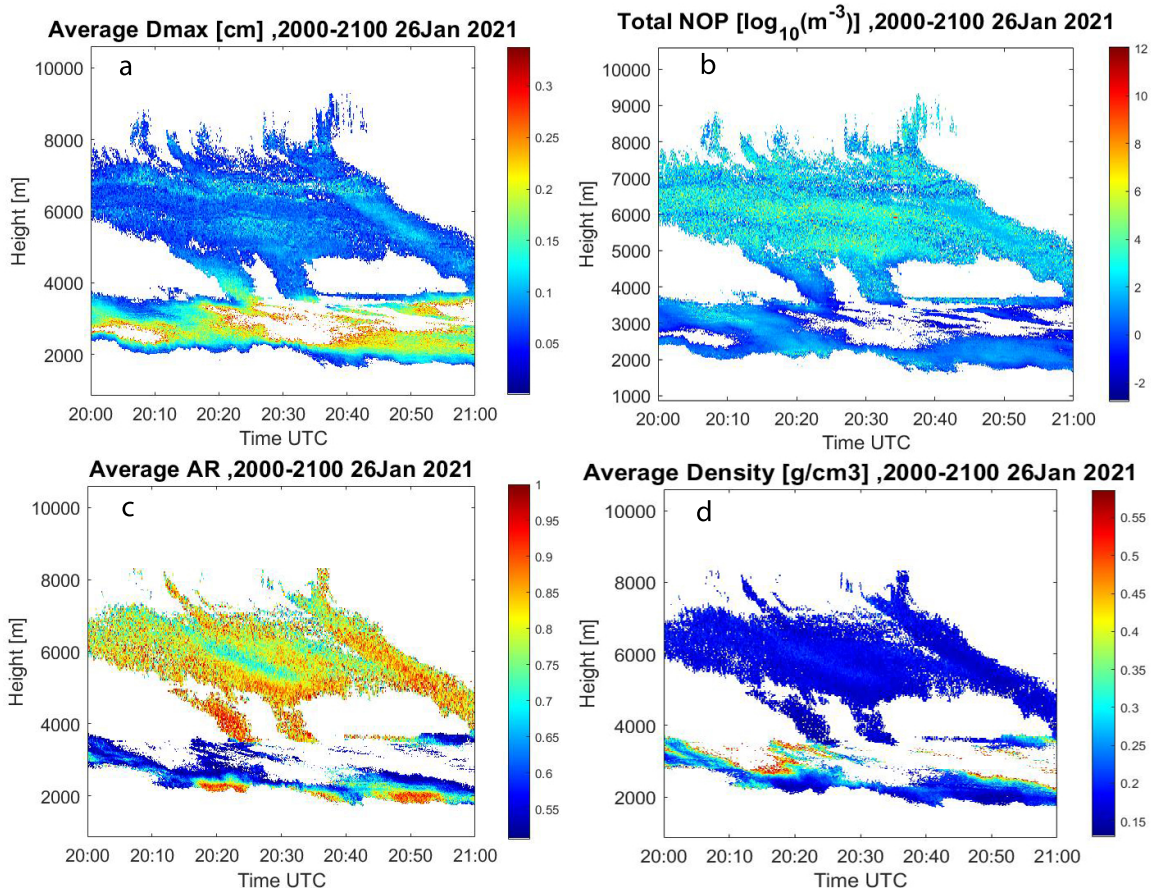

Figure 11: Resulting profiles of case 2000-2100 26Jan 2021. Same as Figure 6.9.

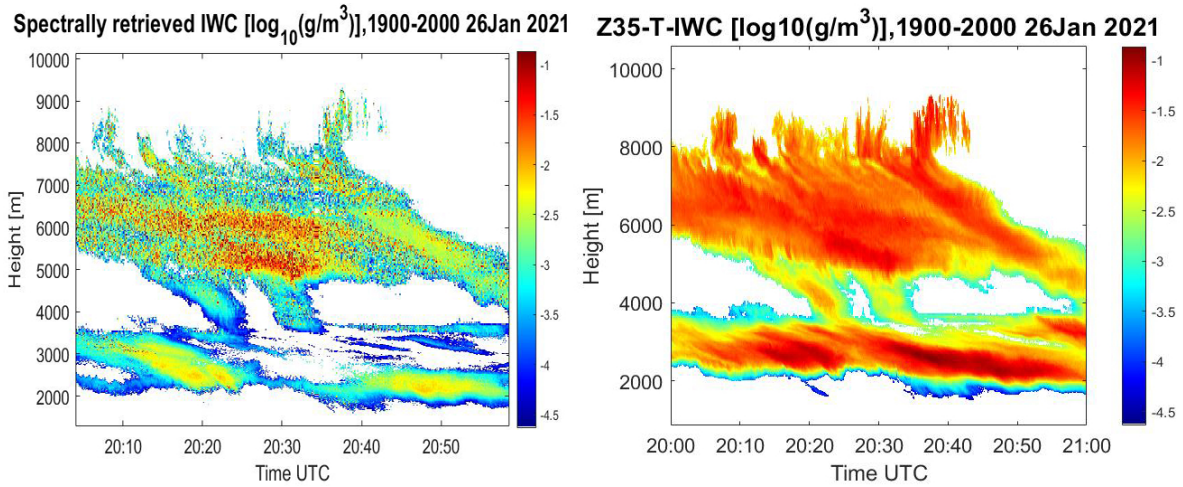

Figure 12: Spetrally retrieved IWC (left) and Z-T-IWC (right) of case 2000-2100 26Jan 2021.

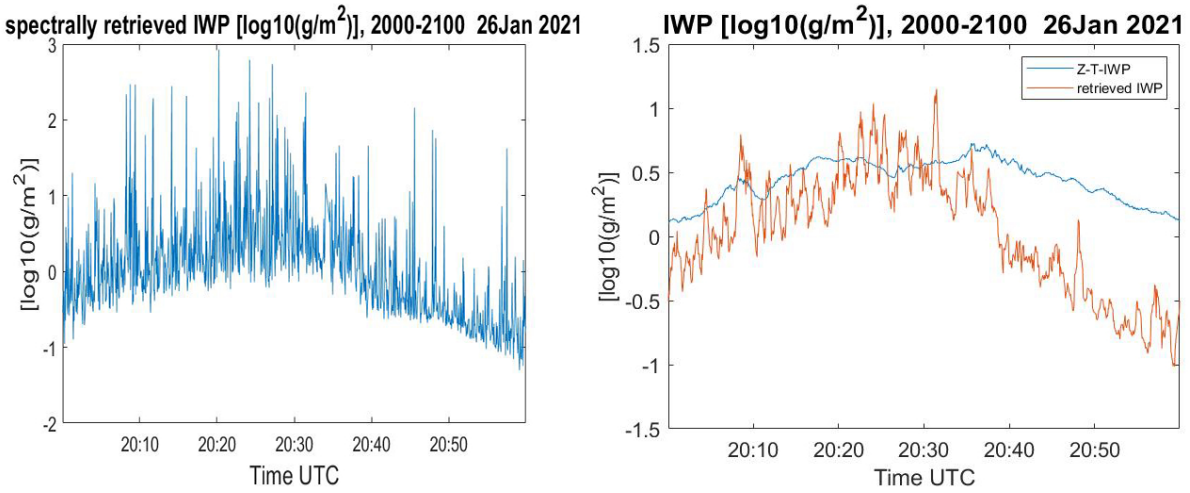

Figure 13: Case 2000-2100 26Jan 2021. Left: Spetrally retrieved IWP. Right: Comparison of Z-T-IWP and smoothed retrieved IWP (moving average of 36 seconds).

D. Statistics of retrieval process

The amount of valid velocity bins is tracked during the retrieval process at spectra level. The loss of valid velocity bins is mainly due to correction and calibration, but parameter setting can also play a role. Notice that although AR equal to zero (AR smaller than ZDR LUT limit) won't fail in the retrieval of number of particles, it doesn't count in valid velocity bins of AR result because actually there's no information about AR retrieved.

D.0.1 Chirp 2 1800-1900

The number of valid velocity bins of Chirp 2 in the case 1800-1900 26Jan 2021 is shown in Table 1 and corresponding setting in Table 2.

Steps	Number of valid velocity bins
sDWR (SNR=0dB) after gas correction	263671
Dmax and mass	259138
sZDR (SNR=10dB) after calibration	229465
AR and density	182714
NOP	259138

Table 1: Number of valid velocity bins using parameter setting in Table 2

DWR limit	8.5dB
ZDR LUT AR	0.2-1
ZDR LUT density	0.05-0.6g/cm^3

Table 2: Parameters setting of Table 1

In Table 1, the reduction of bins from sDWR to Dmax is due to the bins with sDWR larger than DWR limit are removed. The few valid sZDR is mainly resulted from higher noise removal level, which limits the valid bins with AR and density. In the retrieval process of AR and density, the loss is from the limit of the range of ZDR LUT Table 2. The number of valid NOP is the same as the valid D_{max} and mass, since the retrieval of NOP is not limited by the input of AR. It only use AR when it's available, as described in Section 5.5.

If the DWR limit is set as 8dB, (ceteris p.) the number of valid velocity bins decreases, as shown in Table 3. It only shows the number which are different from Table 1.

Steps	Number of valid velocity bins
Dmax and mass	257578
AR and density	181448
NOP	257578

Table 3: Number of valid velocity bins using parameter setting in Table 2, but DWR limit is set as 8dB.

If the ZDR LUT density range is set as 0.05-0.9 g/cm^3 while other parameters remain the same as Table 2, the number of valid AR and density will increase to 182742 and others remain unchanged.

D.0.2 Chirp 3 1800-1900

The number of valid velocity bins for Chirp 3 with the setting in Table 2 is shown

Steps	Number of valid velocity bins
sDWR (SNR=0dB) after gas correction	250709
Dmax and mass	243145
sZDR (SNR=10dB) after calibration	205230
AR and density	145611
NOP	243145

Table 4: Number of valid velocity bins using parameter setting in Table 2